

Imaging techniques for guidance of radionuclide therapy

Casper Beijst

Colophon

Imaging techniques for guidance of radionuclide therapy
PhD Thesis, Utrecht University - with a summary in Dutch

© C. Beijst, Utrecht, 2016
cbeijst@umcutrecht.nl

All rights reserved. No part of this publication may be reproduced or transmitted in any form or by any means without permission in writing from the author. The copyright of the articles that have been published or have been accepted for publication has been transferred to the respective journals.

ISBN:	978-90-393-6517-5
Cover design:	Joep Beijst
Layout:	Proefschrift-AIO
Printing:	PrintSupport4U

Imaging techniques for guidance of radionuclide therapy

**Beeldvormende technieken voor geleiding van
radionuclidetherapie**

(met een samenvatting in het Nederlands)

Proefschrift

ter verkrijging van de graad van doctor aan de Universiteit Utrecht op gezag van de rector magnificus, prof.dr. G.J. van der Zwaan, ingevolge het besluit van het college voor promoties in het openbaar te verdedigen op dinsdag 5 april 2016 des middags te 2.30 uur

door

Casper Beijst

geboren op 13 augustus 1986
te Tilburg

Promotor: Prof. dr. ir. M.A. Viergever

Copromotor: Dr. ir. H.W.A.M. de Jong

Publication of this thesis was financially supported by:

Sirtex Medical Europe GmbH

Nuclear Fields International BV

Tromp Medical BV

Scionix Holland BV

ChipSoft BV

CONTENTS

Chapter 1	
Introduction	7
Chapter 2	
Toward simultaneous real-time fluoroscopic and nuclear imaging in the intervention room	23
Chapter 3	
Multimodality calibration for simultaneous fluoroscopic and nuclear imaging	37
Chapter 4	
A parallel-cone collimator for high-energy SPECT	53
Chapter 5	
Quantitative comparison of ^{124}I PET/CT and ^{131}I SPECT/CT detectability	73
Chapter 6	
Impact of reconstruction parameters on quantitative ^{131}I SPECT	91
Chapter 7	
Summary and general discussion	111
Addenda	124
Samenvatting Nederlands	
List of publications	
Dankwoord	
CV	

1

Introduction

Background

The most common types of cancer treatment involve surgery, radiation therapy and/or chemotherapy. Moreover, internal radiation therapy with radionuclides (i.e. radionuclide therapy) is used, which may have benefits over other treatment options, such as improved targeting and non-invasiveness. Examples of radionuclides used for therapeutic purposes are iodine-131 for thyroid cancer and yttrium-90 for lymphoma. Strategies for targeted delivery of radionuclides include binding of radionuclides to a cell-targeting molecule¹, employing the ability of the radionuclide to target specific cells on its own², intra-arterial injection³ and intra-tumoral injection⁴. The imaging of the distribution of radionuclides plays an important role in assessment of treatment response, dosimetry and treatment planning.

In this thesis several imaging techniques for guidance of radionuclide therapy are investigated. The development of imaging instrumentation, image reconstruction methods and methods for image analysis is discussed. This chapter provides relevant information about radionuclide therapy and the imaging modalities used for guidance of radionuclide therapy.

Nuclear Medicine

The field of nuclear medicine involves the use of radioactive substances to diagnose and treat diseases. The initial treatment of polycythemia vera, a disorder resulting in the overproduction of red blood cells, with phosphorous-32 in 1937⁵ is considered by many to signify the beginning of the field of nuclear medicine. This pioneering work was performed by John Lawrence, who became interested in the use of isotopes for therapeutic purposes when he was working together with his brother Ernest Lawrence, inventor of the cyclotron, at the radiation laboratory in Berkeley (now known as the Lawrence Berkeley National Laboratory). Another early application of radiopharmaceuticals was the use of radioiodine for treatment of thyroid cancer, which was first described by Samuel Seidlin in 1946². Radioiodine is still one of the most commonly used isotopes for treatment in clinical practice.

Up until the 1950s, radiopharmaceuticals were mostly used for therapeutic purposes. However, the invention of the scintillation camera by Hal Anger for imaging of gamma rays in the beginning of the 1950s, meant that radiotracers could also be used for diagnostic purposes⁶. Over the years, many radiotracers have been developed that target specific biochemical processes. An example of a tracer used for diagnostic purposes is technetium-99m sestamibi for imaging of the myocardium. ^{99m}Tc sestamibi is a complex of ^{99m}Tc bound to six methoxyisobutylisonitrile (MIBI) ligands and is used for detection of ischemia in the heart muscle by assessing the difference between images of the heart acquired at rest and after exercise.

The principles of tomography, using multiple projections to reconstruct volumes, can be applied to nuclear imaging to obtain three-dimensional nuclear images. The availability of three-dimensional images as acquired by single photon emission computed tomography (SPECT) and positron emission tomography (PET) allows for more accurate diagnosis and treatment monitoring as a consequence of the more detailed information about the distribution of radionuclides.

Nuclear images can be difficult to interpret due to the absence of an anatomical reference. They are easier to interpret when presented in conjunction with co-registered anatomical information

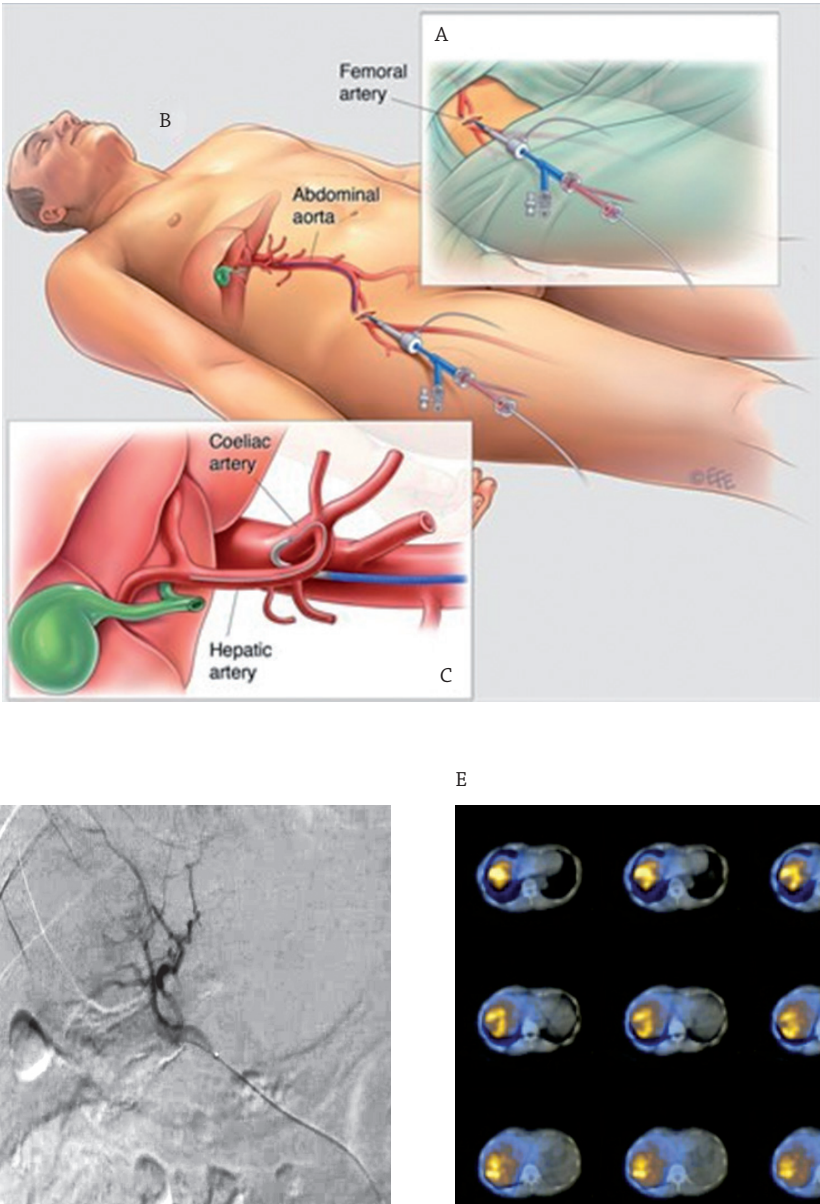


Figure 1.1 Schematic drawing of the radioembolization procedure (**A** and **B**) showing the small incision into the femoral artery, (**C**) the insertion of the catheter into the hepatic artery, (**D**) the hepatic angiogram and (**E**) the posttherapeutic SPECT/CT (courtesy Sirtex Medical Europe GmbH, Bonn, Germany).

from e.g. a computed tomography (CT) scanner. For this reason, hybrid SPECT/CT and PET/CT modalities developed in the late 1990s are now routinely used in clinical practice.

Radioembolization

A specific example of radionuclide therapy is liver radioembolization⁷⁻⁹. Liver radioembolization involves the injection of radioactive yttrium-90 microspheres for internal radiation therapy in the hepatic arteries supplying the tumors. As the name of the procedure suggests, this is achieved by embolization. That is, microspheres with a diameter of 20 – 40 μm selectively occlude the blood vessels, lodging them within the tumor, where they deliver therapeutic dose to the cancerous tissue. The microspheres are administered percutaneously under fluoroscopic guidance in the hepatic artery. The microspheres can be delivered selectively as the tumors in the liver are supplied by blood almost entirely by the hepatic artery, whereas the portal vein supplies most of the healthy liver with blood. This is shown in Figure 1.1.

The procedure comprises two phases. First, a hepatic angiogram (Figure 1.1D) is made to map the hepatic vasculature. Coiling of branches of the hepatic artery is performed to prevent the microspheres from entering the gastrointestinal tract and/or lungs. After coiling, a 'scout' dose of $^{99\text{m}}\text{Tc}$ labeled to albumin particles ($^{99\text{m}}\text{Tc}$ MAA) is administered, to assess whether the therapeutic microspheres can be administered safely. A SPECT/CT is performed to image the distribution of $^{99\text{m}}\text{Tc}$. Additional coiling may be required when depositions of $^{99\text{m}}\text{Tc}$ outside of the liver are found.

The therapeutic dose is administered during the second phase of the procedure, as shown in Figure 1.2. This dose generally consists of 3 – 5 GBq of ^{90}Y . A post-treatment SPECT/CT is performed for treatment monitoring and dosimetry (Figure 1.1E). Although ^{90}Y is mostly used for radioembolization, other isotopes such as ^{166}Ho have also been used successfully¹⁰.

Medical Imaging

This section discusses the imaging modalities that play a vital role in radionuclide therapy. The principles of nuclear imaging modalities such as scintigraphy (planar imaging), SPECT and PET are discussed. Moreover, the dynamic imaging technique for x-ray imaging in real-time, fluoroscopy, is discussed.

SPECT

Single photon emission computed tomography (SPECT) has been used as an imaging modality for many years, and is considered the workhorse of nuclear medicine. Although SPECT cannot compete with positron emission tomography (PET) in the sense of sensitivity, it remains the preferred modality for a large number of applications. SPECT systems rely on scintillation/gamma cameras for the acquisition of projections. An image of a SPECT system is shown in Figure 1.3.

Photon detection

Photon detection in scintillation/gamma cameras relies on indirect detection. First, gamma photons are absorbed in the NaI(Tl) scintillation crystal, creating a cascade of scintillation photons. The scintillation photons disperse in all directions, and part of the photons is absorbed

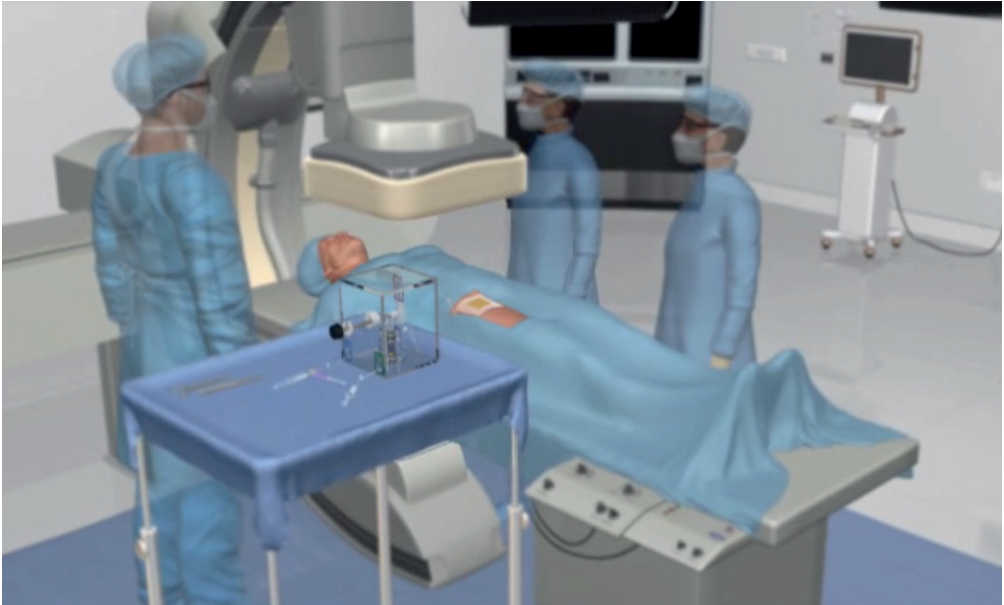


Figure 1.2 The angiographic procedure for administration of the ^{90}Y microspheres (courtesy Sirtex Medical Europe GmbH, Bonn, Germany).



Figure 1.3 Picture of a clinical SPECT/CT system (courtesy Philips Healthcare, Best, The Netherlands).

by a phosphorescent layer on the photomultiplier tube (PMT). Photoelectrons are created and the signal is amplified electronically by the PMT.

Collimation

Gamma cameras can detect high-energy photons, but they require a collimator to obtain useful images, similar to a photo camera requiring a lens to create an image. Since the direction of gamma rays cannot be bent the same way visible light rays are bent by lenses, absorption collimation is used to create projections. Collimators for nuclear imaging are designed to absorb all rays except those from a specific direction. Since this type of collimation is based on absorption, high stopping power of the collimator material is important to guarantee image quality, so that elements with a high atomic mass are preferred. Typically lead is used for collimators, because of its high atomic number and low cost. Tungsten and gold are used for collimators as well.

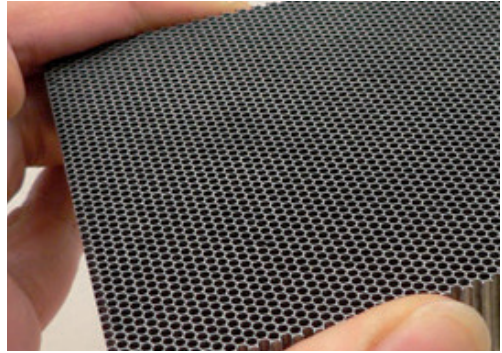


Figure 1.4 Picture of a parallel hole collimator (courtesy Nuclear Fields International BV, Vortum-Mullem, The Netherlands).

The most commonly used type of collimator in clinical practice is the parallel hole collimator. Parallel hole collimators consist of parallel ‘channels’ that are separated by thin walls or septa, so that incoming gamma rays are only allowed to pass through the collimator if they are travelling in a direction parallel to the septa. The septa are placed in a hexagonal pattern (see Figure 1.4). The septal thickness, length and hole size of parallel hole collimators can be optimized for a specific application. The strategy used to optimize parallel hole collimators for high-energy applications is to increase septal thickness and length to limit septal penetration. In general, increasing the septal thickness will decrease the amount of penetrated photons, but it will also decrease the system sensitivity. A decrease in sensitivity can be compensated for by increasing the hole size, but this will in turn compromise spatial resolution. In other words, optimizing the design of a parallel hole collimator involves a tradeoff between septal penetration, spatial resolution and sensitivity.

The septa of collimators are not necessarily placed in parallel, as collimators can also be designed with converging or diverging septa. The converging and diverging septa result in magnified and minified projection images, respectively. Generally, converging collimators create images with a higher resolution and have a higher sensitivity at the cost of a smaller field of view, whereas diverging collimators have a lower resolution and sensitivity but a larger field of view¹¹.

Pinhole collimators are based on an entirely different principle of collimation. Working on the same principles as the ‘camera obscura’, an inverted projection of the object is created on the detector with a magnification factor depending on the detector-pinhole distance and the object-pinhole distance. Pinhole collimators are an interesting alternative to parallel hole collimators for high-energy SPECT imaging, since pinholes can be designed in such a way that collimator penetration is limited¹². Depending on the application and geometry, however, pinhole systems have either limited sensitivity or a small field of view (FOV); the latter is used for example in small

organ imaging (e.g. ¹³) and small animal imaging (e.g. ¹⁴). To overcome the problem of limited sensitivity, multiple pinholes can be used¹⁵.

Image degrading effects

The quality of SPECT and scintigraphy images may be hampered by several factors. As explained above, the collimator is a crucial part of the gamma camera for creating images, which relies on the principle of absorption collimation. However, absorption of single photons is a probabilistic effect. Therefore, a small part of the gamma photons may still penetrate the collimator and hit the detector, even if the photon is not travelling in the allowed direction. The detection of these penetrated photons has an adverse effect on image quality. Photons may also be scattered in the collimator, which causes an increase of noise and loss of contrast.

Apart from the fact that the resolution is limited by the collimator, it is also limited by the intrinsic resolution of the gamma camera. This is a component of the resolution that is ascribed to accuracy with which the gamma camera is able to estimate the position of the scintillation event. Partial volume effects may occur as a consequence of the limited resolution of a gamma camera.

Another important image degrading effect is attenuation. Depending on the distance the gamma photons have to travel through the patient, only a part of the gamma photons leaves the human body without tissue interaction. A significant part of the gamma photons is therefore attenuated, depending of the energy of the gamma photons. Photons are attenuated mainly because (Compton) scatter in the patient and for a small part due to absorption.

These scattered photons may however still be detected on a more or less random location, which is another factor that degrades image quality. During Compton scatter, the energy and the direction of the photon is changed. Therefore, after a scatter event, it is no longer possible to determine the origin of the photon. Fortunately, most of the detected scattered photons can be rejected effectively by using an energy window. Nevertheless, some scattered photons will inevitably be detected in the energy window due to the limited energy resolution.

Reconstruction

Tomographic reconstruction methods can be used to convert multiple two-dimensional projection images, as acquired by gamma cameras, into a single three-dimensional image of the activity distribution. Iterative reconstruction methods are typically used in clinical practice for reconstruction of activity distributions. The maximum likelihood expectation maximization (MLEM) is an iterative reconstruction algorithm, which incrementally changes the reconstruction at each iteration¹⁶. The ordered subset expectation maximization (OSEM) algorithm¹⁷ is an adaptation of the MLEM algorithm designed to increase speed, and is often used in clinical practice.

The number of iterations used for reconstruction affects image quality, and more specifically, the contrast and noise content of the images. A large number of iterations can be used to increase contrast recovery, although this will increase image noise. Choosing the number of iterations inherently involves a tradeoff between contrast and noise.

An advantage of using iterative reconstruction methods, is that the physics of image degrading effects can be modeled in the reconstruction algorithm, to improve the accuracy of the reconstruction.

Correction for image degrading effects

Physical processes responsible for image degrading effects can be incorporated in the reconstruction algorithm. Attenuation correction is commonly incorporated in the projection operators of the iterative reconstruction method, by taking into account the attenuation coefficient and the path length through the tissue. Attenuation correction methods require attenuation maps that can be acquired by means of co-registered CT images.

Compton and Rayleigh scattering can change the direction (and energy) of gamma photons. Correction for scatter in clinical practice is often performed using the triple energy window (TEW) method¹⁸. As the name of the method suggests, three energy windows are acquired to perform this correction. An estimate of the amount of scattered photons is obtained for each projection angle by averaging the amount of photons in the upper and lower scatter window.

As the resolution of collimators and the intrinsic resolution of gamma cameras are limited, acquired projections of an activity distribution appear 'blurred'. The amount of blurring that occurs during an acquisition depends on the shape of the Point Spread Function (PSF), which is defined as the response of a gamma camera to a point source. The shape of the PSF can be characterized accurately and incorporated in the reconstruction algorithm, to improve the quality of reconstructed images.

PET

A picture of a clinical PET/CT system is shown in Figure 1.5. This section discusses the principles of PET imaging.

Co-incidence detection

Positron emission tomography is based on the detection of two annihilation photons that are produced when an emitted positron recombines with an electron. When a positron recombines with an electron, two 511 keV photons are emitted in opposite directions. The principle of PET relies on detection of these annihilation photons on opposite sides of the PET detector ring. The detection of two photons is regarded as a 'count' when they both are detected within the coincidence timing window. When a count is acquired, it is assumed that an annihilation event has occurred on the virtual line between the positions of detection (i.e. the line of response). The three-dimensional activity distribution can be reconstructed if sufficient counts have been acquired.

Detection

The detection of annihilation photons relies on the same principle as the detection of gamma photons with a scintillation camera. That is, photons are first absorbed by the scintillation crystal, where optical scintillation photons are created. Next, the optical signal is amplified electronically using an array of photomultiplier tubes.

Image degrading effects

When two photons are accepted by the coincidence timing window as well as the energy window, a count is stored. These counts are called 'true' counts when both annihilation photons originate from the same annihilation event. However, two annihilation photons from two different annihilation events may also be detected within the coincidence timing window. These 'random' counts have

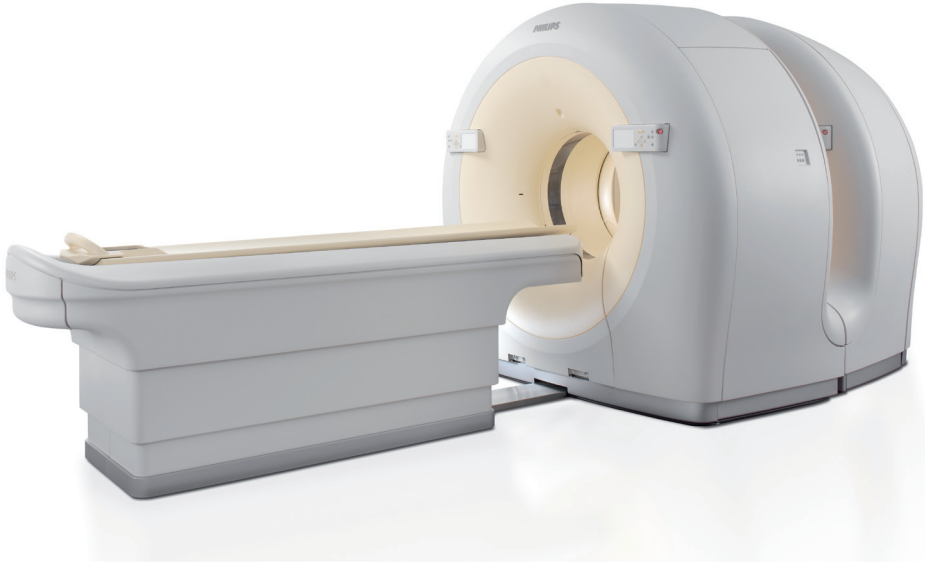


Figure 1.5 Picture of a clinical PET/CT system (courtesy Philips Healthcare, Best, The Netherlands).

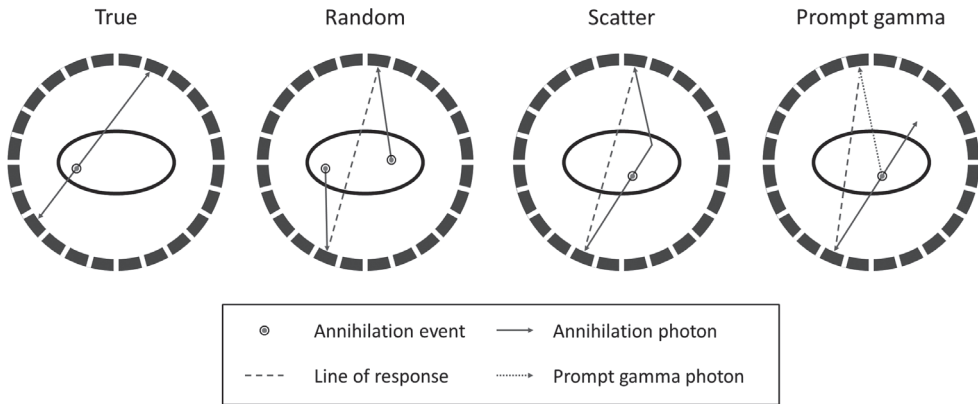


Figure 1.6 Schematic drawing of possible events.

an adverse effect on image quality. The same holds for two annihilation photons from the same annihilation event, when one of the photons is scattered. In such a case, the line of response of a scatter event does not contain information about the position of the actual annihilation event. This is illustrated schematically in Figure 1.6.

For some isotopes, positrons are emitted in cascade with the emission of other gamma photons, so that additional photons are emitted together with the two annihilation photons. Iodine-124 is an example of an isotope that emits prompt gammas in cascade with the positron. When these prompt gamma photons are detected, they may be mistaken for an annihilation photon, resulting in an erroneous line of response. This is illustrated schematically in Figure 1.6.

Reconstruction

The ordered subset expectation maximization (OSEM) algorithm is generally used for reconstruction of the scans performed in clinical practice. Attenuation is corrected for on the basis of the attenuation map as acquired from the co-registered CT data. In addition, scatter is corrected for in clinical practice using fitting techniques¹⁹ or model based scatter correction techniques²⁰. Correction for random counts is generally performed by applying delayed event subtraction²¹. Random and scatter correction can either be incorporated by subtracting the randoms from the sinogram before reconstruction, or by adding the randoms sinogram to the measured sinogram during each iteration in the forward projection^{22,23}.



Figure 1.7 Image of a fluoroscopic x-ray system (courtesy Philips Healthcare, Best, The Netherlands).

The time difference of detection between annihilation photons contains information about the location of the annihilation event along the line of response. This time-of-flight (TOF) information can be incorporated in the reconstruction during the backprojection step to improve image quality.

As the intrinsic resolution of PET detectors is limited, the measured projections appear 'blurred'. The amount of blurring that occurs during an acquisition depends on the shape of the Point Spread Function (PSF). The shape of the PSF can be incorporated in the reconstruction method to improve the quality of reconstructed images.

Fluoroscopy

Fluoroscopy is a dynamic x-ray imaging technique, displaying images in real-time. For this reason, fluoroscopy is commonly used in the intervention room and/or operating theatre for guidance of procedures. A picture of a clinical fluoroscopy system is shown in Figure 1.7.

X-ray tube

The x-ray photons required for fluoroscopic imaging are created in the x-ray tube by accelerating electrons toward the anode. These electrons are emitted by the cathode, which is heated to free electrons from the filament material. When the electrons, accelerated by the electric field, hit the anode, photons are created as a consequence of the Bremsstrahlung effect.

X-ray detection

Image intensifier

Image intensifiers can be used to convert x-ray photons into optical photons. X-ray photons enter the image intensifier through the input window and luminescence occurs when the x-ray photons hit the input phosphor screen, creating optical photons. Subsequently, the optical photons are converted into photoelectrons at the photocathode. As a consequence of the electric field, the photoelectrons are accelerated toward the output phosphor screen. The beam is focused by electron lenses. When the photoelectrons reach the end of the vacuum tube, they impact the output phosphor, where the photoelectrons are converted into optical photons. Next, the optical photons created at the output screen are captured by a charge coupled device (CCD). The signal is amplified because more optical photons are created at the output screen than at the input screen due to the acceleration of the photoelectrons in the image intensifier.

Digital flat panel detectors

For many years, image intensifiers were used for the detection of fluoroscopic x-rays. However, digital flat panel detectors have now become a viable alternative. Digital x-ray detectors generally rely on indirect detection systems with CsI(Tl) scintillators and photodiode detector arrays^{24–26}.

Outline of this thesis

Part I

The aim of this thesis is to investigate imaging techniques for guidance of radionuclide therapy. The first part describes the development of instrumentation for guidance of radionuclide therapy.

To date, no real-time hybrid imaging modalities for interventional purposes have been developed that combine simultaneously acquired nuclear and anatomic images. Real-time functional imaging in conjunction with anatomic imaging would provide the physician with valuable information during the procedure, thereby improving therapeutic efficiency. Procedures that can potentially benefit from real-time simultaneous hybrid imaging include liver radioembolization^{7,9}, biopsies²⁷, tumor resections²⁸, and radiofrequency ablations²⁹. **Chapter 2** investigates the technical feasibility of hybrid simultaneous fluoroscopic and nuclear imaging.

Accurate determination of the system parameters that describe the position of the x-ray tube, x-ray detector, gamma camera and collimators required for hybrid simultaneous fluoroscopic and nuclear imaging, is crucial to optimize image quality. The purpose of **Chapter 3** was to develop a calibration method that estimates the system parameters used for reconstruction.

Part II

The second part of this thesis concerns the quality of SPECT images of high-energy photon-emitting isotopes. Radionuclides that emit high-energy photons (e.g. ¹³¹I and ⁹⁰Y) are often used for radionuclide therapy, and these high-energy photons can be used for imaging of the radionuclide distribution. However, the detection and collimation of high-energy photons remains a challenge. Methods to improve the quality of high-energy SPECT images are therefore introduced, and the implications of reduced image quality in clinical practice are discussed.

In SPECT using high-energy photon-emitting isotopes, such as ¹³¹I, parallel-hole collimators with thick septa are required to limit septal penetration, at the cost of sensitivity and resolution. **Chapter 4** investigates a collimator with cone-shaped holes, which was designed to limit collimator penetration while preserving resolution and sensitivity. To this end, we propose a collimator design (the parallel-cone (PC) collimator) consisting of a repetitive grid of parallel cones, which combines high spatial resolution and low septal penetration with high sensitivity, as compared with a parallel-hole collimator. The objective is to demonstrate that a single-slice prototype of the parallel-cone (PC) collimator was capable of improving the image quality of high-energy SPECT.

Radioiodine therapy with ¹³¹I is used for treatment of suspected recurrence of differentiated thyroid carcinoma. Pretherapeutic ¹²⁴I PET/CT with a low activity (~1% of ¹³¹I activity) can be performed to determine whether uptake of ¹³¹I, and thereby the desired therapeutic effect, may be expected. However, false-negative ¹²⁴I PET/CT results as compared with posttherapeutic ¹³¹I SPECT/CT have been reported by several groups³⁰⁻³⁴. The purpose of **Chapter 5** is to investigate whether the reported discrepancies may be ascribed to a difference in lesion detectability between ¹²⁴I PET/CT and ¹³¹I SPECT/CT and, hence, whether the administered ¹²⁴I activity is sufficient to achieve equal detectability.

Dosimetry for treatment monitoring requires quantitative SPECT images. However, quantitative SPECT imaging of high-energy isotopes such as ¹³¹I remains a challenge, because of scatter and

collimator penetration. The quality of SPECT images can be improved by incorporating scatter and collimator-detector-response models in the reconstruction. The goal of **Chapter 6** is to compare triple-energy-window (TEW) and Monte Carlo based scatter correction methods, as well as different methods for collimator-detector-response by performing phantom measurements.

Finally, the thesis is summarized and discussed in **Chapter 7**.

References

- 1 D.J. Kwekkeboom et al., "Treatment with the radiolabeled somatostatin analog [177 Lu-DOTA 0,Tyr3]octreotate: toxicity, efficacy, and survival.," *J. Clin. Oncol.* 26, 2124–30 (2008).
- 2 S.M. Seidlin, L.D. Marinelli, and E. Oshry, "Radioactive iodine therapy; effect on functioning metastases of adenocarcinoma of the thyroid.," *J. Am. Med. Assoc.* 132, 838–47 (1946).
- 3 M.L.J. Smits et al., "Intra-arterial radioembolization of breast cancer liver metastases: a structured review.," *Eur. J. Pharmacol.* 709, 37–42 (2013).
- 4 S.J. Wang et al., "Intratatumoral injection of rhenium-188 microspheres into an animal model of hepatoma.," *J. Nucl. Med.* 39, 1752–7 (1998).
- 5 J.H. Lawrence, "Nuclear Physics and Therapy: Preliminary Report on a New Method for the Treatment of Leukemia and Polycythemia 1.," *Radiology* 35, 51–60 (1940).
- 6 H.O. Anger, "Scintillation camera with multichannel collimators," *J. Nucl. Med.* 5, 515–31 (1964).
- 7 A.S. Kennedy and R. Salem, "Radioembolization (yttrium-90 microspheres) for primary and metastatic hepatic malignancies.," *Cancer J.* 16, 163–175 (2010).
- 8 M.A.D. Vente et al., "Yttrium-90 microsphere radioembolization for the treatment of liver malignancies: A structured meta-analysis," *Eur. Radiol.* 19, 951–959 (2009).
- 9 R. Salem and K.G. Thurston, "Radioembolization with 90Yttrium microspheres: a state-of-the-art brachytherapy treatment for primary and secondary liver malignancies: Part 1: technical and methodologic considerations," *J. Vasc. Interv. Radiol.* 17, 1251–1278 (2006).
- 10 M.L.J. Smits et al., "Holmium-166 radioembolisation in patients with unresectable, chemorefractory liver metastases (HEPAR trial): A phase 1, dose-escalation study," *Lancet Oncol.* 13, 1025–1034 (2012).
- 11 S.R. Cherry, J.A. Sorenson, and M.E. Phelps, "The Gamma Camera: Performance Characteristics," in *Phys. Nucl. Med.*, third (W.B. Saunders, Philadelphia, 2003), pp. 227–251.
- 12 S. Walrand, M. Hesse, R. Wojcik, R. Lhommel, and F. Jamar, "Optimal design of anger camera for bremsstrahlung imaging: Monte Carlo evaluation.," *Front. Oncol.* 4, 149 (2014).
- 13 P.M. Wanet, A. Sand, and J. Abramovici, "Physical and clinical evaluation of high-resolution thyroid pinhole tomography.," *J. Nucl. Med.* 37, 2017–2020 (1996).
- 14 J. Nuyts, K. Vunckx, M. Defrise, and C. Vanhove, "Small animal imaging with multi-pinhole SPECT," *Methods* 48, 83–91 (2009).
- 15 N.U. Schramm, G. Ebel, U. Engeland, T. Schurrat, M. Behe, and T.M. Behr, "High-resolution SPECT using multipinhole collimation," *Nucl. Sci. IEEE Trans.* 50, 315–320 (2003).
- 16 L.A. Shepp and Y. Vardi, "Maximum likelihood reconstruction for emission tomography," *IEEE Trans. Med. Imaging* 1, 113–122 (1982).
- 17 H.M. Hudson and R.S. Larkin, "Ordered Subsets of Projection Data," *IEEE Trans. Med. Imaging* 13, 601–609 (1994).
- 18 K. Ogawa, Y. Harata, T. Ichihara, A. Kubo, and S. Hashimoto, "A practical method for position-dependent Compton-scatter correction in single photon emission CT.," *IEEE Trans. Med. Imaging* 10, 408–12 (1991).
- 19 S.R. Cherry, "Effects of scatter on model parameter estimates in 3D PET studies of the human brain," *IEEE Trans. Nucl. Sci.* 42, 1174–1179 (1995).
- 20 J.M. Ollinger, "Model-based scatter correction for fully 3D PET.," *Phys. Med. Biol.* 41, 153–76 (1996).
- 21 M.E. Casey and E.J. Hoffman, "Quantitation in positron emission computed tomography: 7. A technique to reduce noise in accidental coincidence measurements and coincidence efficiency calibration.," *J. Comput. Assist. Tomogr.* 10, 845–50.

- 22 K.P. Willowson, M. Tapner, D.L. Bailey and QUEST team, "A multicentre comparison of quantitative (90)Y PET/CT for dosimetric purposes after radioembolization with resin microspheres: The QUEST Phantom Study.," *Eur. J. Nucl. Med. Mol. Imaging* 42, 1202–1222 (2015).
- 23 D. Brasse, P.E. Kinahan, C. Lartizien, C. Comtat, M. Casey, and C. Michel, "Correction methods for random coincidences in fully 3D whole-body PET: impact on data and image quality," *J. Nucl. Med.* 46, 859–867 (2005).
- 24 L. Lança and A. Silva, "Digital radiography detectors – A technical overview: Part 1," *Radiography* 15, 58–62 (2009).
- 25 M. Körner, C.H. Weber, S. Wirth, K.-J. Pfeifer, M.F. Reiser, and M. Treitl, "Advances in digital radiography: physical principles and system overview.," *Radiographics* 27, 675–86 (2007).
- 26 H.G. Chotas, J.T. Dobbins, and C.E. Ravin, "Principles of digital radiography with large-area, electronically readable detectors: a review of the basics.," *Radiology* 210, 595–9 (1999).
- 27 S. Tatli, V.H. Gerbaudo, C.M. Feeley, P.B. Shyn, K. Tuncali, and S.G. Silverman, "PET/CT-guided percutaneous biopsy of abdominal masses: Initial experience," *J. Vasc. Interv. Radiol.* 22, 507–514 (2011).
- 28 S. Vidal-Sicart, M.E. Rioja, P. Paredes, M.R. Keshtgar, and R.A. Valdes Olmos, "Contribution of perioperative imaging to radioguided surgery," *Q. J. Nucl. Med. Mol. Imaging* 58, 140–160 (2014).
- 29 B.J. Wood et al., "Technologies for guidance of radiofrequency ablation in the multimodality interventional suite of the future," *J. Vasc. Interv. Radiol.* 18, 9–24 (2007).
- 30 C. De Pont, S. Halders, J. Bucorius, F. Mottaghy, and B. Brans, "124I PET/CT in the pretherapeutic staging of differentiated thyroid carcinoma: Comparison with posttherapy 131I SPECT/CT," *Eur. J. Nucl. Med. Mol. Imaging* 40, 693–700 (2013).
- 31 L.S. Freudenberg, W. Jentzen, S.P. Müller, and A. Bockisch, "Disseminated iodine-avid lung metastases in differentiated thyroid cancer: A challenge to 124I PET," *Eur. J. Nucl. Med. Mol. Imaging* 35, 502–508 (2008).
- 32 G.R. Khorjekar et al., "Do Negative 124 I Pretherapy Positron Emission Tomography Scans in Patients with Elevated Serum Thyroglobulin Levels Predict Negative 131 I Posttherapy Scans?," *Thyroid* 24, 1394–1399 (2014).
- 33 G.K. Lammers, J. Paul Esser, P.C.M. Pasker, M.E. Sanson-van Praag, and J.M.H. de Klerk, "Can I-124 PET/CT predict pathological uptake of therapeutic dosages of radioiodine (I-131) in differentiated thyroid carcinoma?," *Adv. Mol. Imaging* 04, 27–34 (2014).
- 34 H.T.T. Phan et al., "The diagnostic value of 124I-PET in patients with differentiated thyroid cancer," *Eur. J. Nucl. Med. Mol. Imaging* 35, 958–965 (2008).



Toward simultaneous real-time fluoroscopic and nuclear imaging in the intervention room

Based on:

C. Beijst, M. Elschot, M.A. Viergever, H.W.A.M. de Jong, "Toward simultaneous real-time fluoroscopic and nuclear imaging in the intervention room", *Radiology*, 2016, nr. 1, vol. 278, pp. 232-238

Abstract

Purpose

To investigate the technical feasibility of hybrid simultaneous fluoroscopic and nuclear imaging.

Materials and Methods

The concept relies on placing an x-ray tube, x-ray detector and a gamma camera in one line enabling imaging of the same field of view. Since straightforward combination of these elements would block the line of views, a gamma camera geometry that looks around the x-ray tube was developed. A prototype was built using a mobile c-arm and a gamma camera with a four pinhole collimator. Using the prototype, test images were acquired and sensitivity, resolution and co-registration error were analyzed.

Results

Nuclear images (2 frames per second) were acquired simultaneously with fluoroscopic images. Depending on the point source-to-detector distance, the system resolution was 1.5 – 1.9 cm full width at half maximum (FWHM), the sensitivity $0.6 - 1.5 \times 10^{-5}$ counts per decay and the co-registration error -0.13 – 0.15 cm. With good spatial and temporal alignment of both modalities throughout the field of view, fluoroscopic images can be shown in grayscale and corresponding nuclear images in color overlay.

Conclusion

Measurements with our hybrid imaging prototype device that combines simultaneous fluoroscopic and nuclear imaging of the same field of view have demonstrated the feasibility of real time simultaneous hybrid imaging in the intervention room.

Introduction

One of the major advances in oncological imaging in the last decades has been the development of hybrid imaging modalities, including single photon emission computed tomography/computed tomography (SPECT/CT) and positron emission tomography/computed tomography (PET/CT)^{1, 2} showing both anatomical and molecular information. To date, no real-time hybrid imaging modalities for interventional purposes have been developed that combine simultaneously acquired nuclear and anatomical images. The intraoperative availability of molecular information may be achieved by registering pre-operative SPECT or PET data to intra-operative fluoroscopic or CT data³. However, the registration of the non-rigid target organs remains a challenge and the pre-operative scans may not represent the actual activity distribution. Alternatively, diagnostic hybrid systems can be employed in the intervention room, but most hybrid diagnostic systems, such as PET/CT systems, do not acquire nuclear and anatomical images simultaneously and the closed gantry geometries are not ideal for interventional applications^{4, 5}. Therefore, gamma probes and hand held gamma cameras are often used to perform radio-guided procedures, although interpretation of the information about the radioactivity distribution can be complex for lack of co-registered anatomical information.

We present an interventional fluoroscopic and nuclear imaging system that is capable of combined simultaneous fluoroscopic and nuclear imaging producing intrinsically registered hybrid images. Procedures that can potentially benefit from real time simultaneous hybrid imaging include selective internal radiation therapy (SIRT) or liver radioembolization⁶⁻⁸, biopsies^{3, 9}, tumor resections¹⁰ and radiofrequency ablations¹¹. Real time functional imaging in concert with anatomical imaging would provide the physician with valuable information during the procedure, and thereby improve therapeutic efficiency. As an example, the SIRT procedure may be drastically shortened if direct feedback about extra-hepatic activity of the radionuclide is available during injection of the therapeutic microspheres in the intervention room.

The goal of this study is to investigate the technical feasibility of hybrid simultaneous fluoroscopic and nuclear imaging.

Methods

The gamma camera used in this study was provided by Siemens Healthcare (Erlangen, Germany). The authors had control of the data and the information submitted for publication.

Device design

The x-ray tube, the gamma camera and the x-ray detector are placed in one line to enable imaging of the same field of view. Straightforward geometric configurations of the gamma camera and the c-arm in one line will block the line of sight of either one of the modalities. This problem was solved by placing the gamma camera behind the x-ray tube and four pinholes around the x-ray tube to create stereoscopic pinhole views of the field of view. The pinholes were positioned such that the center of the three-dimensional field of view was imaged by all four pinholes (Figure 2.1).

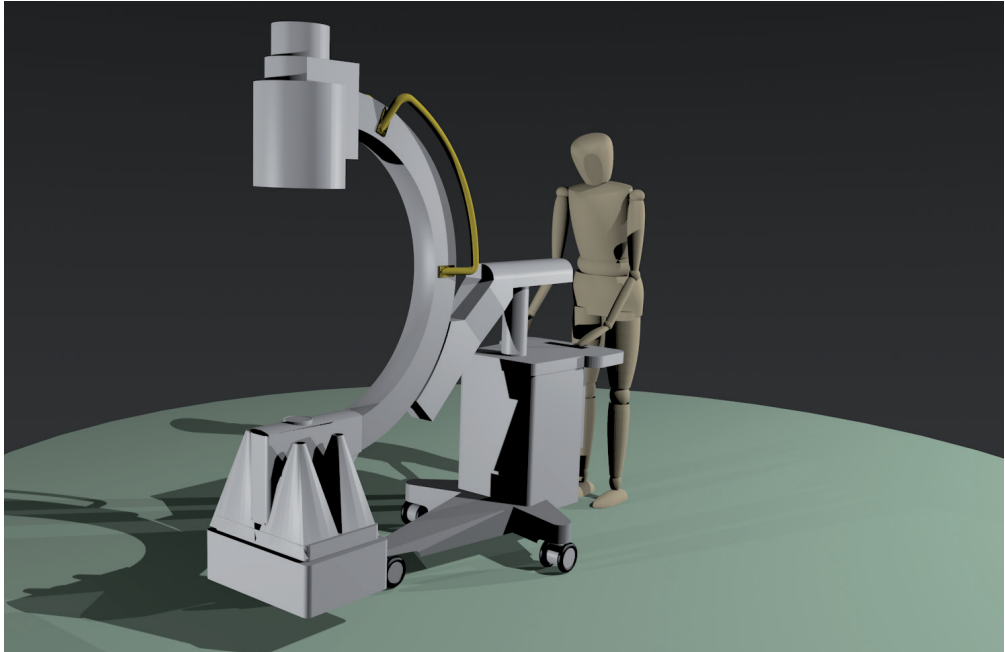


Figure 2.1 Rendering and prototype of the interventional fluoroscopic and nuclear imaging system.

Table 2.1 Geometry of the hybrid c-arm.

Hybrid c-arm geometry	
Distance pinhole – NaI(Tl) crystal	38,7 cm
Distance pinhole - x-ray detector	79,0 cm
Diameter image intensifier	22,9 cm
Pinhole diameter	0,5 cm

Prototype

A prototype of the interventional fluoroscopic and nuclear imaging system was built, see Figure 2.1. A Diacam gamma camera (Siemens Healthcare, Erlangen, Germany) with a 9.5 mm NaI(Tl) scintillation crystal was used to acquire nuclear images and a BV29 c-arm (Philips Healthcare, Best, The Netherlands) with a 22.9 cm image intensifier was used to acquire fluoroscopic images. Four 5 mm lead pinholes were fabricated and placed next to the x-ray tube. Lead shielding of at least 4 mm thickness was applied around the pinholes and the gamma camera to prevent uncollimated photons from interacting with the scintillation crystal. The dimensions of the prototype are given in Table 2.1. Scintigraphic images were acquired on a 256 x 256 grid with 2.4 x 2.4 mm² pixel size. The gamma camera was subdivided in four quadrants; one 128 x 128 quadrant for each individual pinhole (Figure 2.2).

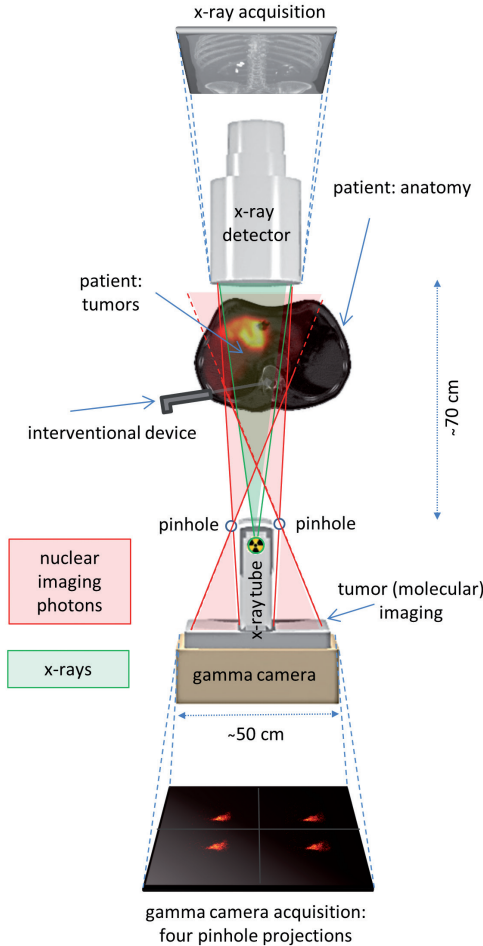


Figure 2.2 Schematic drawing of the hybrid c-arm showing the field of view of the pinhole collimator and the x-ray photons.

Reconstruction, co-registration and overlay

The positioning of the pinhole collimators allows conversion of the pinhole projections into one nuclear image that overlaps with the fluoroscopic image.

In the past, several techniques have been developed to merge information from a limited number of projections into a single image (e.g.¹²). Tomosynthesis is now often applied as an extension to mammography¹³⁻¹⁵.

For conversion, first the 3D activity distribution was iteratively estimated from the four pinhole projections using a maximum-likelihood expectation-maximization (MLEM) reconstruction algorithm. Resolution recovery was incorporated in both the forward- and the back-projection step of the reconstruction algorithm by analytical determination of the point spread function, taking into account the finite dimensions of the cone opening and pinhole edge penetration¹⁶⁻¹⁸.

Next, the 3D activity distribution was forward projected along the direction of the x-ray photons, creating a nuclear image taken from the same point of view as the x-ray tube. Subsequently, multimodality images were created showing fluoroscopic images in grayscale and nuclear images in color overlay.

Fluoroscopic images were acquired at 25 frames per second, and corrected for image non-linearities including pincushion and barrel distortions¹⁹. Nuclear images were acquired at a rate of 2 frames per second. Results of simultaneous fluoroscopic and nuclear acquisitions were visualized at 5 frames per second. For visual purposes the nuclear images were supersampled by means of interpolation to match the spatial and temporal sizes of the visualized fluoroscopic images²⁰.

Image quality characterization

Measurements were performed with a ^{99m}Tc point source placed on thirty different positions between 1 and 30 cm from the x-ray detector. The point source was positioned on the central line through the x-ray tube and the x-ray detector. To create a phantom visible for both modalities, a 3 mm spherical cavity in a polymethyl methacrylate (PMMA) cylinder was filled with 2.0 MBq ^{99m}Tc. A 60 s acquisition was performed for each location of the point source, using a 15% energy window centered at 140 keV. The measured projections were used to reconstruct a volume of 64 x 64 x 64 voxels with a 4.8 x 4.8 x 4.8 mm³ voxel size. A reconstruction of the nuclear image was performed using 10 MLEM iterations. Fluoroscopic images were acquired with a 45 kV tube voltage and 0.20 mA tube current. Subsequently, the full width at half maximum (FWHM) of the reconstructed and co-registered nuclear projection image, the sensitivity of the gamma camera with collimator, and the overlap error between both modalities were calculated. Theoretical values of the resolution were calculated for comparison²¹. The co-registration error was determined by calculating the distance between the centers of gravity of the fluoroscopic and the nuclear image.

Intermodal spill-over

X-ray photons may undesirably be detected by the gamma camera, for instance directly due to insufficient shielding or through the pinholes via (back-)scattering. Two sets of measurements were performed using x-ray tube voltages between 40 and 100 kV; the first with an empty field of view (with air) and the second with 10 cm of polymethyl methacrylate (PMMA) in front of the x-ray detector acting as a scatter medium. The scatter material consisted of ten stacked in-house manufactured 40 x 40 x 1 cm PMMA plates with a density of 1.18 g/cm³. The x-ray tube was switched on during the entire 5 s scintigraphic acquisition.

Phantoms

A syringe with a droplet (0.02 ml) of 25.9 MBq ^{99m}Tc solution was moved through the combined field of view of both modalities. The gamma camera acquired 60 frames of 500 ms. The MLEM algorithm with 3 iterations was used to reconstruct the 3D activity distribution for each time frame. Fluoroscopic images were acquired with a 50 kV tube voltage and 0.44 mA tube current.

Subsequently, the IEC NEMA 2007 phantom (PTW, Freiburg, Germany) with two out of six spheres (17 mm and 37 mm) filled with 3.7 MBq/ml was rotated under an angle of 16 degrees in the combined field of view of both modalities. The size of the anthropomorphic phantom is 30.5 cm (long axis) x 24.1 cm (short axis) x 24.1 cm (height). The background compartment was

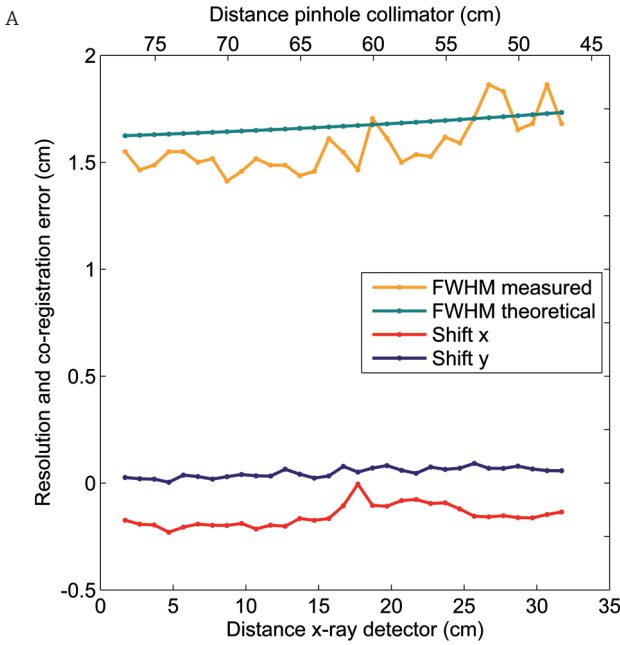
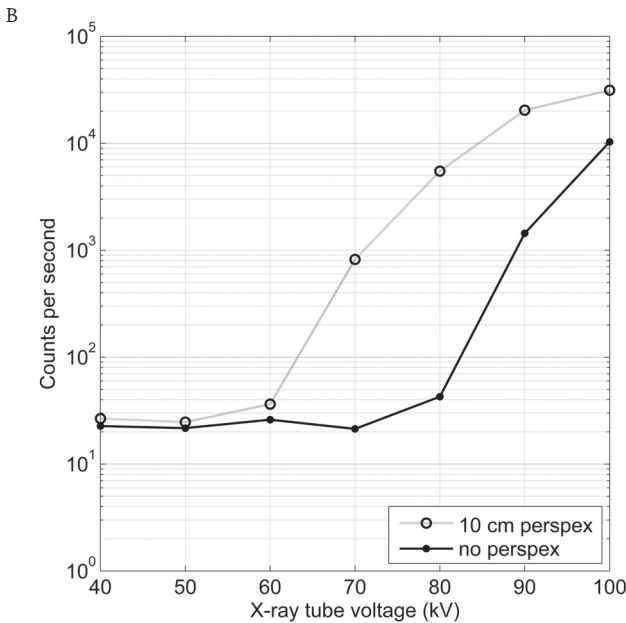


Figure 2.3 Quantitative performance measurements of the prototype showing (A) the resolution and the co-registration error of the nuclear projection image as a function of distance from the x-ray detector and (B) the number of counts measured in the gamma camera energy window as a function of x-ray tube voltage.



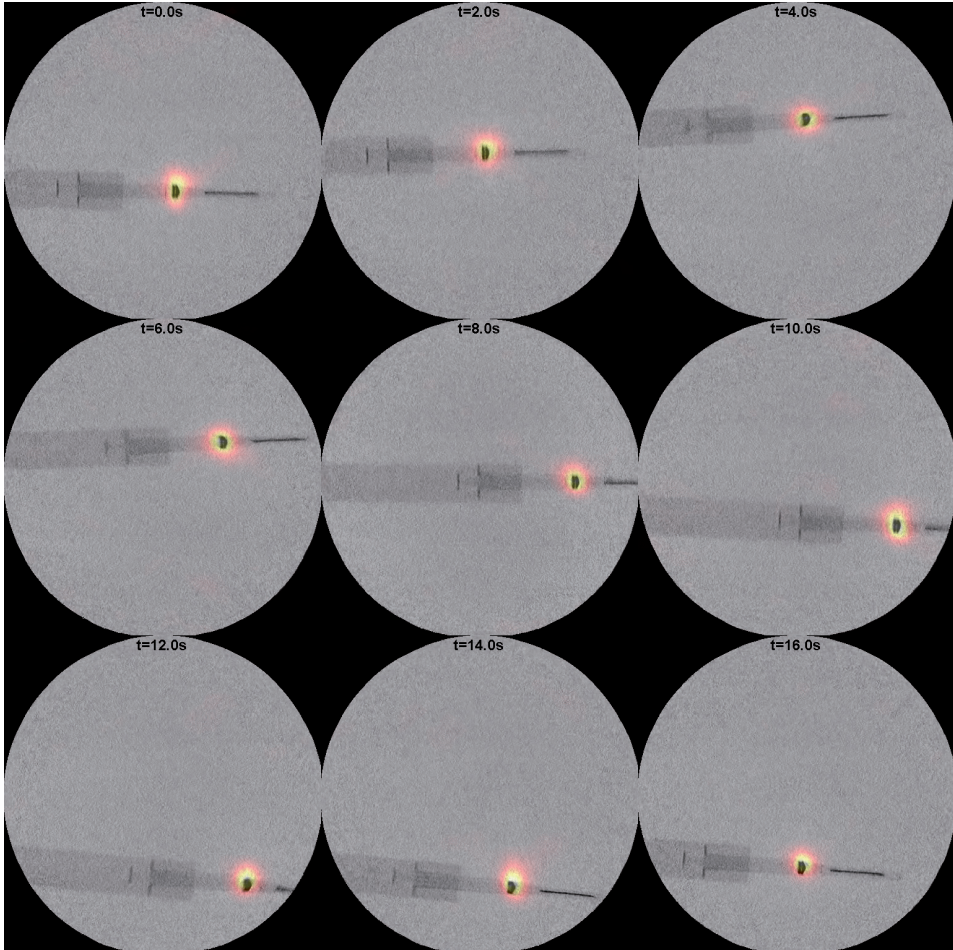


Figure 2.4 Montage of frames from a simultaneous hybrid acquisition of a 25.9 MBq ^{99m}Tc syringe with fluoroscopic images in grayscale and nuclear images in color overlay.

not filled with water in order to enhance contrast for assessment of intermodal co-registration. The gamma camera acquired 100 frames of 500 ms. During the entire acquisition, fluoroscopic images were acquired with a 44 kV tube voltage and 0.16 mA tube current.

Results

Quantitative analysis

The results of ^{99m}Tc point source measurements to analyze resolution, sensitivity and co-registration errors are shown in Figure 2.3A. The FWHM of nuclear point source images was in the range 1.5-1.9 cm. The co-registration error was between -0.13 and 0.15 cm, which is roughly an

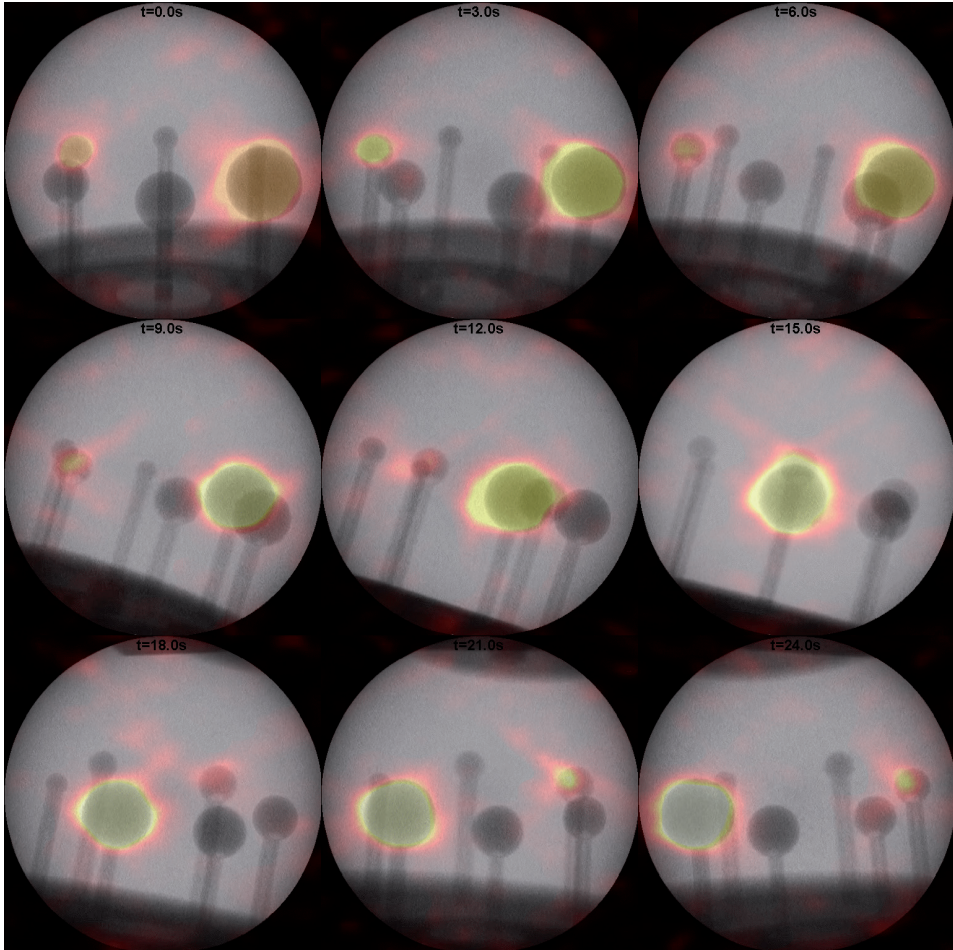


Figure 2.5 Montage of frames from a simultaneous hybrid acquisition of a 3.7 MBq/ml ^{99m}Tc phantom with fluoroscopic images in grayscale and nuclear images in color overlay.

order of magnitude smaller than the resolution of the nuclear image. The sensitivity was $0.6 - 1.5 \times 10^{-5}$ counts per decay.

Intermodal spill-over

Figure 2.3B shows the amount of counts in the 15% energy window centered at 140 keV, for different values of the x-ray tube current. The measurements show that the amount of counts increased rapidly as the tube voltage increased beyond 60 kV (with scatter material) and 80 kV (without scatter material).

Phantoms

A syringe with 25.9 MBq ^{99m}Tc was moved through the combined field of view, as shown in Figure 2.4. With good spatial and temporal overlap of both modalities, a montage of fluoroscopic images is shown in grayscale and nuclear images in color overlay. No artifacts could be detected in the fluoroscopic images, which shows that fluoroscopic imaging is unaffected by the presence of the radioactive tracer, the pinholes or the gamma camera. Similar results were obtained using a IEC NEMA 2007 phantom with 17 mm and 37 mm spheres filled with 3.7 MBq/ml. A montage of acquired hybrid images is shown in Figure 2.5.

Discussion

Real time hybrid imaging promises to improve radio-guided procedures. In this study, measurements with a prototype setup demonstrate that real-time simultaneous fluoroscopic and nuclear imaging of the same field of view is feasible. This was achieved without adding constraints to the traditional geometry of the C-arm, to fluoroscopic imaging and to the interventional set-up. The co-registration error was shown to be an order of magnitude smaller than the in-plane resolution of the nuclear image. The fluoroscopic/nuclear hybrid images demonstrated good spatial and temporal overlap.

The purpose of the hybrid c-arm is not to compete with diagnostic hybrid imaging devices in terms of image parameters such as resolution and contrast. The proposed system is rather aimed at guiding interventional oncological procedures. The intrinsic spatial co-registration of the fluoroscopic and nuclear images is a great advantage in supporting the dynamic procedures in the intervention room.

Constructing a real prototype can prove the technical feasibility of a system, but it may also reveal unforeseen obstacles. Prototype measurements showed substantial spill-over of x-rays into the nuclear images, even at kV settings well below the lower energy threshold of the nuclear imaging (126 keV). Pile-up effects in the gamma camera can cause multiple x-ray photons to be detected as a single gamma photon, potentially causing x-ray photons to be counted in the energy window. Possible solutions to the spill-over problem include anti-synchronization of the nuclear acquisition with pulsed fluoroscopy²². Assuming that fluoroscopic images are acquired with a frequency of 5 fps and a pulse width of 5 ms, only 2.5% of the counts would theoretically be lost to prevent detection of possibly scattered x-rays in the gamma camera energy window. Furthermore, the effects of x-ray photon pileup can be overcome by using detectors with a higher temporal resolution than detectors equipped with a NaI(Tl) scintillation crystal, such as a LYSO or LaBr₃ scintillation crystal with a much shorter decay time^{23, 24}.

Since the C-arm used did not allow pulsed fluoroscopy to prevent the spill-over, the measurements of the NEMA phantom were performed without water in the background compartment to limit the effects of (back-)scattered x-ray photons.

In this prototype set-up using a standard desktop PC and software not optimized for speed, the average post-processing time for a single visualization frame was approximately 3 s, allowing only retrospective image evaluation. Several groups have shown that significant acceleration can be achieved by parallel processing on graphic processing units (GPUs)²⁵. Therefore, we believe real time processing is feasible when optimized hardware and software is used.

Future research will be aimed at improving the image quality while maintaining the system's capability of simultaneous hybrid imaging. Larger digital flat panel x-ray detectors capable of imaging the entire patient may be more practical for clinical procedures than the relatively small image intensifier with a diameter of 22.9 cm used for the prototype. Moreover, the application of smaller detectors for nuclear imaging that require less shielding and of parallel hole collimators may improve sensitivity, resolution and allow a flexible light-weight design. The resolution and sensitivity required to provide the physician with clinically relevant information will strongly depend on the clinical application. This will be assessed in future research by using the hybrid c-arm in (pre-)clinical settings as, e.g. radioembolization.

In conclusion, a novel hybrid imaging prototype that combines simultaneous fluoroscopic and nuclear imaging of the same field of view has been proposed. Measurements with our concept device demonstrated that real time hybrid imaging in the intervention room is feasible.

References

- 1 S. Basu and A. Alavi, "SPECT-CT and PET-CT in Oncology - An Overview," *Curr. Med. Imaging. Rev.* 7, 202–209 (2011).
- 2 D. Delbeke and M.P. Sandler, "The role of hybrid cameras in oncology," *Semin. Nucl. Med.* 30, 268–280 (2000).
- 3 S. Tatli, V.H. Gerbaudo, M. Mamede, K. Tuncali, P.B. Shyn, and S.G. Silverman, "Abdominal masses sampled at PET/CT-guided percutaneous biopsy: initial experience with registration of prior PET/CT images.," *Radiology* 256, 305–311 (2010).
- 4 B. Klaeser, M.D. Mueller, R.A. Schmid, C. Guevara, T. Krause, and J. Wiskirchen, "PET-CT-guided interventions in the management of FDG-positive lesions in patients suffering from solid malignancies: Initial experiences," *Eur. Radiol.* 19, 1780–1785 (2009).
- 5 S. Tatli, V.H. Gerbaudo, C.M. Feeley, P.B. Shyn, K. Tuncali, and S.G. Silverman, "PET/CT-guided percutaneous biopsy of abdominal masses: Initial experience," *J. Vasc. Interv. Radiol.* 22, 507–514 (2011).
- 6 S.A. Gulec and Y. Fong, "Yttrium 90 microsphere selective internal radiation treatment of hepatic colorectal metastases.," *Arch. Surg.* 142, 675–682 (2007).
- 7 A.S. Kennedy and R. Salem, "Radioembolization (yttrium-90 microspheres) for primary and metastatic hepatic malignancies.," *Cancer J.* 16, 163–175 (2010).
- 8 M.A.D. Vente et al., "Yttrium-90 microsphere radioembolization for the treatment of liver malignancies: A structured meta-analysis," *Eur. Radiol.* 19, 951–959 (2009).
- 9 K. Kobayashi et al., "Image-guided biopsy: what the interventional radiologist needs to know about PET/CT," *Radiographics* 32, 1483–1501 (2012).
- 10 S. Vidal-Sicart, M.E. Rioja, P. Paredes, M.R. Keshtgar, and R.A. Valdes Olmos, "Contribution of perioperative imaging to radioguided surgery," *Q. J. Nucl. Med. Mol. Imaging* 58, 140–160 (2014).
- 11 B.J. Wood et al., "Technologies for guidance of radiofrequency ablation in the multimodality interventional suite of the future," *J. Vasc. Interv. Radiol.* 18, 9–24 (2007).
- 12 R.A. Crowther, L.A. Amos, J.T. Finch, D.J. De Rosier, and A. Klug, "Three dimensional reconstructions of spherical viruses by fourier synthesis from electron micrographs.," *Nature* 226, 421–425 (1970).
- 13 J.T. Dobbins III and D.J. Godfrey, "Digital x-ray tomosynthesis: current state of the art and clinical potential," *Phys Med Biol* 48, R65–R106 (2003).
- 14 D.G. Grant, "Tomosynthesis: a three-dimensional radiographic imaging technique.," *IEEE Trans. Biomed. Eng.* 19, 20–28 (1972).
- 15 M.J. Yaffe and J.G. Mainprize, "Digital tomography: technique," *Radiol. Clin. North Am.* 52, 489–497 (2014).
- 16 G. Bal and P.D. Acton, "Analytical derivation of the point spread function for pinhole collimators.," *Phys. Med. Biol.* 51, 4923–4950 (2006).
- 17 S.D. Metzler, J.E. Bowsher, K.L. Greer, and R.J. Jaszczak, "Analytic determination of the pinhole collimator's point-spread function and RMS resolution with penetration," *IEEE Trans. Med. Imaging* 21, 878–887 (2002).
- 18 C. Vanhove, A. Andreyev, M. Defrise, J. Nuyts, and A. Bossuyt, "Resolution recovery in pinhole SPECT based on multi-ray projections: a phantom study," *Eur. J. Nucl. Med. Mol. Imaging* 34, 170–180 (2007).

- 19 W.A. Wallace and F. Johnson, "Detection and correction of geometrical distortion in X-ray fluoroscopic images," *J. Biomech.* 14, 123–125 (1981).
- 20 R.G. Gould, M.J. Lipton, P. Mengers, and R. Dahlberg, "Investigation of a video frame averaging digital subtraction fluoroscopic system," *Proc. SPIE* 0314, 184–190 (1981).
- 21 S.D. Metzler, J.E. Bowsher, M.F. Smith, and R.J. Jaszczak, "Analytic determination of pinhole collimator sensitivity with penetration," *IEEE Trans. Med. Imaging* 20, 730–741 (2001).
- 22 D.B. Plewes and E. Vogelstein, "Grid controlled x-ray tube switching time: implications for rapid exposure control," *Med. Phys.* 11, 693–696 (1984).
- 23 T.K. Lewellen, "Recent developments in PET detector technology," *Phys. Med. Biol.* 53, R287–R317 (2008).
- 24 T.E. Peterson and L.R. Furenlid, "SPECT detectors: the Anger camera and beyond," *Phys. Med. Biol.* 56, R145–R182 (2011).
- 25 A. Eklund, P. Dufort, D. Forsberg, and S.M. LaConte, "Medical image processing on the GPU - Past, present and future," *Med. Image Anal.* 17, 1073–1094 (2013).



Multimodality calibration for simultaneous fluoroscopic and nuclear imaging

Based on:

C. Beijst, M. Elschot, S. van der Velden, H.W.A.M de Jong, "Multimodality calibration for simultaneous fluoroscopic and nuclear imaging", *Submitted for publication*

Abstract

Background

Simultaneous real time fluoroscopic and nuclear imaging could benefit image guided (oncological) procedures. To this end, a hybrid modality is currently being developed by our group, by combining a c-arm with a gamma camera and four pinhole collimators. Accurate determination of the system parameters that describe the position of the x-ray tube, x-ray detector, gamma camera and collimators is crucial to optimize image quality. The purpose of this study was to develop a calibration method that estimates the system parameters used for reconstruction.

Methods

A multimodality phantom consisting of five point sources was created. First, nuclear and fluoroscopic images of the phantom were acquired at several distances from the image intensifier. The system parameters were acquired using physical measurement and multimodality images of the phantom were reconstructed. The resolution and co-registration error of the point sources were determined as a measure of image quality. Next, the system parameters were estimated using a calibration method, which adjusted the parameters in the reconstruction algorithm, until the resolution and co-registration were optimized. For evaluation, multimodality images of a second set of phantom acquisitions were reconstructed using calibrated parameter sets. Subsequently, the resolution and co-registration error of the point sources were determined as a measure of image quality. In addition, simultaneously acquired fluoroscopic and nuclear images of two moving syringes were obtained with parameter sets from before and after calibration.

Results

The mean FWHM was lower after calibration (0.94 cm) than before calibration (1.01 cm). The mean co-registration error was lower after calibration (0.14 cm) than before calibration (1.17 cm). The simultaneously acquired fluoroscopic and nuclear images showed improved co-registration after calibration as compared with before calibration.

Conclusions

A calibration method was presented that improves the resolution and co-registration of simultaneously acquired hybrid fluoroscopic and nuclear images by estimating the geometric parameter set as compared with a parameter set acquired by direct physical measurement.

Introduction

A major development in imaging for oncology during the last decades has been the development of hybrid imaging modalities such as PET/CT and SPECT/CT¹. These systems are mostly used for diagnostic purposes, although PET/CTs have also been employed for image guided (oncological) procedures². However, the closed gantry geometry and the lack of real-time simultaneous imaging are suboptimal for interventional applications. Therefore, a modality for real-time simultaneous fluoroscopic and nuclear imaging is currently being developed by our group, by combining a c-arm and a gamma camera with a four-pinhole collimator³.

Real-time simultaneous fluoroscopic and nuclear imaging has the potential to provide the physician with valuable information during interventional procedures. Examples of procedures that could benefit from real-time hybrid imaging are biopsies⁴ and liver radioembolization⁵.

Hybrid nuclear imaging modalities require a correct description of the acquisition geometry for accurate reconstruction and co-registration of images. In SPECT/CT, for example, these geometric parameters include mechanical offsets of the gamma cameras, electronic shifts, the rotation radius and the relative position of modalities. Incorrect description of the SPECT/CT acquisition geometry can result in loss of resolution, image deformation and co-registration errors, especially for pinhole and cone beam collimators because of their magnifying properties⁶⁻⁸. The geometric parameters can be determined by direct physical measurement or by using calibration methods⁹⁻¹¹.

A correct description of the acquisition geometry is also required for the fluoroscopic and nuclear imaging c-arm, to prevent resolution loss, image deformation and co-registration errors. The parameters that describe the geometry of the hybrid c-arm include the relative position of the gamma camera, collimators, x-ray tube and x-ray detector (image intensifier). The purpose of this study was to develop a calibration method which improves the resolution and co-registration of simultaneously acquired hybrid fluoroscopic and nuclear images, by estimating the geometric parameter set used for reconstruction and co-registration using phantom measurements.

Methods

Prototype

Simultaneous fluoroscopic and nuclear imaging of the same field of view (FOV) is feasible when an x-ray tube, an x-ray detector and a gamma camera with a four pinhole collimator are placed in one line³. A prototype of this interventional fluoroscopic and nuclear imaging system was previously built using a Siemens Diacam gamma camera with a 9.5 mm NaI(Tl) scintillation crystal and a Philips BV29 c-arm with a 22.9 cm image intensifier (Figure 3.1)³. A collimator with four 5 mm lead pinholes was especially designed to collimate gamma rays around the x-ray tube. At least 4 mm of lead shielding was applied around the four-pinhole collimator to ensure that uncollimated photons remained undetected.

Nuclear image reconstruction

A reconstruction algorithm was previously developed to create a nuclear image that overlapped with the fluoroscopic image, by conversion of the four pinhole projections into a single image³. In short, the conversion of the four pinhole projections involves two steps. First, the four

projections are used to reconstruct a three-dimensional distribution with an iterative maximum likelihood expectation maximization (MLEM) algorithm¹². The forward and backward projection of the reconstruction step incorporate resolution recovery by modeling the point response geometrically, taking into account the size of the pinhole opening and including penetration of the pinhole edges¹³⁻¹⁵. Second, the three-dimensional activity distribution is projected onto the x-ray detector by performing a cone-beam projection that is geometrically identical to the fluoroscopic projection. Hybrid fluoroscopic and nuclear images are subsequently obtained by showing the fluoroscopic image in grayscale and the nuclear image in color overlay. The process of creating hybrid fluoroscopic and nuclear images is shown schematically in Figure 3.2.

Fluoroscopic distortion correction

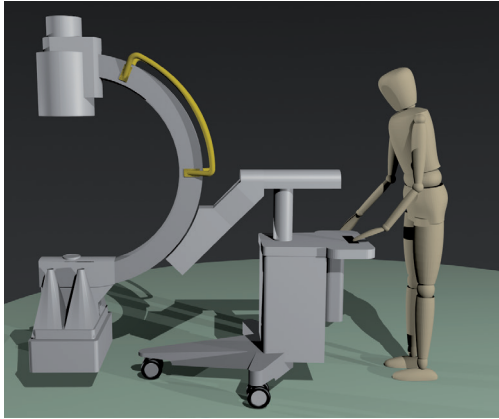
The fluoroscopic images were corrected for distortion effects of the image intensifier, before being overlapped with nuclear images. Distortion of fluoroscopic images as acquired by image intensifiers is a relatively common problem, and several strategies have been described in literature that involve the acquisition of a repetitive grid of features to estimate the position dependent displacement¹⁶⁻¹⁹.

For correction, fluoroscopic acquisitions of a line pattern phantom with 4 mm wide strips of lead were performed, using a 45 kV tube voltage and a 0.2 mA tube current. The grid acquisition as shown in Figure 3.3A was obtained by combining acquisitions of the lead grid in x and y direction through subtraction. To obtain an image with enhanced grid points, a threshold was applied and binary erosion was performed, using in-house developed Matlab (MathWorks Inc., Natick, MA, USA) code. Subsequently, the center of gravity of the enhanced grid points was calculated to determine their position. For each acquired grid point, the measured position was compared to the expected position. In this manner, the position dependent grid point distortion in x and y direction was determined (Figure 3.3B). This was translated into a distortion matrix with the size of the fluoroscopic image for both the x and y direction by bi-linear interpolation. This distortion matrix was used to obtain corrected fluoroscopic images, as shown in Figure 3.3B.

Parameter calibration

To improve the resolution and co-registration of simultaneously acquired fluoroscopic and nuclear images, we developed a calibration method that estimates the geometric parameter set. An overview of the calibrated geometric parameters is given in Table 3.1. A correct estimate of the pinhole positions is required to prevent resolution loss of the nuclear image, whereas a correct estimation of the effective diameter of the x-ray detector was important for correct scaling of fluoroscopic images with respect to the nuclear images. The position of the x-ray detector was important for co-registration of fluoroscopic and nuclear images. To serve as an initial guess for the calibration, the geometric parameter set was determined by direct physical measurement. The pinhole positions were obtained using measuring tape. The x-ray tube and x-ray detector were placed in front of the center of the gamma camera as accurately as possible by visual inspection, to minimize the shift with respect to the center of the coordinate system. Consequently, the shift of the x-ray tube and detector with respect to the center of the gamma camera were initially assumed to be zero.

A



B

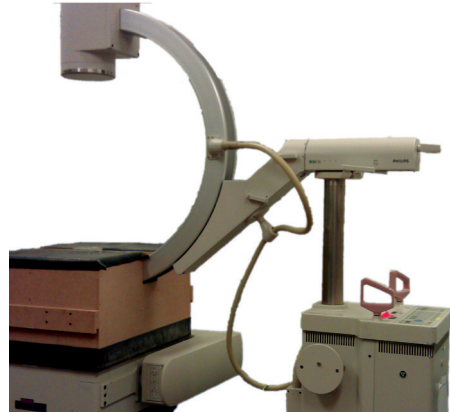


Figure 3.1 Rendering (A) and picture (B) of the interventional fluoroscopic and nuclear imaging system.

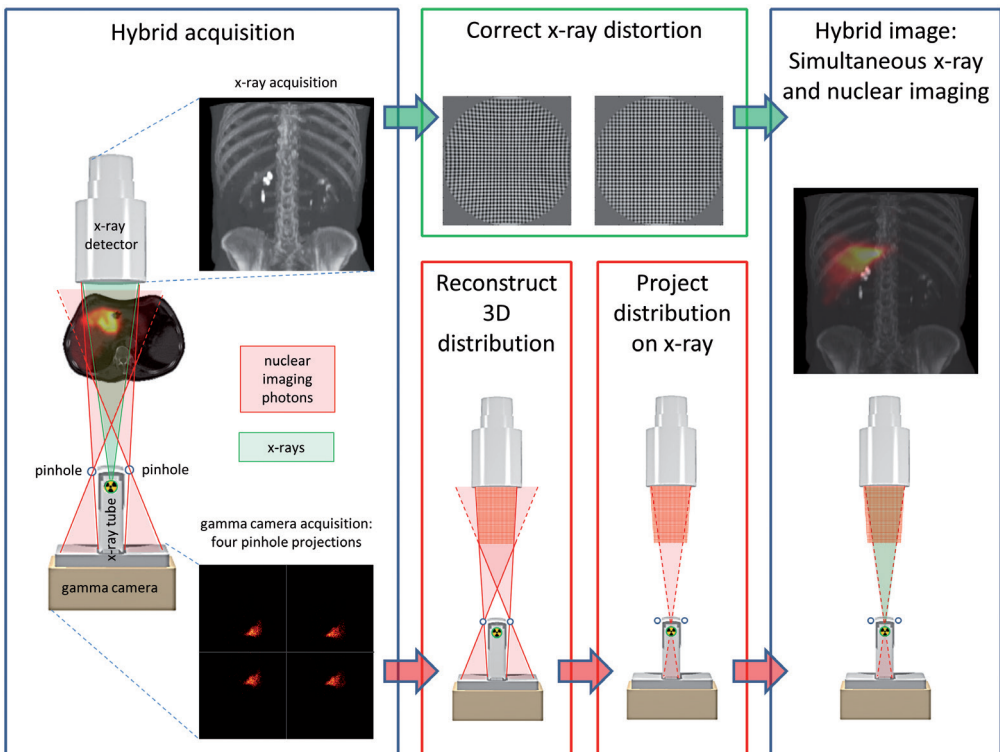


Figure 3.2 Flowchart showing steps involved in post-processing of acquired hybrid simultaneous images

For calibration purposes, acquisitions were performed of a five-point-source phantom. The point sources were visible on both fluoroscopic and nuclear images and were created by filling a 3 mm spherical cavity in a polymethyl methacrylate cylinder with a diameter and thickness of 2 cm (Figure 3.4). The phantom was positioned at 4.7, 10.7, 16.7, 22.7 and 28.7 cm distance from the x-ray detector, resulting in a total of 25 point source positions used for calibration.

Fluoroscopic images were acquired with a 45 kV tube voltage and a 0.2 mA tube current. Nuclear images were acquired on 128 x 128 pixels per projection with 2.4 x 2.4 mm² pixel size in 300 s per view. Reconstructions were performed with 5 MLEM iterations to obtain a volume of 128 x 128 x 128 voxels with a 2.4 x 2.4 x 2.4 mm³ voxel size for evaluation. The calibration required a computation time of approximately 3 hours on a standard workstation.

A two-step calibration of resolution and co-registration was performed in Matlab (MathWorks Inc., Natick, MA, USA) to obtain a calibrated parameter set, as explained below and as shown schematically in Figure 3.5. As a measure of resolution, the FWHM of the three-dimensional activity distribution in the x and y direction was determined. The FWHM was calculated by extracting profiles from the reconstructed activity distribution through the maximum voxel in x and y direction, which were fitted with a Gaussian. The positions of the point sources on fluoroscopic and nuclear images were determined by applying a threshold and subsequent calculation of the centers of gravity. The co-registration error was determined by calculating the distance between the centers of gravity of the fluoroscopic and nuclear images.

Step 1: calibration pinhole positions

First, the resolution of the nuclear image was optimized by performing reconstructions for varying x and y components of the pinhole positions, and the resulting resolution was determined for each pinhole configuration. A non-linear trust-region-reflective sum-of-squares minimization algorithm was used to determine the optimal pinhole positions in terms of phantom resolution^{20, 21}. Trust-regions were used to prevent local convergence, because in exploratory experiments not presented in this study we observed that local convergence was likely to occur without the use of trust-regions.

Step 2: calibration effective size x-ray detector

Once the optimal pinhole positions were found, the effective diameter of the x-ray detector was estimated, to improve the co-registration. The effective diameter was defined as the cross-section of the image intensifier that was actually used for fluoroscopic imaging, which determined the effective diameter of the fluoroscopic images after correction. Therefore, the distance between the upper and lower point source, as well as the distance between the left and right point source were calculated for both fluoroscopic and nuclear images. The effective diameter was scaled such that the mean of these distances over all positions of the phantom were equal.

Step 3: calibration position x-ray detector

Next, the mean shift between fluoroscopic and nuclear images was corrected for by incorporating the position of the x-ray detector in x and y direction. The position of the x-ray detector was estimated by calculating the mean shift between point sources on fluoroscopic images and nuclear images in x and y direction.

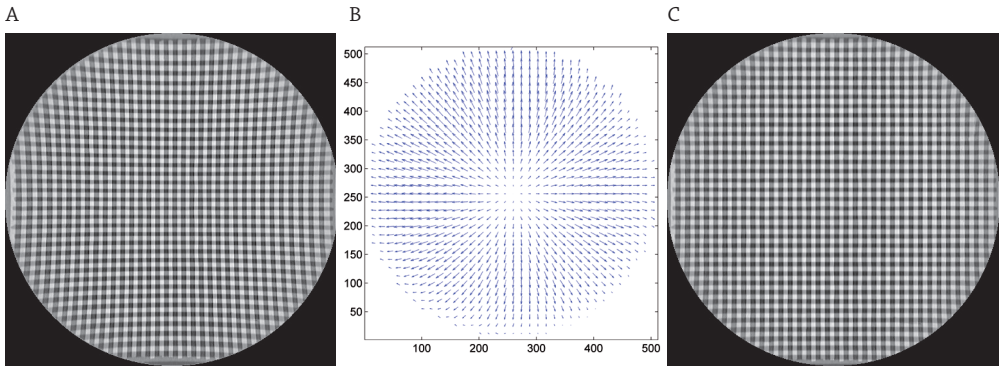


Figure 3.3 Fluoroscopic image of the lead grid before distortion correction (A), the acquired distortion matrix (B) and fluoroscopic image of the lead grid after distortion correction (C).

Table 3.1 Geometric parameters used by the co-registration and overlap algorithm.

Symbol	Explanation
$x_{\text{pinhole}, n}$	X coordinate of pinhole nr. $n=1,2,3,4$
$y_{\text{pinhole}, n}$	Y coordinate of pinhole nr. $n=1,2,3,4$
$d_{\text{xray detector}}$	Effective diameter x-ray detector
$x_{\text{xray detector}}$	Shift of x-ray detector with respect to center of coordinate system
$y_{\text{xray detector}}$	Shift of x-ray detector with respect to center of coordinate system

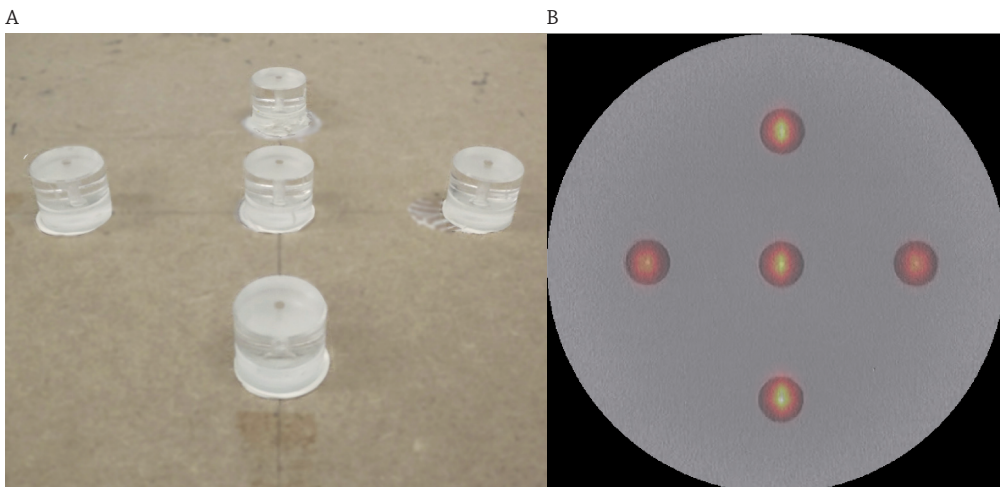


Figure 3.4 A picture of the five-point-source phantom (A) and a hybrid acquisition of the phantom showing the fluoroscopic image in grayscale and nuclear image in color overlay (B).

Evaluation

After calibration, the resolution of the nuclear images and the multimodality co-registration error were evaluated with a different set of point source measurements, to avoid using the same measurements for calibration and evaluation. For evaluation, the phantom was positioned at 1.7, 7.7, 13.7, 19.7 and 25.7 cm distance from the x-ray detector, resulting in a total of 25 point source positions used for evaluation. Subsequently, the mean resolution and the mean co-registration error were determined at each distance for a geometric parameter set that was acquired by direct physical measurement and geometric parameter sets estimated using the calibration method.

Simultaneous fluoroscopic and nuclear acquisition

To illustrate the co-registration of simultaneously acquired fluoroscopic and nuclear images in a dynamic situation, acquisitions were performed of two syringes containing 49 MBq of ^{99m}Tc . The syringes were connected via a three-way-valve and the activity was flowing from one syringe into the other during the acquisition. Post-processing was performed twice, using a geometric parameter set that was acquired by direct physical measurement and using a geometric parameter set estimated by the calibration method.

Nuclear images were acquired with a frame rate of 2 frames per second. Reconstructions were performed with 5 MLEM iterations. Fluoroscopic images were acquired with a 43 kV tube voltage and a 0.14 mA tube current at 25 frames per second. Hybrid fluoroscopic and nuclear acquisitions were visualized at 5 frames per second. The nuclear images were super-sampled by means of interpolation for visual purposes to match the spatial and temporal matrix sizes of the visualized x-ray images^{3,22}.

Results

Parameter calibration

Table 3.2 shows the parameter values before, during and after calibration. Figure 3.6A-D shows the full width at half maximum (FWHM) of the reconstructed activity distribution in the xy plane (perpendicular to x-ray beam) as a function of distance from the pinholes. The mean FWHM was lower for the parameter set estimated by the calibration method (0.94 cm; Figure 3.6D) than for the parameter set acquired by direct measurement (1.01 cm; Figure 3.6A), as shown in Table 3.3. As expected, the resolution was improved by the resolution calibration (step 1), and remained unchanged during the subsequent calibration steps.

Figure 3.6E-H shows the co-registration error as a function of distance from the pinholes. The mean co-registration error was lower for the parameter set estimated by the calibration method (0.14 cm; Figure 3.6E) than for the parameter set acquired by direct physical measurement (1.17 cm; Figure 3.6H). The spread of the co-registration error was reduced when the effective size of the x-ray detector was calculated (Figure 3.6G), whereas the mean co-registration error was reduced significantly after calibrating the position of the x-ray detector (Figure 3.6H), as shown in Table 3.3.

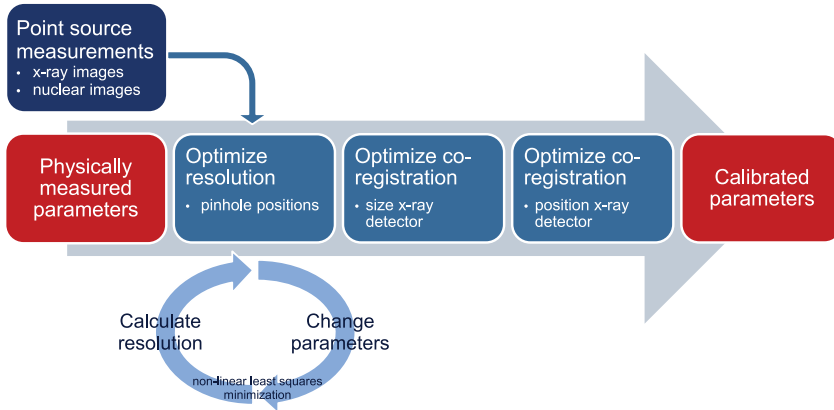


Figure 3.5 Schematic overview of the calibration procedure.

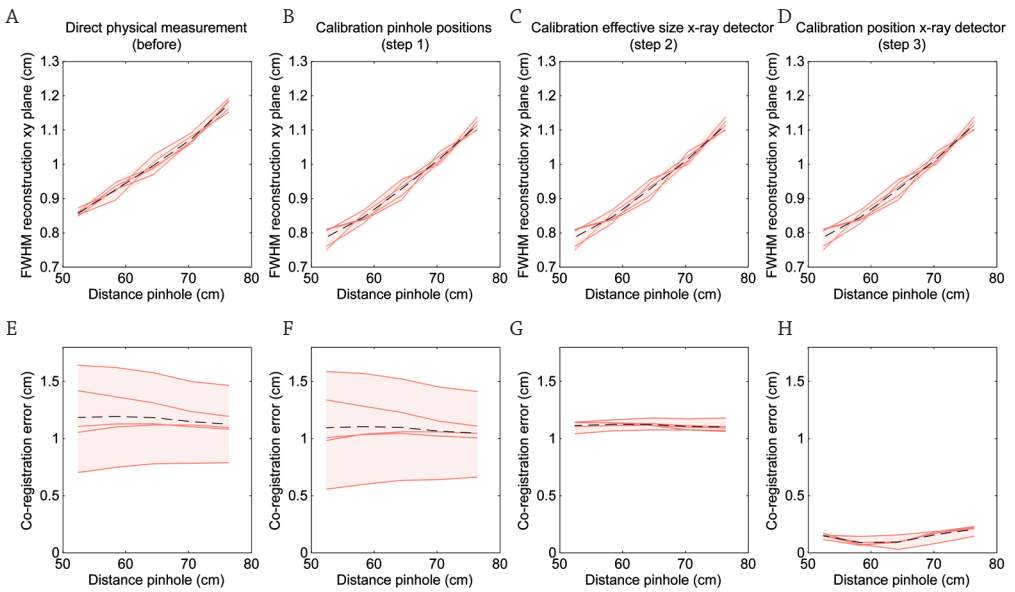


Figure 3.6 Graphical representations of the calibration results showing the resolution of the reconstructed volume in the xy plane as function of distance from the pinholes for the parameter set obtained (A) by direct physical measurement, (B) after calibrating the pinhole positions (step 1), (C) after calibrating the effective size of the x-ray detector (step 2) and (D) after calibrating the position of the x-ray detector (step 3). The co-registration error as function of distance from the pinholes for the parameter set obtained (E) by direct physical measurement, (F) after calibrating the pinhole positions (step 1), (G) after calibrating the effective size of the x-ray detector (step 2) and (H) after calibrating the position of the x-ray detector (step 3). The dashed lines show the mean value of the five point sources. The shaded area denotes the range between the minimum and maximum point source value.

Table 3.2 Parameter values before, during and after calibration. The center of the coordinate system was the center of the scintillation crystal surface. The z axis was perpendicular to the scintillation crystal surface and pointed towards the x-ray detector. Asterisks (*) indicate that the parameter value was unchanged with respect to the previous calibration step.

Parameter	Pinhole nr.	direct physical measurement (before)	calibration pinhole positions (step 1)	calibration effective size x-ray detector (step 2)	calibration position x-ray detector (step 3)
x_{pinhole}	1	-5.40	-5.52	*	*
	2	-5.50	-5.40	*	*
	3	5.40	5.33	*	*
	4	5.50	5.53	*	*
y_{pinhole}	1	-8.90	-8.79	*	*
	2	8.90	8.88	*	*
	3	-9.15	-9.05	*	*
	4	9.15	9.06	*	*
$d_{\text{xray detector}}$		22.86	22.86	21.36	*
$x_{\text{xray detector}}$		0.00	0.00	0.00	-1.09
$y_{\text{xray detector}}$		0.00	0.00	0.00	0.26

Table 3.3 Mean FWHM and co-registration error for the parameter set obtained by direct physical measurement, after resolution calibration, after determining the initial guess of the co-registration calibration and after co-registration calibration. Asterisks (*) indicate that the value was unchanged with respect to the previous calibration step.

	Pinhole distance (cm)	direct physical measurement (before)	calibration pinhole positions (step 1)	calibration effective size x-ray detector (step 2)	calibration position x-ray detector (step 3)
Mean FWHM (cm)	52.4	0.86	0.79	*	*
	58.4	0.93	0.85	*	*
	64.4	1.00	0.93	*	*
	70.4	1.07	1.02	*	*
	76.4	1.18	1.12	*	*
	Mean over distances		1.01	0.94	*
Mean co-registration error (cm)	52.4	1.18	1.09	1.11	0.15
	58.4	1.19	1.11	1.12	0.09
	64.4	1.18	1.10	1.12	0.10
	70.4	1.15	1.06	1.11	0.16
	76.4	1.13	1.05	1.10	0.21
	Mean over distances		1.17	1.08	1.11

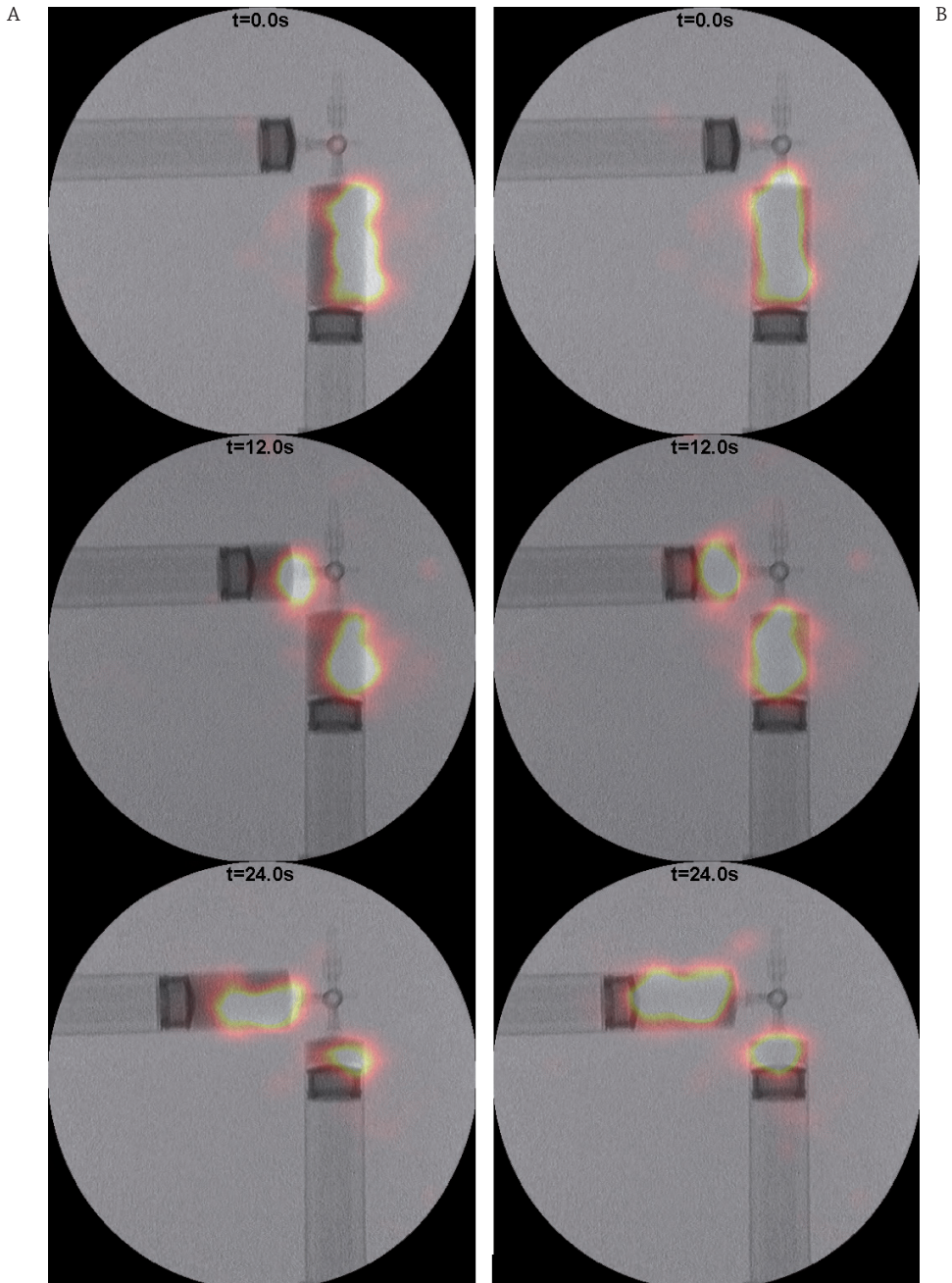


Figure 3.7 Montage of frames from a simultaneous hybrid acquisition of two syringes connected via a three-way-valve filled with 49 MBq of ^{99m}Tc showing fluoroscopic images in grayscale and nuclear images in color overlay. Images were obtained with a parameter set acquired by physical measurement (**A**) and with a parameter set acquired by the calibration method (**B**).

Simultaneous fluoroscopic and nuclear acquisition

The simultaneously acquired dynamic fluoroscopic and nuclear images of the two syringes filled with 49 MBq of ^{99m}Tc are shown in Figure 3.7. With good spatial and temporal overlap of both modalities, a montage of fluoroscopic images is shown in grayscale and nuclear images in color overlay. Visual inspection of the images clearly showed an improvement of the co-registration of fluoroscopic and nuclear images by the calibration method. Differences in resolution of the nuclear images were difficult to assess visually.

Discussion

For hybrid fluoroscopic and nuclear imaging, a correct description of the acquisition geometry is required for accurate reconstruction and co-registration of images. A calibration method was presented that improved the resolution and co-registration of simultaneously acquired hybrid fluoroscopic and nuclear images by estimating the geometric parameter set as compared with a parameter set acquired by direct physical measurement.

The remaining co-registration error after calibration was between 0 and 0.2 cm, and may be caused by not including some geometric parameters in the calibration procedure. For example, the z coordinates of the pinholes, gamma camera, x-ray detector and x-ray tube were not calibrated using the calibration algorithm. However, as observed in experiments not presented in this study, these parameters had minor influence on the resolution and co-registration errors as compared with the parameters estimated with the calibration method. Moreover, the amount of parameters used for calibration is a tradeoff between accuracy and complexity. Model instability and computation time increase with complexity and therefore only the most important parameters were included in the calibration algorithm.

In experiments not presented in this paper, we minimized the co-registration error by varying the x-ray detector position and the effective x-ray detector size using the Levenberg-Marquardt algorithm^{23, 24}. However, this did not significantly reduce the co-registration error as compared with the analytical method. Moreover, Levenberg-Marquardt optimizations with additional parameters including the position of the x-ray tube did not improve co-registration.

The construction of the experimental setup did not fully restrict movement of the c-arm with respect to the gamma camera. Therefore, a calibration of the system parameters was required each time the system was moved. Furthermore, the current experimental setup was only able to perform acquisitions in a single orientation. Future research aims to develop a prototype that can rotate around the patient, the same way conventional c-arms are used.

Corrections were required for the distortion of fluoroscopic images acquired using an image intensifier. Future research will involve the acquisition and development of a prototype with a digital flat panel x-ray detector, capable of performing the first clinical studies. In this way, problems caused by distortion of image intensifiers will be overcome, since these problems are almost non-existent for digital flat panel detectors.

The resolution of the nuclear images depends on the number of iterations used during the reconstruction step. Five MLEM iterations were used during the reconstruction step of the overlap algorithm, which was found optimal for calibration and visualization purposes based on a visual trade-off between resolution and noise. As with all nuclear medicine examinations in clinical

practice, the number of iterations (and/or subsets) is a trade-off between resolution and noise. For some tasks high resolution is required and a large number of iterations is used, whereas images with low noise levels may be favored for other applications. More research needs to be done to determine the application dependent optimal number of MLEM iterations for the fluoroscopic and nuclear imaging *c*-arm. The same holds for the frame rate of nuclear imaging. Guidance of interventional procedures may require high frame rates, whereas diagnostic imaging may require high image quality. The noise level of the acquired images will also depend on the amount of activity that is used, which in turn depends on the isotope and the procedure. Clinical experience will be required to optimize these parameters and is subject of future research.

Limitations of the calibration method include that the co-registration error was only minimized for five positions on the image intensifier. The number of point sources could be increased to acquire calibration data for additional locations. However, an increased number of acquired datasets requires longer computation times and increases complexity.

Over the years, many different optimization algorithms have been developed²⁵. Other optimization algorithms such as the Levenberg-Marquardt method have also been used for calibration of (hybrid) imaging modalities^{7, 11, 26–28}. Using another optimization algorithm than the trust-region reflective method used for the presented calibrations may affect computation times. However, the solution of the optimization is not expected to differ significantly for different optimization algorithms, as long as local convergence is avoided, which was ruled out by using trust-regions.

The accuracy of the physical measurement was limited. For the pinhole positions, measuring tape was used, which resulted in an estimated measurement error of approximately 1 mm. Moreover, the shift of the x-ray detector and x-ray tube with respect to the gamma camera was minimized by visual alignment, which is error-prone. More accurate physical measurements could have been obtained using more advanced measurement equipment, such as laser distance meters. However, the authors believe that geometric parameters estimated by calibration can be obtained with high accuracy, and that achieving the same accuracy by direct measurement would require expensive and advanced equipment. In addition, phantom measurements have the added advantage of allowing for easy evaluation of image quality.

The findings of this study emphasize the importance of correct system calibration for simultaneous fluoroscopic and nuclear imaging. Of course, the specific results are only applicable to the current prototype. The general methodology, however, will also be applicable to future prototypes of the hybrid *c*-arm and may also be of use for calibration of other hybrid modalities²⁹. Therefore, the presented calibration algorithm is a crucial next step towards bringing real-time simultaneous fluoroscopic and nuclear imaging to the intervention room.

Conclusion

A calibration method was presented that improved the resolution and co-registration of simultaneously acquired hybrid fluoroscopic and nuclear images by optimizing the geometric parameter set as compared with a parameter set acquired by direct physical measurement. The improvement of co-registration was verified qualitatively by hybrid imaging of a dynamic phantom.

References

- 1 A. Bockisch, L.S. Freudenberg, D. Schmidt, and T. Kuwert, "Hybrid imaging by SPECT/CT and PET/CT: Proven outcomes in cancer imaging," *Semin. Nucl. Med.* 39, 276–289 (2009).
- 2 P.B. Shyn, "Interventional Positron Emission Tomography/Computed Tomography: State-of-the-Art," *Tech. Vasc. Interv. Radiol.* 16, 182–190 (2013).
- 3 C. Beijst, M. Elschot, M.A. Viergever, and H.W.A.M. de Jong, "Toward Simultaneous Real-Time Fluoroscopic and Nuclear Imaging in the Intervention Room.," *Radiology* 142749 (2015).
- 4 K. Kobayashi et al., "Image-guided biopsy: what the interventional radiologist needs to know about PET/CT," *Radiographics* 32, 1483–1501 (2012).
- 5 S.A. Gulec and Y. Fong, "Yttrium 90 microsphere selective internal radiation treatment of hepatic colorectal metastases.," *Arch. Surg.* 142, 675–682 (2007).
- 6 D. Bequé, J. Nuyts, P. Suetens, and G. Bormans, "Optimization of geometrical calibration in pinhole SPECT.," *IEEE Trans. Med. Imaging* 24, 180–190 (2005).
- 7 G.T. Gullberg, B.M. Tsui, C.R. Crawford, J.G. Ballard, and J.T. Hagius, "Estimation of geometrical parameters and collimator evaluation for cone beam tomography.," *Med. Phys.* 17, 264–72.
- 8 Y. Mao, Z. Yu, and G.L. Zeng, "Geometric calibration and image reconstruction for a segmented slant-hole stationary cardiac SPECT system," *J. Nucl. Med. Technol.* 43, 103–112 (2015).
- 9 Z. El Bitar, R.H. Huesman, R. Boutchko, V. Bekaert, D. Brasse, and G.T. Gullberg, "A detector response function design in pinhole SPECT including geometrical calibration.," *Phys. Med. Biol.* 58, 2395–411 (2013).
- 10 F. Noo, R. Clackdoyle, C. Mennessier, T.A. White, and T.J. Roney, "Analytic method based on identification of ellipse parameters for scanner calibration in cone-beam tomography.," *Phys. Med. Biol.* 45, 3489–508 (2000).
- 11 H. Wang, M.F. Smith, C.D. Stone, and R.J. Jaszczak, "Astigmatic single photon emission computed tomography imaging with a displaced center of rotation.," *Med. Phys.* 25, 1493–501 (1998).
- 12 L.A. Shepp and Y. Vardi, "Maximum likelihood reconstruction for emission tomography," *IEEE Trans. Med. Imaging* 1, 113–122 (1982).
- 13 G. Bal and P.D. Acton, "Analytical derivation of the point spread function for pinhole collimators.," *Phys. Med. Biol.* 51, 4923–4950 (2006).
- 14 C. Beijst, M. Elschot, M.A. Viergever, and H.W.A.M. de Jong, "A parallel-cone collimator for high-energy SPECT," *J. Nucl. Med.* 56, 476–482 (2015).
- 15 S.D. Metzler, J.E. Bowsher, K.L. Greer, and R.J. Jaszczak, "Analytic determination of the pinhole collimator's point-spread function and RMS resolution with penetration," *IEEE Trans. Med. Imaging* 21, 878–887 (2002).
- 16 D.P. Chakraborty, "Image intensifier distortion correction," *Med. Phys.* 14, 249 (1987).
- 17 L.F. Gutiérrez et al., "A practical global distortion correction method for an image intensifier based x-ray fluoroscopy system.," *Med Phys* 35, 997–1007 (2008).
- 18 R.R. Liu, S. Rudin, and D.R. Bednarek, "Super-global distortion correction for a rotational C-arm x-ray image intensifier.," *Med. Phys.* 26, 1802–1810 (1999).
- 19 W.A. Wallace and F. Johnson, "Detection and correction of geometrical distortion in X-ray fluoroscopic images," *J. Biomech.* 14, 123–125 (1981).

- 20 M.A. Branch, T.F. Coleman, and Y. Li, "A subspace, interior, and conjugate gradient method for large-scale bound-constrained minimization problems," *SIAM J. Sci. Comput.* 21, 1–23 (1999).
- 21 R.H. Byrd, R.B. Schnabel, and G.A. Shultz, "Approximate solution of the trust region problem by minimization over two-dimensional subspaces," *Math. Program.* 40, 247–263 (1988).
- 22 R.G. Gould, "A video frame-averaging digital fluoroscopic system.," *Appl. Radiol.* 11, 834–879 (1982).
- 23 K. Levenberg, "A method for the solution of certain non-linear problems in least squares," *Q. J. Appl. Mathematics II*, 164–168 (1944).
- 24 D.W. Marquardt, "An algorithm for least-squares estimation of nonlinear parameters," *J. Soc. Ind. Appl. Math.* 11, 431–441 (1963).
- 25 I. Griva, S.G. Nash, and A. Sofer, *Linear and nonlinear optimization: second edition* (SIAM, 2009).
- 26 F.P. DiFilippo, "Geometric characterization of multi-axis multi-pinhole SPECT.," *Med. Phys.* 35, 181–94 (2008).
- 27 K.J. Kyriakopoulos, P. Yiannakos, V. Kallipolites, and K. Domales, "A geometric calibration methodology for single-head cone-beam X-ray systems," *J. Intell. Robot. Syst.* 24, 151–174 (1999).
- 28 F. van der Have, B. Vastenhouw, M. Rentmeester, and F.J. Beekman, "System calibration and statistical image reconstruction for ultra-high resolution stationary pinhole SPECT.," *IEEE Trans. Med. Imaging* 27, 960–71 (2008).
- 29 N. Navab, S.M. Heining, and J. Traub, "Camera augmented mobile C-arm (CAMC): Calibration, accuracy study, and clinical applications," *IEEE Trans. Med. Imaging* 29, 1412–1423 (2010).



A parallel-cone collimator for high-energy SPECT

Based on:

C. Beijst, M. Elschot, M.A. Viergever, H.W.A.M. de Jong, "A parallel-cone collimator for high-energy SPECT", *The Journal of Nuclear Medicine*, 2015, nr. 3, vol. 56, pp. 476-482

Abstract

Background

In single photon emission computed tomography (SPECT) using high-energy photon emitting isotopes, such as ^{131}I , parallel hole collimators with thick septa are required to limit septal penetration at the cost of sensitivity and resolution. This study investigates a parallel hole collimator with cone shaped holes, which is designed to limit collimator penetration while preserving resolution and sensitivity. The objective is to demonstrate that a single slice prototype of the Parallel Cone (PC) collimator is capable of improving the image quality of high-energy SPECT.

Materials and methods

The image quality of the PC collimator was quantitatively compared to that of clinically used Low-Energy High-Resolution (LEHR; for $^{99\text{m}}\text{Tc}$) and High-Energy General-Purpose (HEGP; for ^{131}I and ^{18}F) parallel hole collimators. First, Monte Carlo simulations of single and double point sources were performed to assess sensitivity and resolution by comparing point spread functions (PSFs). Second, a prototype PC collimator was used in an experimental phantom study to assess and compare contrast recovery coefficients and image noise.

Results

Monte Carlo simulations showed reduced broadening of the PSF due to collimator penetration for the PC collimator as compared with the HEGP collimator (e.g. 0.9 cm vs. 1.4 cm FWHM for ^{131}I). Simulated double point sources placed 2 cm apart were separately detectable for the PC collimator, whereas this was not the case for ^{131}I and ^{18}F at distances from the collimator face ≥ 10 cm for the HEGP collimator. The sensitivity, measured over the simulated profiles as the total amount of counts per decay, was found to be higher for the LEHR and HEGP collimators than for the PC collimator (e.g. 3.1×10^{-5} vs. 2.9×10^{-5} counts per decay for ^{131}I). However, at equal noise level, phantom measurements showed that contrast recovery coefficients were similar for the PC and LEHR collimators for $^{99\text{m}}\text{Tc}$, but that the PC collimator significantly improved the contrast recovery coefficients as compared with the HEGP collimator for ^{131}I and ^{18}F .

Conclusion

High-energy SPECT imaging with a single slice prototype of the proposed PC collimator has shown the potential for significantly improved image quality in comparison with standard parallel hole collimators.

Introduction

Single photon emission computed tomography (SPECT) imaging using isotopes emitting high-energy gamma and/or Bremsstrahlung photons has important applications in oncology and is used for both diagnosis and therapy monitoring. Examples of applications include radioisotope therapy (e.g. ^{131}I , ^{188}Re and ^{67}Ga), monitoring of antibodies (^{111}In) and internal radiation therapy (^{90}Y and ^{166}Ho)¹⁻⁴. SPECT images are used for qualitative as well as quantitative purposes, both requiring high image resolution and low image noise. SPECT imaging of these high-energy photon-emitting isotopes remains a challenge, since broadening of the point spread function (PSF) due to penetration of collimator septa by high-energy photons severely degrades image quality^{5, 6}. Improvement of the quality of high-energy SPECT images is an important field of interest, which may have great impact on planning, follow-up and dosimetry in cancer treatment⁷.

The septal thickness, length and hole size of parallel hole collimators can be optimized for a specific application. The strategy used to optimize parallel hole collimators for high-energy applications, is to increase septal thickness and length to limit septal penetration. Over the years, several high energy collimators have been designed to accommodate photon energies of 200-511 keV, including the SHEAP collimator⁸, the UHE collimator⁹ and the more common high-energy general-purpose (HEGP) collimator. In general, increasing the septal thickness will decrease the amount of penetrated photons, but it will also decrease the system sensitivity. A decrease in sensitivity can be compensated for by increasing the hole size, but this will in turn compromise spatial resolution. In other words, optimizing the design of a parallel hole collimator for high-energy SPECT involves a tradeoff between septal penetration, spatial resolution and sensitivity.

Pinhole collimators are an interesting alternative to parallel hole collimators for high-energy SPECT imaging, since pinholes can be designed in such a way that collimator penetration is limited⁷. Depending on the application and geometry, however, pinhole systems have either limited sensitivity or a small field of view (FOV); the latter is used for example in small organ (e.g.¹⁰) and small animal imaging¹¹. By combining the advantages of parallel hole collimators and high-energy pinhole systems, we aim to design a collimator with high sensitivity, high spatial resolution and limited collimator penetration.

The objective of this work is to present and evaluate a collimator that yields SPECT images for isotopes in the high-energy range that can replace a parallel hole collimator in standard clinical SPECT systems without technical modifications. To this end, we propose a collimator design (the Parallel Cone (PC) collimator) consisting of a repetitive grid of parallel cones, which combines high spatial resolution and low septal penetration with high sensitivity, as compared with a parallel hole collimator. Monte Carlo simulations and phantom experiments were performed with low-energy ($^{99\text{m}}\text{Tc}$) and high-energy (^{131}I and ^{18}F) isotopes, to quantitatively evaluate the performance of the PC collimator in comparison with standard clinical low-energy and high-energy parallel hole collimators. In addition to ^{131}I , $^{99\text{m}}\text{Tc}$ and ^{18}F were included to gain insight into the performance of the PC collimator in situations without and with significant septal penetration.

Materials and Methods

Collimator Design

Figure 4.1 shows a rendering of the PC collimator, consisting of multiple cones with a hexagonally shaped base that can be mounted on a standard gamma camera. The PC collimator was designed in such a way that collimator penetration by high-energy gamma photons is limited. Each cone's top diameter (pinhole diameter) is 4 mm and the cone base diameter (shortest distance across hexagonal base) is 40 mm, its height is 100 mm. The top of each cone is circular, but the bottom is hexagonal so as to have uniform septal thickness at the collimator bottom. The shape can be characterized as a single sided knife-edge pinhole, which allows for small pinhole-to-object distances. If the PC collimator was made from lead in a size typical for most gamma cameras (approximately 500 x 400 mm), the weight of the collimator would be approximately 180 kg. The low-energy and high-energy parallel hole collimator used in this study weigh 20.4 kg and 134.5 kg respectively.

The PC collimator performance was compared to the low-energy and high-energy parallel hole collimators that are commonly used for SPECT imaging in clinical practice. The Siemens BiCore™ low-energy high-resolution (LEHR) collimator (Siemens Healthcare, Erlangen, Germany) has 148000 holes, a hole length of 24.05 mm, hole diameter of 1.11 mm and septal thickness of 0.16 mm. The Siemens BiCore™ HEGP collimator (Siemens Healthcare, Erlangen, Germany) has 8000 holes, a hole length of 59.7 mm, hole diameter of 4.0 mm and septal thickness of 2.0 mm¹².

Prototype Collimator

A prototype with a limited field of view for single slice reconstructions was built, consisting of six cones positioned in a row, with the bases of adjacent cones placed 5 mm apart (Figure 4.2 and Figure 4.3). The collimator was manufactured by lead casting (Nuclear Fields BV, Vortum-Mullem, The Netherlands). The back side of the collimator was mounted on the crystal with 1 mm spacing, so that the distance of the collimator face to the crystal is 10.1 cm.

Monte Carlo Simulations

In order to study the influence of collimator penetration on image quality, Monte Carlo simulations were performed using the Monte Carlo radiation transport code MCNPX 2.5.0¹³. MCNPX standard particle physics settings were used and whenever the energy of a photon fell below 49 keV, it was terminated, simulating 5×10^7 particles. The Monte Carlo simulations took into account the photoelectric effect, coherent and Compton scattering, bremsstrahlung and x-ray production by electrons. No variance reduction techniques were used. The input photon-energy spectra used for the MCNPX simulations were obtained from the Nuclear Data Sheets¹⁴. Photons and particles were tracked and the histories of those travelling through the crystal and their deposited energies were logged. Energy window weighting was performed with a Gaussian filtered energy window to implement the energy resolution. The intrinsic spatial resolution was modeled by applying Gaussian convolution. The gamma camera was simulated including the 9.5 mm NaI(Tl) crystal, aluminium crystal housing, lead camera housing, and photomultiplier tube crown glass acting as backscatter material, as described and validated previously by our group^{6, 15, 16}.

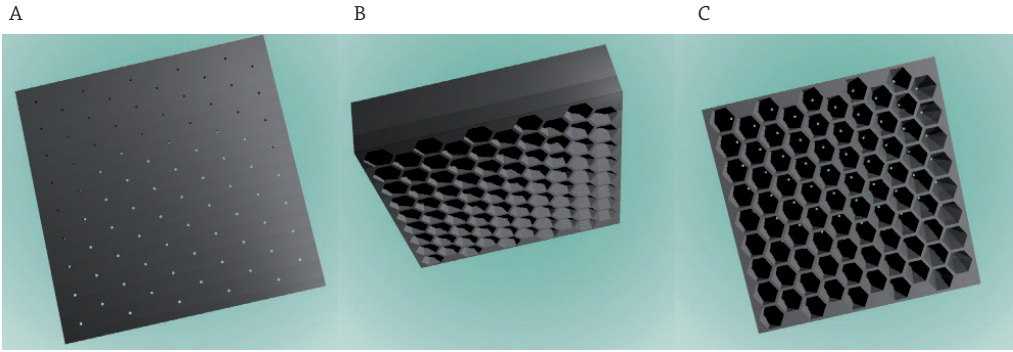


Figure 4.1 Rendering of the PC collimator from different perspectives; (A) from the face of the collimator, (B) the side of the collimator and (C) the back of the collimator.

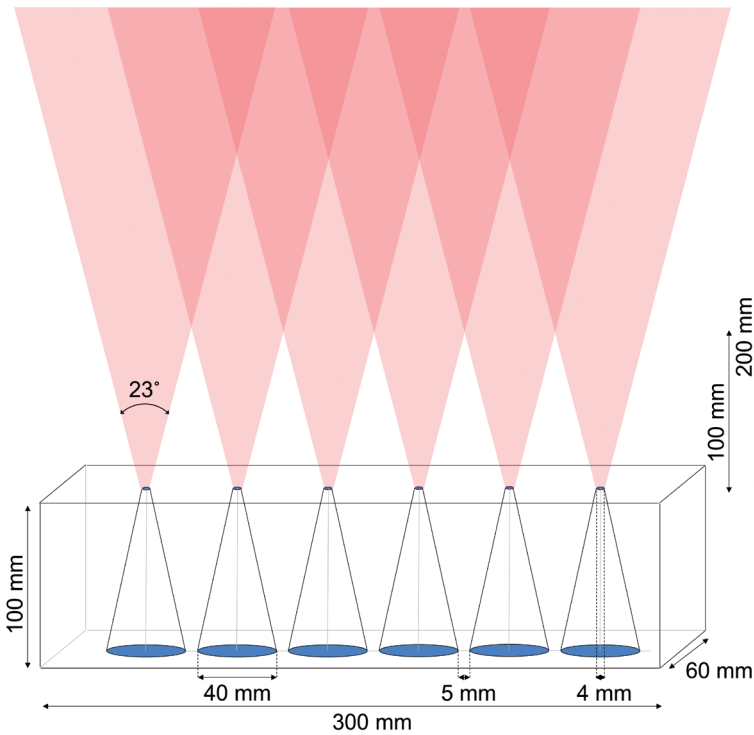


Figure 4.2 Schematic drawing of the PC collimator prototype showing that the fields of view of adjacent cones overlap as the distance from the collimator increases. Darker colors mark the areas that are imaged by multiple cones. The FOVs of adjacent cones overlap at distances greater than 100 mm (two cones) and 200 mm (three cones) from the collimator surface.

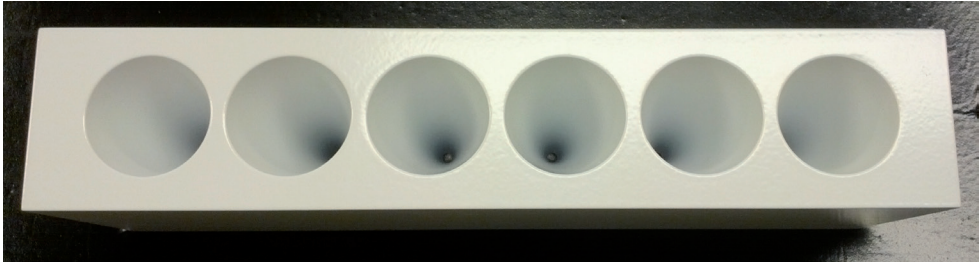


Figure 4.3 Picture of the Parallel Cone collimator prototype.

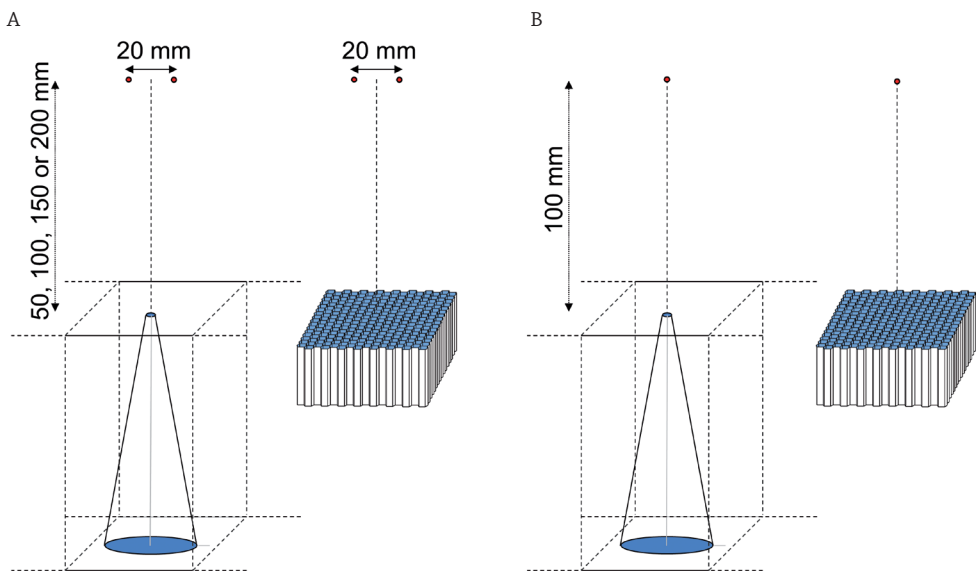


Figure 4.4 Schematic drawing of (A) the double point source Monte Carlo simulation geometry and (B) the single point source Monte Carlo simulation geometry (not drawn to scale).

Table 4.1 Overview of activity concentration and ratios used during phantom experiments.

Isotope	Photon energy (keV)	Activity concentration hot cylinders (MBq/ml)	Activity concentration background (MBq/ml)	Ratio
^{99m}Tc	141	0.88	0.08	11.4
^{131}I	364, 637, 284	0.66	0.06	10.4
^{18}F	511	1.34	0.12	11.5

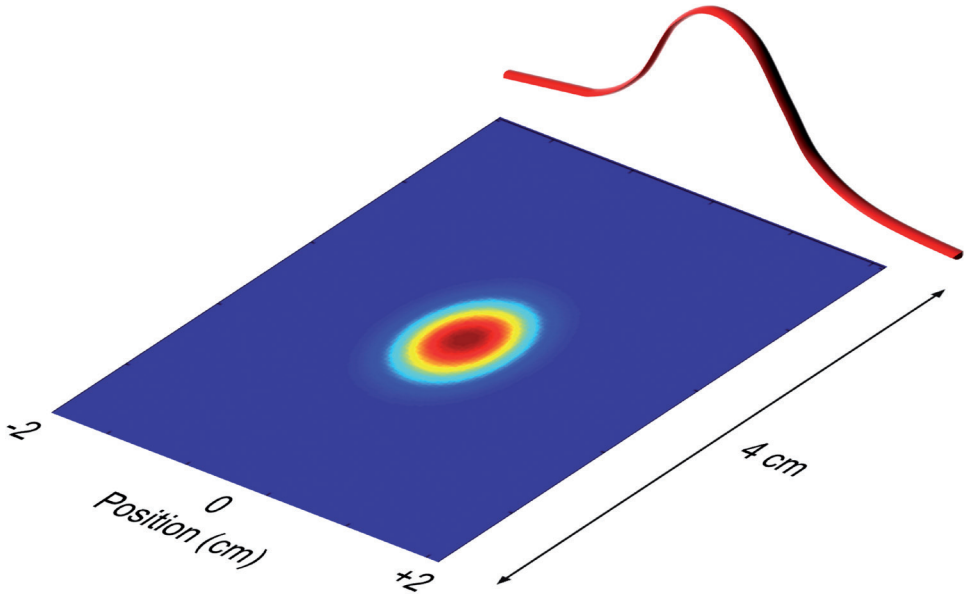


Figure 4.5 Schematic drawing of how one dimensional profiles were created from simulated detector data.

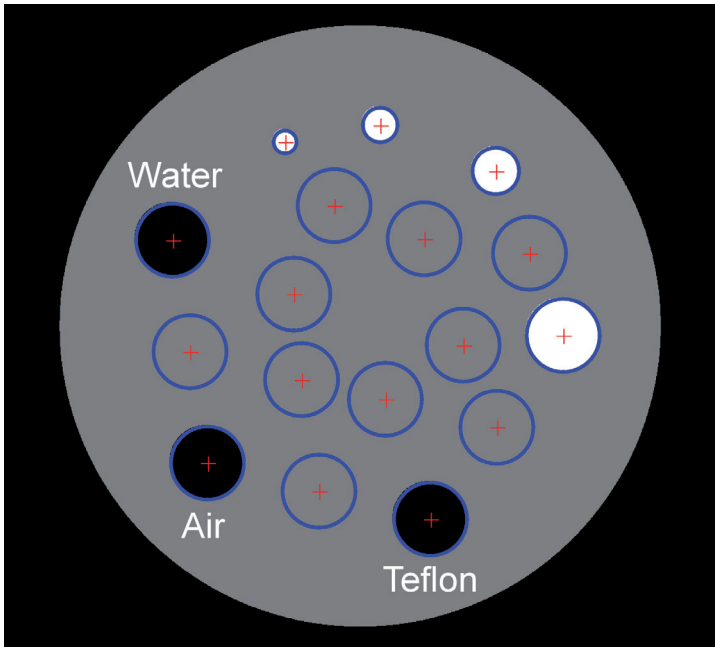


Figure 4.6 Schematic drawing of the phantom with hot cylinders (white), cold cylinders (black) and background ROIs (grey).

^{99m}Tc , ^{131}I and ^{18}F point sources were simulated to compare the prototype PC collimator with the LEHR and HEGP collimators. First, simulations of two point sources in air placed 2 cm apart at 5, 10, 15 and 20 cm distance from the collimator face were performed to study the capability of the collimator to spatially separate the signal of the two sources at varying distance (Figure 4.4A). Second, simulations of a single point source in air placed 10 cm from the collimator face were done to study the point spread function (PSF) broadening (Figure 4.4B). Contributions of primary photons, penetrated photons and other non-primary photons, such as scattered photons, to the total PSF were analyzed separately. One-dimensional profiles were created from the two-dimensional detector data by summation over a width of 4 cm (Figure 4.5). The full width at half maximum (FWHM) and full width at tenth maximum (FWTM) were calculated directly from the acquired profiles. The area under the curve of the measured profiles was determined as a measure of sensitivity, in addition to the maximum value of the profiles.

Phantom Experiments

Phantom

A flangeless Esser phantom (Data Spectrum Corporation, Hillsborough, North Carolina, US) with a lid holding refillable thin-walled cylinders of 8, 12, 16, 25 (x3) mm in diameter and a solid Teflon® cylinder of 25 mm in diameter was used to quantitatively evaluate the image quality of the different collimators. The phantom inner diameter is 204 mm, the inner phantom height is 186 mm and the inner cylinder height is 38.1 mm. Table 4.1 shows the activity concentrations in the hot cylinders and the background of the phantom for the different isotope experiments. As shown in Figure 4.6, the three cold cylinders contained Teflon, air and water. SPECT acquisitions of the same phantom using the PC and HEGP or LEHR collimators were performed successively to compare phantom measurements with the same activity concentration ratio.

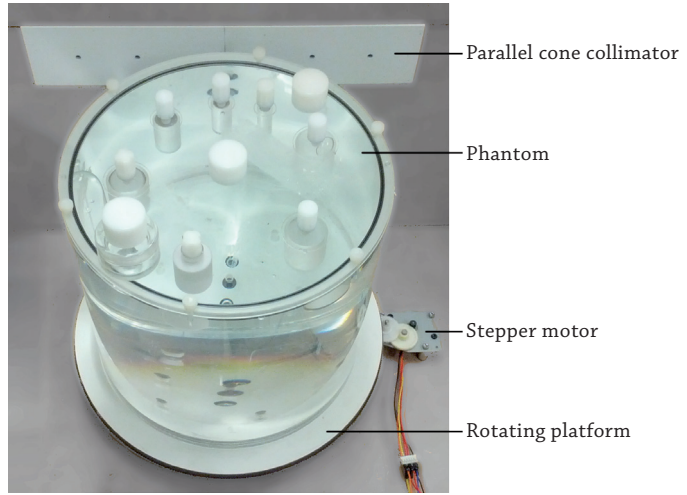
Scanners and Acquisition

A dual-headed Siemens Symbia T16 (Siemens Healthcare, Erlangen, Germany) SPECT/CT system with LEHR (^{99m}Tc) and HEGP (^{131}I and ^{18}F) collimators was used to acquire SPECT images on a 128 x 128 grid with 2.40 x 2.40 mm² pixel size. The PC collimator was mounted on a single-headed ADAC Argus Epic (ADAC Laboratories, Milpitas, CA) gamma camera, acquiring images on a 256 x 256 grid with 2.32 x 2.32mm² pixel size. Both systems use a 9.5 mm NaI(Tl) scintillation crystal. As the construction holding the PC collimator restricted rotation of the gantry, a computer controlled stepper motor was used to accurately rotate the phantom (Figure 4.7). The computer controlling the phantom rotation was also used to start gamma camera acquisitions, in order to synchronize phantom rotation with image acquisition. The energy window width around the photopeak was 15% for ^{99m}Tc , 15% for ^{131}I and 20% for ^{18}F , respectively. 120 projections were acquired over a 360 degrees orbit for all experiments and the distance from the center of rotation to the collimator face was 15 cm. The acquisition time was 30 s per view or proportionally longer to correct for the decay time between consecutive measurements of the same phantom.

Reconstruction

Iterative 2D maximum-likelihood expectation-maximization (MLEM) reconstruction algorithms incorporating attenuation correction and resolution recovery in the forward and backward

Figure 4.7 Picture of the experimental setup showing the PC collimator, phantom, stepper motor controlling the phantom rotation and rotating platform.



projectors were used for image reconstruction¹⁷. Reconstructions of a single (2D) slice instead of a (3D) volume were performed, because the prototype PC collimator consists of only a single row of cones. The measured projections of the Siemens Symbia T16 system were acquired with parallel hole collimators and image reconstruction was performed using an in-house developed 2D MLEM algorithm based on a rotation-based projector/backprojector pair. Convolution with depth-dependent Gaussian PSFs was applied to achieve resolution recovery in both forward and backward projections, including modeling of septal penetration by taking into account the effective septal length. The projections of the ADAC Argus Epic gamma camera were acquired with the PC collimator and image reconstruction was performed using a voxel-driven 2D MLEM algorithm estimating the contribution of voxels covered by the geometry of the cone FOV by modeling the point response geometrically^{18,19}. The finite dimensions of the cone opening as well as collimator penetration were taken into account to incorporate resolution recovery²⁰. To prevent the occurrence of multiplexing artifacts, no backprojection was performed of pixels that contain information from multiple cones i.e. the area between adjacent cones where overlap occurs most likely owing to the limited intrinsic spatial resolution of the anger logic position estimation^{21,22}. Other potential causes for overlap of adjacent pinhole projections are unlikely, because the crystal-collimator geometry does not allow for overlap of primary photons from adjacent cones, the multiplexing is observed even at low energies where collimator penetration is negligible and the Monte Carlo simulations show collimator scatter is negligible. No scatter correction, smoothing or filtering was applied during or after reconstruction to ensure that the reconstruction algorithms for the PC and parallel hole collimators incorporated the same features.

Quantitative Analysis

Figure 4.6 shows a schematic drawing of the phantom overlaid with the positions of the hot cylinder, cold cylinder and background Regions Of Interest (ROIs). To quantitatively evaluate the quality of reconstructed images, several image quality measures were calculated. Wherever

possible, the National Electrical Manufacturers Association (NEMA) 2007 guidelines were adopted²³. Contrast recovery coefficients (CRC) were calculated for each of the hot cylinders using the following equation

$$CRC = \frac{C_H/C_B - 1}{R - 1} \times 100\%$$

where C_H is the mean pixel value in the hot cylinder ROI under consideration, C_B is the mean pixel value in the background ROIs and R is the actual activity concentration ratio between hot cylinders and background. Assuming that R is zero for cold ROIs, cold CRCs are calculated using

$$CRC = \left(1 - \frac{C_C}{C_B}\right) \times 100\%$$

where C_C is the mean pixel value in the cold cylinder ROI. To assess the noise in the reconstructed data, the coefficient of variation (CV) in the pixels contained by the background ROIs shown in Figure 4.6 is calculated using

$$CV = \frac{STDV_B}{C_B} \times 100\%$$

where $STDV_B$ is the standard deviation of the pixel values in all background ROIs. The ROI analysis took into account partial pixels by applying weights to the pixels on the edge of the ROI based on the fraction of their surface that fell within the circular ROI. The position of each ROI was determined with sub-pixel resolution such that the sum of CRCs was maximized. The diameter of the ROIs was taken equal to the inner diameter of cylinders.

The error of the mean value in the hot and background ROIs was determined with 95% confidence intervals and error propagation was used to calculate the uncertainties in the CRCs²⁴. The Standard Equivalency Test was used to determine whether or not measured CRCs were significantly different, described mathematically by

$$|a - b| \leq 2\sqrt{\sigma_a^2 + \sigma_b^2}$$

where a and b are values measured with uncertainties σ_a and σ_b respectively.

Results

Double Point Source Simulations

Figure 4.8 shows the Monte Carlo simulated count distributions of two point sources placed 2 cm apart at several distances from the collimator face. Both the LEHR and PC collimator enable detection of the two ^{99m}Tc sources separately at all simulated distances. However, for ¹³¹I and ¹⁸F point sources at distances greater than 10 cm, a difference can be seen in level of point source separation between the PC and the HEGP collimator. The simulations of the PC collimator show the typical magnification effect expected for the cone geometry; the projected maxima are further apart when the simulated point sources are close to the collimator face, and vice versa. The field of view of adjacent cones is overlapping for distances more than 10 cm from the collimator face

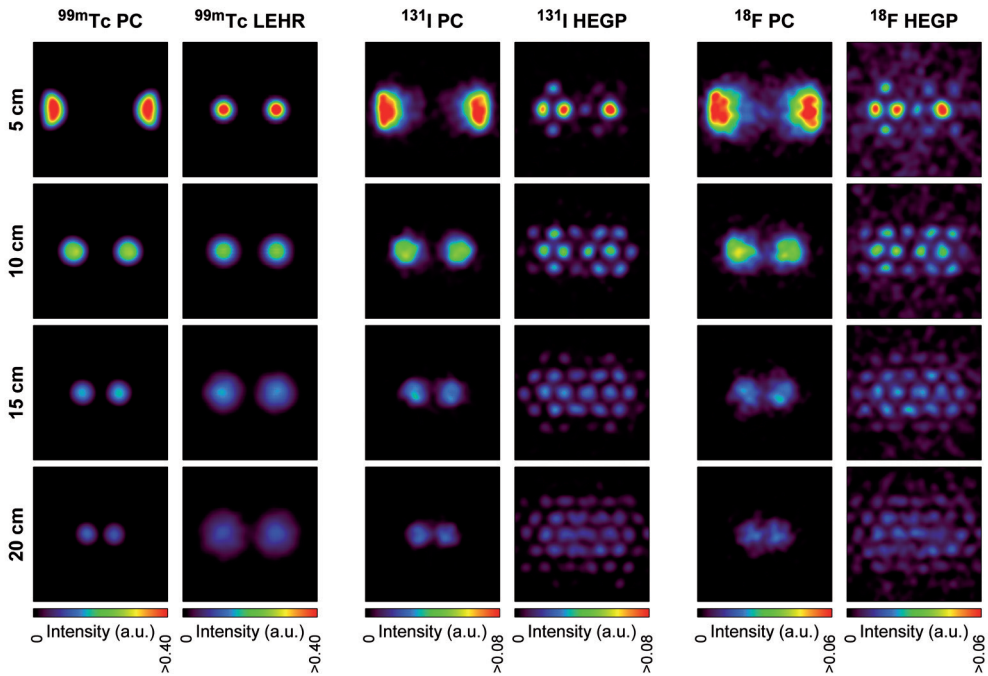


Figure 4.8 Double point source Monte Carlo simulations of the PC collimator, LEHR collimator and HEGP collimator for ^{99m}Tc , ^{131}I and ^{18}F respectively.

and sources can be imaged by multiple cones in this region. Hence, the sensitivity of the collimator is not a continuous function of the distance to the collimator face. The hexagonal pattern of collimator septa can be observed in the simulations of the HEGP collimator, due to the relatively large hole sizes and thick septa.

Single Point Source Simulations

The PSF simulations of ^{131}I and ^{18}F show that PSF broadening is largely caused by septal penetration and that this effect is more clearly present with the HEGP collimator than with the PC collimator (Figure 4.9 and Table 4.2). The width of the FWHM of primary photons as measured by the PC collimator is nearly constant for all isotopes, despite the small variations caused by the energy dependent intrinsic spatial resolution. For ^{131}I and ^{18}F , the FWHM and FWTM of the total PSF measured by the HEGP collimator are higher than the values measured by the PC collimator. Furthermore, the shape of the distribution of penetrated photons is different for the PC and HEGP collimators. For the HEGP collimator, the positions of the septa cause variations in the distribution of penetrated photons. For the PC collimator, two maxima are observed in the distribution of penetrated photons where the edges of the cone are situated. This is where penetration is likely to occur more frequently owing to the limited thickness of the cone edges.

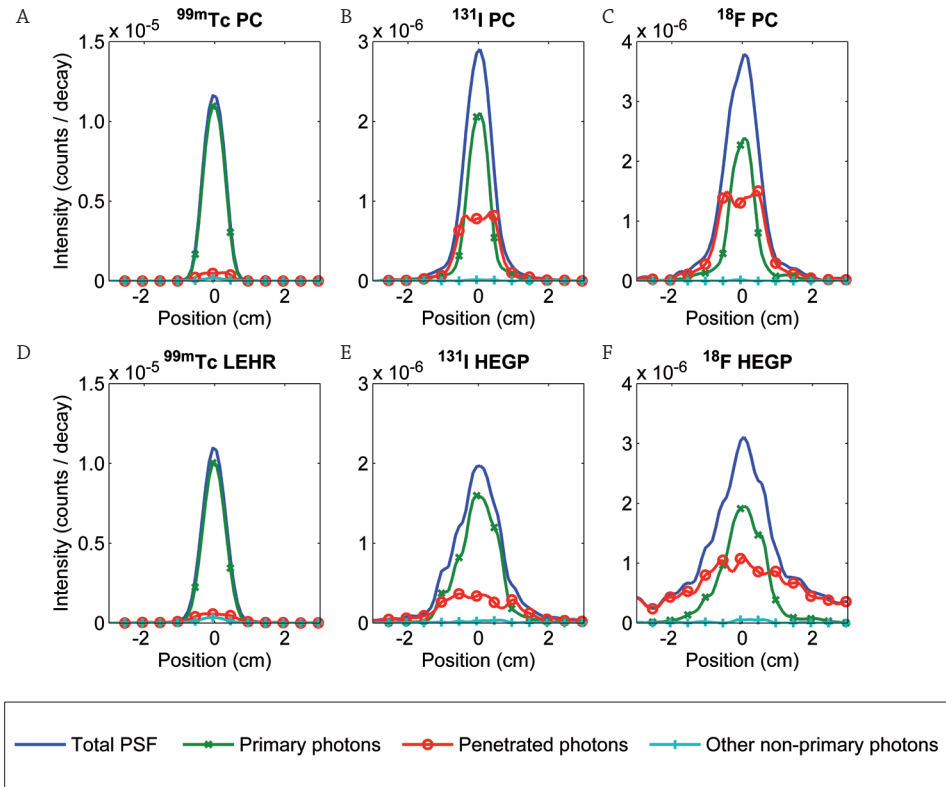


Figure 4.9 Four-cm-wide profiles through the Monte Carlo-simulated projection images of a single point source at 10 cm from the collimator face. Graphs are shown for the Parallel Cone (PC) collimator in (A), (B), and (C), LEHR collimator in (D) and HEGP collimator in (E) and (F) for ^{99m}Tc , ^{131}I and ^{18}F respectively.

While the FWHM of the primary PSF for ^{99m}Tc is equal for both collimators, the FWTM of the total PSF is slightly larger for the LEHR collimator, due to broadening by septum-penetrated and collimator-scattered photons.

The sensitivity, measured over the profiles as the total amount of counts per decay (see also Figure 4.9), was found to be higher for the LEHR and HEGP collimators than for the PC collimator. However, the maximum value of the profiles was higher for the PC collimator (Table 4.3).

Phantom Experiments

2D reconstructed images were created comparing the PC collimator with the LEHR and HEGP collimator (Figure 4.10). To evaluate the image quality quantitatively, contrast recovery coefficients and noise measures are shown as a function of the number of iterations (Figure 4.11). For comparison, images after 37, 43 and 57 iterations for the PC and 49, 122 and 145 iterations for the parallel hole collimators for ^{99m}Tc , ^{131}I and ^{18}F respectively are shown, since these have identical background noise levels (CV) of 15%. These same numbers of iterations were used to

Table 4.2 FWHM and FWTM of the total PSF and of primary photon profiles shown in Figure 4.9.

Isotope	Collimator	FWHM _{tot} (cm)	FWHM _{pri} (cm)	FWTM _{tot} (cm)	FWTM _{pri} (cm)
^{99m} Tc	PC	0.7	0.7	1.2	1.2
	LEHR	0.8	0.7	1.4	1.3
¹³¹ I	PC	0.9	0.7	1.7	1.3
	HEGP	1.4	1.2	2.8	2.3
¹⁸ F	PC	1.1	0.7	2.1	1.4
	HEGP	1.6	1.3	5.5	2.5

Table 4.3 Total and maximum amount of counts per decay of profiles shown in Figure 4.9.

Isotope	Collimator	Profile area (Counts/decay)	Profile maximum (Counts/decay)
^{99m} Tc	PC	8.8x10 ⁻⁵	1.2x10 ⁻⁵
	LEHR	9.1x10 ⁻⁵	1.1x10 ⁻⁵
¹³¹ I	PC	2.9x10 ⁻⁵	2.9x10 ⁻⁶
	HEGP	3.1x10 ⁻⁵	2.0x10 ⁻⁶
¹⁸ F	PC	4.7x10 ⁻⁵	3.8x10 ⁻⁶
	HEGP	6.6x10 ⁻⁵	3.1x10 ⁻⁶

quantitatively compare CRCs between collimators at equal noise levels, as shown in Figure 4.12. Using the Standard Equivalency Test with a 95% confidence interval, the PC hot CRCs were not statistically different from the LEHR CRCs for ^{99m}Tc, whereas PC cold CRCs were significantly lower than those of the LEHR. For ¹³¹I, the hot CRCs of the PC were significantly higher than those of the HEGP. The Teflon cold CRC was significantly higher for the PC collimator, whereas the cold CRC with air was significantly higher for the parallel hole collimator. No significant difference was observed for the cold CRC with water. For ¹⁸F, all CRCs obtained with the PC collimator were significantly higher than those of the parallel hole collimator, except for the cold CRC with air. In general, the CRCs decreased with increasing photon energy.

Discussion

In this study we have presented a PC collimator as an alternative to the customary parallel hole collimators for high-energy photon SPECT imaging.

Monte Carlo simulations and phantom measurements were performed to compare the PC collimator to LEHR and HEGP parallel hole collimators. The Monte Carlo simulations showed that PSF broadening is largely caused by septal penetration of the HEGP collimator and that this effect is reduced by the PC collimator. The phantom experiments demonstrated that the 2D PC collimator can be used for low and high-energy SPECT. It was found that, at equal noise level, the contrast recovery coefficients obtained by the PC collimator were similar to those of the LEHR collimator for ^{99m}Tc, and on average higher than those of the HEGP collimator for ¹³¹I and ¹⁸F.



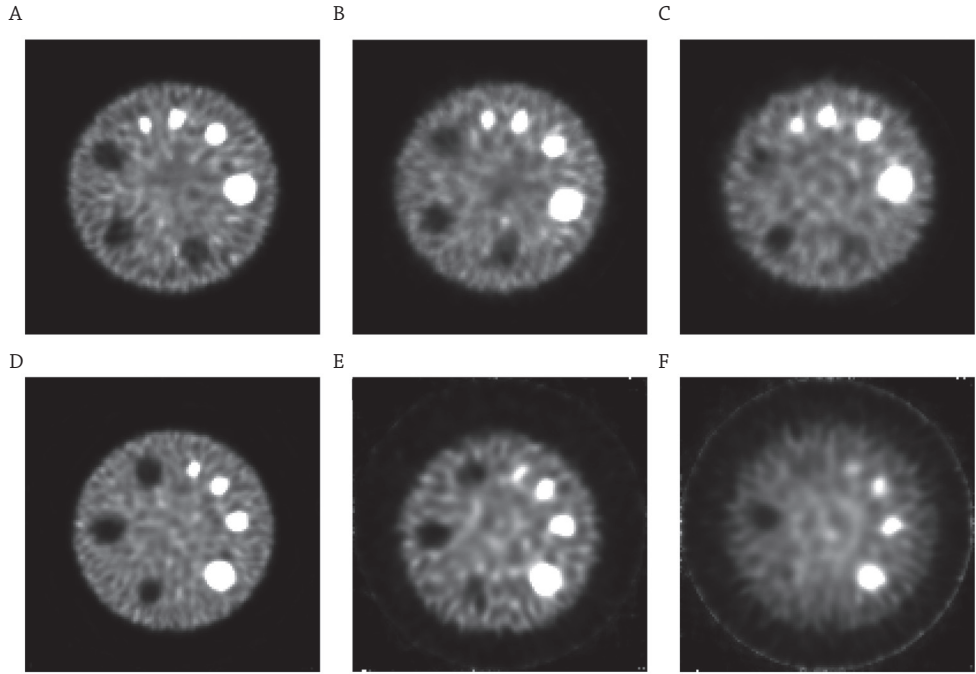


Figure 4.10 Reconstructed data at constant noise levels ($CV=15\%$) for the PC collimator in (A), (B), and (C), LEHR collimator in (D) and HEGP collimator in (E) and (F) for ^{99m}Tc , ^{131}I and ^{18}F respectively. The maximum of the color scale is twice the average background value.

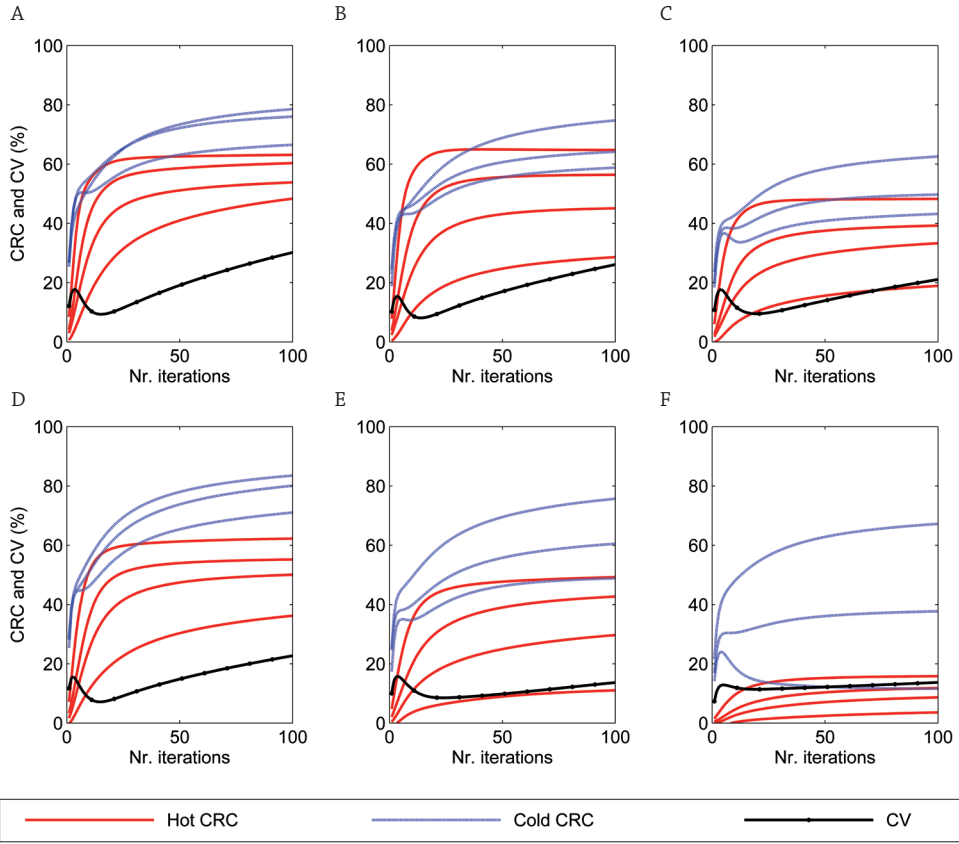


Figure 4.11 The graphs in (A), (B), and (C) for the Parallel Cone (PC) collimator, in (D) for the LEHR collimator and in (E) and (F) for the HEGP collimator show the contrast recovery coefficients and noise as a function of the number of iterations, for ^{99m}Tc, ¹³¹I and ¹⁸F respectively.



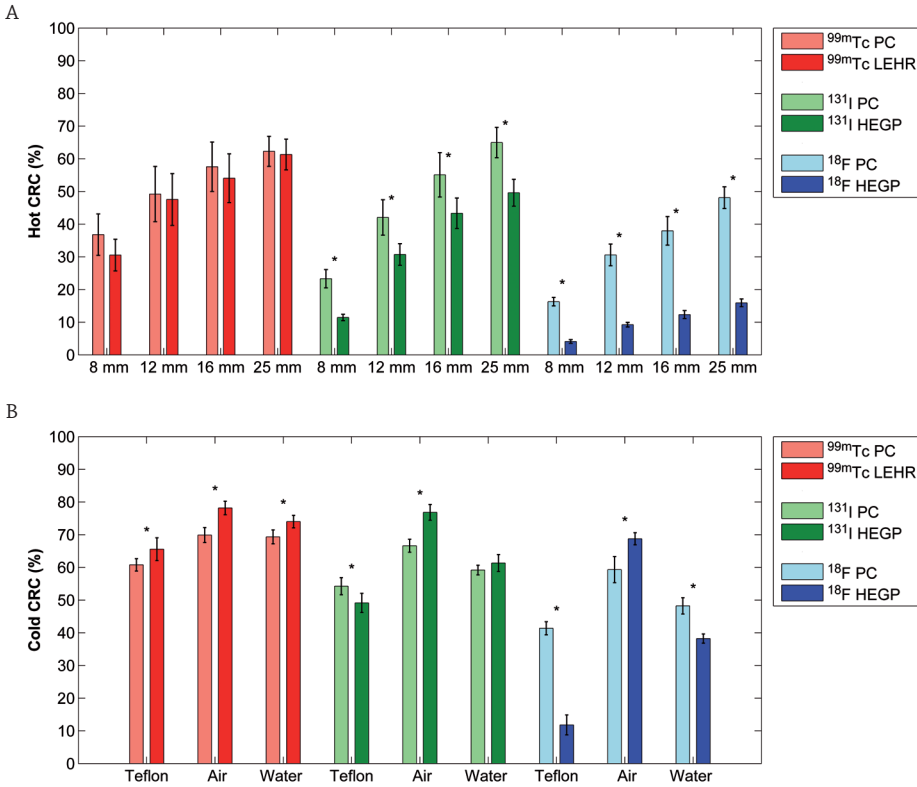


Figure 4.12 The contrast recovery coefficient (CRC) of images at identical noise levels ($CV=15\%$) for the PC and parallel hole collimators shown in (A) of hot cylinders and in (B) of cold cylinders for ^{99m}Tc , ^{131}I and ^{18}F . Asterisks (*) indicate significantly different CRCs.

The total amount of counts over the profiles was calculated for single point source simulations as a measure of sensitivity. In this study, a distance of 10 cm was used, so that the magnification factor is approximately 1, for both the PC collimator and the parallel hole collimators. Because the sensitivity is highest for the PC collimator when the point source is positioned directly in front of the cone, this might not be a fair comparison with the parallel hole collimators. On the other hand, the measurements do not take into account that a point source is possibly imaged by multiple cones. In general, it is difficult to define a single metric to assess the impact of the sensitivity on image quality. Therefore, the CRCs and CV in reconstructed images were studied.

Owing to the design of the collimator, the acquisition of a single planar projection does not directly yield a useful image. Sampling of the entire field of view is achieved by performing tomography and useful images are generated after reconstruction. The sensitivity of the collimator depends on by how many cones the source is 'seen', and is therefore not a continuous function of the distance to the collimator face. The use of multiple cones ensures that the sensitivity does not decrease as rapidly with distance from the collimator as with single pinhole collimators.

The error bars presented in Figure 4.12 are based on the noise level of the image, which means that they are a measure of (pixel) precision, but not of accuracy. Therefore, the error bars only represent random errors and do not include possible systematic errors. For example, measurement errors in the activity concentration might have yielded a systematic over/underestimation of the background-to-cylinder ratio. However, such a systematic misestimation would have affected CRC quantification of the parallel hole and PC collimator proportionally, since measurements of an isotope with different collimators were performed consecutively using the same phantom. Consequently, the validity of relative image quality differences that were observed between the collimator types is not compromised by neglecting these potential systematic errors. However, such errors might explain the better 25 mm cylinder CRC for ^{131}I as compared with $^{99\text{m}}\text{Tc}$, although the observed difference is not significant.

The prototype PC collimator consists of a single row of cones to simplify production and to keep costs low. Consequently, SPECT data could only be reconstructed to 2D slices (instead of 3D volumes) for the PC collimator. The SPECT data for the parallel hole collimators were also reconstructed in 2D, to ensure that collimator differences were studied rather than differences in the reconstruction algorithm.

To prevent the occurrence of multiplexing artifacts, two pixels on either side of the cone were not used for backprojection, i.e. 4 out of approximately 20 pixels per cone. For future research, it should be taken into account that the relative amount of masked pixels is larger in 2D projections than in 1D projections. However, the amount of masked pixels can possibly be reduced, since no fundamental need for this masking exists, by optimizing the collimator design, for example by optimizing the thickness of septa at the bottom of the cones.

This study shows that the image quality of the PC collimator decreases as the photon energy increases, but that this effect is not as severe as observed for the parallel hole collimator. This indicates that the PC collimator could be used for a variety of radioisotopes and photon energies. Using a single collimator for multiple purposes has many benefits in clinical practice, because changing collimators between exams is time consuming and requires large and heavy collimator carts. A study comparing acquisitions from full-FOV collimators with full 3D acquisitions and algorithms may give conclusive answers as to whether the PC collimator can improve image quality in clinical practice for high-energy applications.

Conclusion

A Parallel Cone collimator for high-energy SPECT imaging has been designed and evaluated. Monte Carlo simulations show less broadening of the PSF due to collimator penetration for the proposed collimator than for a high-energy parallel hole collimator. Additionally, phantom measurements with a single slice prototype of the proposed PC collimator have shown the potential for significantly improved quality of high-energy SPECT images in comparison with standard parallel hole collimators.

References

- 1 A.M. Avram, "Radioiodine scintigraphy with SPECT/CT: An important diagnostic tool for thyroid cancer staging and risk stratification," *J. Nucl. Med. Technol.* 42, 170–180 (2014).
- 2 Y.K. Dewaraja et al., "MIRD pamphlet no. 23: Quantitative SPECT for patient-specific 3-dimensional dosimetry in internal radionuclide therapy," *J. Nucl. Med.* 53, 1310–1325 (2012).
- 3 S. Shcherbinin, J. Grimes, A. Bator, J.B. Cwikla, and A. Celler, "Three-dimensional personalized dosimetry for (188)Re liver selective internal radiation therapy based on quantitative post-treatment SPECT studies.," *Phys. Med. Biol.* 59, 119–134 (2013).
- 4 M.A.D. Vente et al., "Yttrium-90 microsphere radioembolization for the treatment of liver malignancies: A structured meta-analysis," *Eur. Radiol.* 19, 951–959 (2009).
- 5 Y.K. Dewaraja, M. Ljungberg, and K.F. Koral, "Characterization of scatter and penetration using Monte Carlo simulation in 131I imaging.," *J. Nucl. Med.* 41, 123–130 (2000).
- 6 M. Elschoot, J.F.W. Nijssen, A.J. Dam, and H.W.A.M. de Jong, "Quantitative evaluation of scintillation camera imaging characteristics of isotopes used in liver radioembolization," *PLoS One* 6, (2011).
- 7 S. Walrand, M. Hesse, G. Demonceau, S. Pauwels, and F. Jamar, "Yttrium-90-labeled microsphere tracking during liver selective internal radiotherapy by bremsstrahlung pinhole SPECT: feasibility study and evaluation in an abdominal phantom," *EJNMMI Res.* 1, 32 (2011).
- 8 A. Van Lingen et al., "Performance characteristics of a 511 keV collimator for imaging positron emitters with a standard gamma-camera," *Eur. J. Nucl. Med.* 19, 315–321 (1992).
- 9 Y.K. Dewaraja, M. Ljungberg, and K.F. Koral, "Accuracy of 131I tumor quantification in radioimmunotherapy using SPECT imaging with an ultra-high-energy collimator: Monte Carlo study.," *J. Nucl. Med.* 41, 1760–1767 (2000).
- 10 P.M. Wanet, A. Sand, and J. Abramovici, "Physical and clinical evaluation of high-resolution thyroid pinhole tomography.," *J. Nucl. Med.* 37, 2017–2020 (1996).
- 11 J. Nuyts, K. Vunckx, M. Defrise, and C. Vanhove, "Small animal imaging with multi-pinhole SPECT," *Methods* 48, 83–91 (2009).
- 12 Symbia™ TruePoint SPECT/CT System Specifications, (2005).
- 13 J.S. Hendricks et al., "MCNPX Extensions version 2.5.0," (2005).
- 14 Y. Khazov, I. Mitropolsky, and A. Rodionov, "Nuclear Data Sheets for A = 131," *Nucl. Data Sheets* 107, 2715–2930 (2006).
- 15 M. Elschoot, M.G.E.H. Lam, M.A.A.J. van den Bosch, M.A. Viergever, and H.W.A.M. de Jong, "Quantitative Monte Carlo-based 90Y SPECT reconstruction.," *J. Nucl. Med.* 54, 1557–63 (2013).
- 16 M. Elschoot et al., "Quantitative Monte Carlo-based holmium-166 SPECT reconstruction," *Med. Phys.* 40, 112502–112512 (2013).
- 17 L.A. Shepp and Y. Vardi, "Maximum likelihood reconstruction for emission tomography," *IEEE Trans. Med. Imaging* 1, 113–122 (1982).
- 18 G. Bal and P.D. Acton, "Analytical derivation of the point spread function for pinhole collimators.," *Phys. Med. Biol.* 51, 4923–4950 (2006).
- 19 S.D. Metzler, J.E. Bowsher, K.L. Greer, and R.J. Jaszczak, "Analytic determination of the pinhole collimator's point-spread function and RMS resolution with penetration," *IEEE Trans. Med. Imaging* 21, 878–887 (2002).

- 20 C. Vanhove, A. Andreyev, M. Defrise, J. Nuyts, and A. Bossuyt, "Resolution recovery in pinhole SPECT based on multi-ray projections: a phantom study," *Eur. J. Nucl. Med. Mol. Imaging* 34, 170–180 (2007).
- 21 B.J. Min et al., "Unmatched projector/backprojector pair for demultiplexing in multipinhole emission computed tomography," *Opt. Eng.* 49, 127004 (2010).
- 22 K. Vunckx, P. Suetens, and J. Nuyts, "Effect of overlapping projections on reconstruction image quality in multipinhole SPECT," *IEEE Trans. Med. Imaging* 27, 972–983 (2008).
- 23 NEMA, NEMA standards publication NU 2-2007 Performance measurements of positron emission tomographs.
- 24 J.R. Taylor, *An Introduction To Error Analysis: The Study Of Uncertainties In Physical Measurements* (University Science Books, Sausalito, CA, 1997).





Quantitative comparison of ^{124}I PET/CT and ^{131}I SPECT/CT detectability

Based on:

C. Beijst, J.W. Kist, M. Elschot, M.A. Viergever, O.S. Hoekstra, B. de Keizer, H.W.A.M. de Jong,
“Quantitative comparison of ^{124}I PET/CT and ^{131}I SPECT/CT detectability “, *The Journal of Nuclear
Medicine*, 2016, nr. 1, vol. 57, pp. 103-108

Abstract

Background

Radioiodine therapy with ^{131}I is used for treatment of suspected recurrence of differentiated thyroid carcinoma. Pre-therapy ^{124}I PET/CT with a low activity (~1% of ^{131}I activity) can be performed to determine whether uptake of ^{131}I , and thereby the desired therapeutic effect, may be expected. However, false negative ^{124}I PET/CTs as compared with the post-therapy ^{131}I SPECT/CTs have been reported by several groups. The purpose of this study was to investigate whether the reported discrepancies may be ascribed to a difference in detectability of lesions on ^{124}I PET/CT and ^{131}I SPECT/CT, and hence, to determine whether the administered activity of ^{124}I is sufficient to achieve equal detectability.

Methods

Phantom measurements were performed using the NEMA-2007 image quality phantom. As a measure of detectability the contrast-to-noise ratio (CNR) was calculated. The ^{124}I activity concentration was expressed as a percentage of the ^{131}I activity concentration required to achieve the same CNR. This metric was defined as the detectability equivalence percentage (DEP).

Results

Lower DEPs were obtained for smaller spheres, so that a relatively low ^{124}I activity concentration is sufficient to achieve a similar detectability of lesions with ^{124}I PET/CT as with ^{131}I SPECT/CT. The DEP was 1.5, 1.9, 1.9, 4.4, 9.0 and 16.2% for the spheres with a diameter of 10, 13, 17, 18, 25 and 37 mm respectively, for attenuation and scatter corrected SPECT versus point spread function (PSF) modeled and time-of-flight (TOF) PET. For no-PSF no-TOF PET, the DEP was 3.6, 2.1, 3.5, 7.8, 15.1 and 23.3%.

Conclusion

A relatively low activity of 74 MBq ^{124}I (~1% of ^{131}I activity) is sufficient to achieve similar detectability of lesions on ^{124}I PSF TOF PET/CT and ^{131}I SPECT/CT for small spheres ($\leq 10\text{mm}$), since the reported DEPs are close to 1%. False negative ^{124}I PET/CTs as compared with the post-therapy ^{131}I SPECT/CTs may be ascribed to differences in detectability for large lesions ($>10\text{mm}$) and for no-PSF no-TOF PET, since DEPs are larger than 1%. Based on DEPs of 3.5% for lesion diameters up to 17mm on no-PSF no-TOF PET, activities as high as 170 MBq of ^{124}I may be warranted to obtain equal detectability.

Introduction

Radioiodine therapy with ^{131}I is used for the primary treatment of differentiated thyroid carcinoma by ablating remnant thyroid tissue and potential residual tumor tissue after thyroid resection. Treatment with 5.5-7.4 GBq of ^{131}I is indicated if a patient is suspected of metastases¹. The administered activity of ^{131}I is generally empiric and non-patient-specific, since the uptake and hence the therapeutic effectiveness of radioiodine in metastatic lesions is usually not known beforehand. Post-therapy ^{131}I SPECT/CT and/or whole body scintigraphy is routinely performed to assess tumor uptake. Up to 50% of empirically treated patients show no uptake on the post-therapy imaging². To predict whether uptake of radioiodine, and hence a desired therapeutic effect, may be expected, pre-therapy imaging with a low activity is performed.

Several pre-therapy imaging strategies have been suggested to optimize patient-specific treatment activity and to prevent unnecessary ^{131}I therapies. ^{131}I whole-body scintigraphy with a low non-therapeutic activity of ^{131}I (half-life 8 days) can be used for pre-therapy imaging³. However, diagnostic low activity scintigraphy with ^{131}I does not adequately predict the results of post-therapeutic high activity ^{131}I scintigraphy⁴. Moreover, septal penetration by the high-energy (364 keV and 637 keV) gamma photons negatively affects the image quality of ^{131}I SPECT and scintigraphy, which makes ^{131}I less suitable for diagnostic purposes. The medium energy (159 keV) gamma emitter ^{123}I has also been suggested for pre-therapy imaging and studies investigating the potential of ^{123}I yielded good results (e.g. ⁵). However, due to the short half-life of ^{123}I (13.2 h) a large fraction of the administered activity has already decayed before the maximum uptake is achieved and imaging is performed.

Alternatively, ^{124}I with a half-life of 4.2 days has been proposed for pre-therapy imaging and assessment of treatment response. Several groups have reported promising results using ^{124}I as a diagnostic agent^{6,7}. ^{124}I is a positron emitter and can be imaged with PET, with superior resolution, sensitivity and quantitation as compared with scintigraphy or SPECT used for ^{131}I . Relatively low activities of 20 – 74 MBq are used for diagnostic ^{124}I PET imaging⁸⁻¹³.

Unfortunately, clinical experiences have shown that ^{124}I PET/CT does not always predict uptake of ^{131}I reliably, and discrepancies between post-therapy ^{131}I SPECT/CT and pre-therapy ^{124}I PET/CT have been reported by several groups⁸⁻¹³. More specifically, in some cases no uptake was found on ^{124}I PET/CT images, whereas uptake was found on ^{131}I SPECT/CT images. An example from a study we performed (unpublished data) is shown in Figure 5.1¹⁴. These false negative ^{124}I PET/CTs as compared with ^{131}I SPECT/CTs may be ascribed to a difference in detectability of lesions on ^{124}I PET/CT and ^{131}I SPECT/CT.

The purpose of this study was to investigate whether the reported discrepancies may be ascribed to a difference in detectability of lesions on ^{124}I PET/CT and ^{131}I SPECT/CT, and hence, to determine whether the administered activity of ^{124}I is sufficient to achieve equal detectability. This was done by establishing the activity concentration of ^{124}I expressed as a percentage of the ^{131}I activity concentration at which the contrast-to-noise ratio was equal for both modalities.

Materials and Methods

Phantom

To compare the detectability of lesions on ^{131}I SPECT/CT and ^{124}I PET/CT images, acquisitions of the IEC NEMA 2007 phantom (PTW, Freiburg, Germany) were performed with varying activity concentrations. The phantom is torso-shaped and has a lid holding refillable thin-walled spheres of 10, 13, 17, 22, 28 and 37 mm in diameter. Separate phantoms were used for ^{124}I and ^{131}I experiments. The phantoms were filled only once and different activity concentrations were obtained by leaving the activity to decay. This approach decreases measurement errors in comparison with refilling the phantom. Two phantoms were used for detectability analysis; one with activity in the background compartment and one without.

Clinically, large variations may occur in lesion to background ratios. Rubello et al. have performed measurements of the lesion-to-background ratio with a gamma probe during radio-guided surgery, and they obtained a mean lesion-to-background ratio of 11.4¹⁵. Therefore, we used two phantoms with different background concentrations to capture both extremities; no background (1:0) and a high background concentration (10:1). The activity concentration in the spheres ranged from 1.8×10^4 Bq/ml to 4.6 Bq/ml for ^{124}I and from 9.1×10^5 Bq/ml to 3.9×10^2 Bq/ml for ^{131}I . The initial activity concentrations are shown in Table 5.1. The activity concentration in the phantoms was chosen such that it could be used to effectively compare the detectability of lesions in the range around the expected minimum detectable activity (MDA). In total, 45 ^{124}I PET acquisitions were acquired over a period of 50 days. Similarly, 42 ^{131}I SPECT acquisitions were performed over a period of 90 days.

Scanners and acquisition

A Siemens Biograph mCT Time-of-Flight (TOF) PET/CT scanner (Siemens Healthcare, Erlangen, Germany) with TrueV (axial field of view 21.6 cm) was used to acquire PET data. ^{124}I images were acquired using a 435-650 keV energy window in 4 minutes per bed position, in accordance with the clinical protocol¹⁴. Three bed positions were used to ensure that the sensitivity was uniform along the entire length of the phantom in the axial direction.

A dual-headed Siemens Symbia T16 (Siemens Healthcare, Erlangen, Germany) SPECT/CT system was used to acquire SPECT images. The Siemens BiCore™ high-energy (HE) (Siemens Healthcare, Erlangen, Germany) collimator that was used has 8000 holes, a hole length of 59.7 mm, hole diameter of 4.0 mm and septal thickness of 2.0 mm. For all ^{131}I acquisitions, 128 projections were acquired on a 128 x 128 grid with a 4.8×4.8 mm² pixel size. In accordance with the clinical protocol, a 25 s acquisition time per view was used, resulting in a total acquisition time of 26 minutes.

Reconstruction

PET images were reconstructed to create 200 x 200 x 316 voxel images with $4.07 \times 4.07 \times 1.50$ mm³ voxel size. The reconstruction incorporated a ^{124}I prompt gamma correction¹⁶ and a randoms correction by adding the Gaussian-filtered randoms-sinogram to the forward projection during the iterative reconstruction¹⁷. Two reconstruction methods were used to obtain PET images.

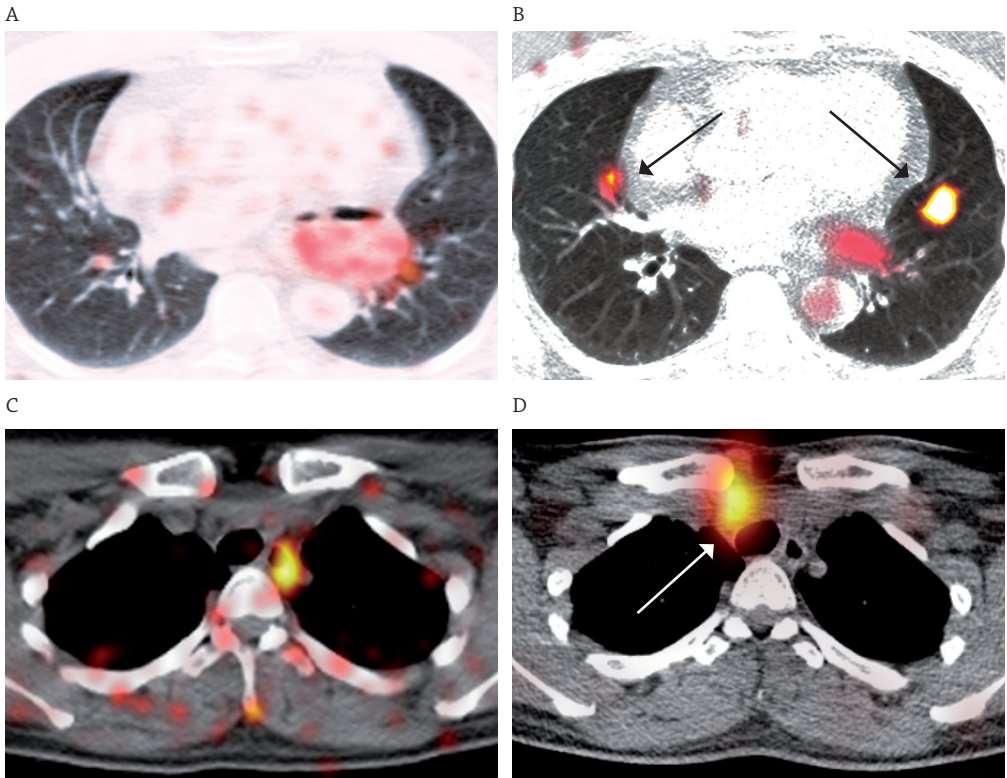


Figure 5.1 Examples of cases from the THYROPET trial¹⁴ where false negative ¹²⁴I PET/CTs as compared with the ¹³¹I SPECT/CT were obtained. ¹²⁴I PET/CT (A and C) acquired 24 hours after oral administration of 74 MBq ¹²⁴I and ¹³¹I SPECT/CT (B and D) acquired 7 days after oral administration of 7400 MBq ¹³¹I, for the first and second patient respectively. The PET/CT scans were acquired using a Philips Gemini in 2 minutes per bed position and a LOR-RAMLA reconstruction without time-of-flight correction (no-PSF no-TOF). The SPECT/CT scans were acquired on a Siemens Symbia T2 in a total scan time of 21 minutes using a Flash3D attenuation corrected reconstruction method (no-SC 6i8s). The arrows indicate the metastatic lesions.

Table 5.1 Initial activity concentrations of the phantoms at time of the first experiment.

Isotope	Initial activity concentration spheres (Bq/ml)	Initial activity concentration background (Bq/ml)	Ratio
¹²⁴ I	1.8×10^4	0	-
¹²⁴ I	1.8×10^4	1.8×10^3	10
¹³¹ I	9.1×10^5	0	-
¹³¹ I	9.1×10^5	9.0×10^4	10

The first method was an ordered subset expectation maximization 3D reconstruction method incorporating time of flight (TOF) information (TrueX) with point spread function (PSF) model based resolution recovery and CT based attenuation and scatter correction, using 4 iterations and 21 subsets in accordance with the clinical protocol. A Gaussian post-reconstruction filter was applied with a full width at half maximum of 5 mm. This method will be referred to as the PSF TOF method.

The second method was an ordered subset expectation maximization 3D reconstruction method with attenuation correction, scatter correction, no TOF modeling and no PSF model based resolution recovery. As advised by the vendor, 4 iterations and 24 subsets were used and a Gaussian post-reconstruction filter was applied with a full width at half maximum of 5 mm. This reconstruction method will be referred to as the *no-PSF no-TOF* method.

SPECT images were reconstructed to create 128 x 128 x 80 voxel images with 4.8 x 4.8 x 4.8 mm³ voxel size. The Siemens Flash 3D reconstruction algorithm was used, incorporating attenuation correction and resolution recovery using distance dependent PSFs. Three reconstruction methods were used to obtain SPECT images. The first method used 6 iterations with 8 subsets and triple-energy-window scatter correction (*SC 6i8s*), the second method used 6 iterations with 8 subsets and did not incorporate scatter correction (*no-SC 6i8s*) and the third method used 30 iterations with 8 subsets and triple-energy-window scatter correction (*SC 30i8s*). Reconstructions with 6 iterations and 8 subsets were performed to allow comparison with the clinical trial running at our hospital¹⁴, whereas reconstructions with 30 iterations and 8 subsets were included for increased contrast recovery at the cost of increased image noise^{18,19}.

Quantitative analysis

Detectability Equivalence Percentage

As a measure of detectability, we calculated the contrast-to-noise ratio (CNR) for each sphere using

$$CNR = \frac{C_H - C_B}{\sigma_B}$$

where C_H is the mean voxel value in the sphere volume of interest (VOI), C_B is the mean voxel value in the background VOI and σ_B is the standard deviation in the background VOI.

Three-dimensional VOI masks were created based on the sphere coordinates determined from the co-registered CT. The position of the spheres in the CT image was determined automatically using a Hough-transform based circle detection method²⁰. The background VOI was defined as the entire phantom minus the sphere VOIs. To eliminate the influence of partial volume effects on the background measurement, a 2 cm margin around the spheres and the phantom edges was subtracted from the background VOI by means of binary erosion.

To assess the difference in detectability of spheres on ¹²⁴I PET/CT and ¹³¹I SPECT/CT, the ¹²⁴I activity concentration was expressed as a percentage of the ¹³¹I activity concentration required to achieve the same CNR. This metric was defined as the *detectability equivalence percentage (DEP)*. For example, a DEP of 1% indicates that the same CNR is obtained on the ¹²⁴I PET/CT image as on the ¹³¹I SPECT/CT image if the ¹²⁴I activity concentration is 1% of the ¹³¹I activity concentration. The DEP was determined by calculating the average ratio of the CNR curves (CNR versus activity concentration) for the two isotopes, and multiplied by 100 to obtain a percentage. This was done

for each sphere size and sphere-to-background ratio. To reduce the influence of noise on the calculated DEPs, regression analysis of the curves was performed. Cubic spline fits of the activity concentration as a function of the sphere CNR were performed and plotted in the log-log domain, because the range of the curves was several orders of magnitude. The mean ratios were calculated over the largest possible interval where CNR data was acquired for both isotopes and where CNR values were greater than 1. For the phantom without activity in the background compartment, the CNR values, where the mean pixel value of the background VOI was smaller than one, were not used for the regression analysis.

Minimum Detectable Activity

False negative ^{124}I PET/CTs as compared with the ^{131}I SPECT/CTs occur when the ^{124}I activity concentration is below minimum detectable activity (MDA) and ^{131}I concentration is above MDA. Therefore, the MDA was calculated by using the Rose criterion²¹. The Rose criterion states that a lesion is no longer visible when the CNR of the lesion falls below a certain threshold value, which can be used to determine the MDA. As the Rose criterion has been validated for use in 2D only, we calculated the CNR of the (2D) central slice through the spheres. The detectability measure K_{2D} was obtained by correcting the CNR for the lesion size according to

$$K_{2D} = \text{CNR}_{2D} \times \sqrt{N} = \frac{C_{H,2D} - C_{B,2D}}{\sigma_{B,2D}} \times \sqrt{N}$$

where CNR_{2D} is the CNR in 2D, $C_{H,2D}$ is the mean voxel value in the sphere 2D region of interest (ROI), $C_{B,2D}$ is the mean voxel value in the 2D background ROI, $\sigma_{B,2D}$ is the standard deviation in the 2D background ROI and N is the number of pixels in the lesion ROI. A K_{2D} threshold value of 8 was used to determine the MDA^{22,23}. The MDA was defined as the activity concentration where the K_{2D} versus activity concentration curve intersected with the threshold value. Regression analysis of the K_{2D} versus activity concentration curves with cubic splines was performed to reduce the influence of noise.

Results

Figure 5.2 and Figure 5.3 show typical examples of the ^{124}I PET/CT and ^{131}I SPECT/CT NEMA phantom images for different activity concentrations. The sphere CNR was calculated and plotted as a function of activity concentration, as shown in Figure 4.1 and Figure 5.5 for the phantom with and without background activity, respectively. Defined as the average ratio between ^{124}I and ^{131}I activity concentration to achieve the same CNR, the DEP was calculated for each combination of PET and SPECT reconstruction methods and for each sphere size (Table 5.2 and Table 5.3).

In general, lower DEPs were obtained for smaller spheres, so that a relatively low ^{124}I activity concentration is sufficient to achieve a similar detectability of lesions with ^{124}I PET/CT as with ^{131}I SPECT/CT. Furthermore, the DEP depends on the reconstruction method that is used. The DEP is higher for the no-PSF no-TOF PET reconstruction method than for the PSF TOF reconstruction method. Furthermore, the DEP is slightly higher for the SC 6i8s method than for the no-SC 6i8s method, and lower for the SC 30i8s method than for the other SPECT reconstruction methods. The differences between DEPs for the PSF TOF and no-PSF no-TOF reconstruction methods are

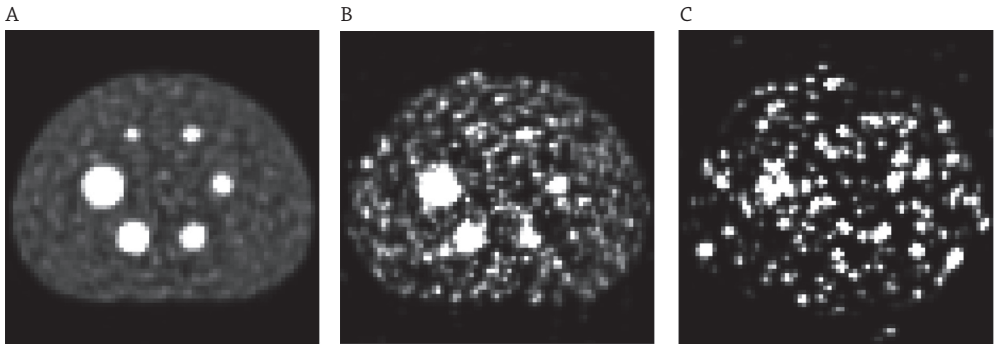


Figure 5.2 Typical ^{124}I PET/CT images of the phantom with activity in the background compartment reconstructed using the PSF TOF method showing the central slice through the spheres for (A) 2.2×10^4 Bq/ml, (B) 9.3×10^2 Bq/ml and (C) 6.5×10^1 Bq/ml in the spheres. The maximum of the gray scale is five times the mean pixel value of the image.

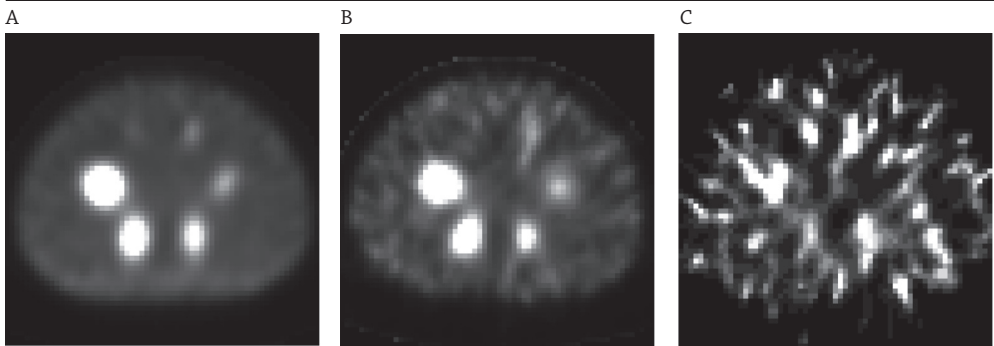


Figure 5.3 Typical ^{131}I SPECT/CT images of the phantom with activity in the background compartment reconstructed using the SC 6i8s method showing the central slice through the spheres for (A) 9.1×10^5 Bq/ml, (B) 4.5×10^4 Bq/ml and (C) 2.2×10^3 Bq/ml in the spheres. The maximum of the gray scale is five times the mean pixel value of the image.

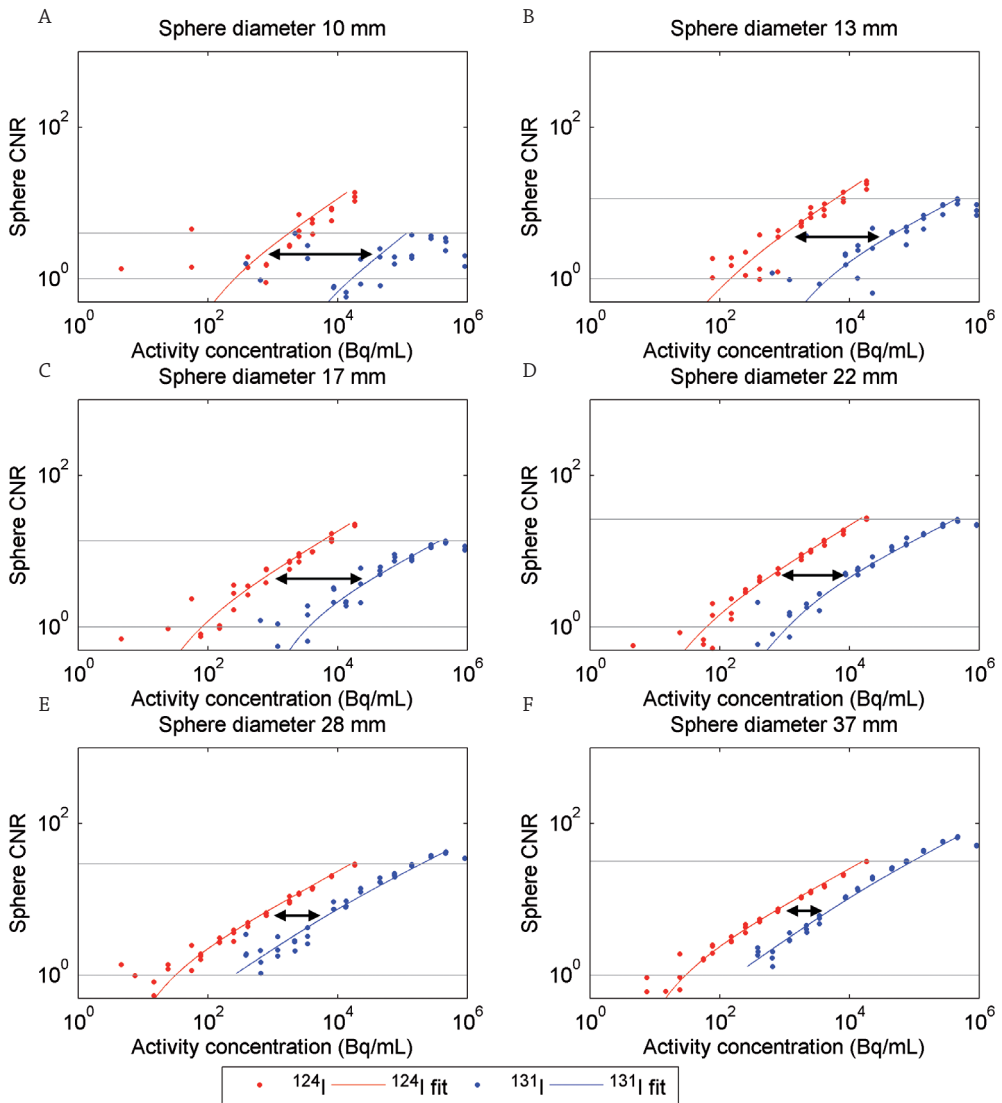


Figure 5.4 The sphere CNR as a function of activity concentration for the ^{124}I (red) and ^{131}I (blue) phantom with background for spheres with a diameter of (A) 10 mm, (B) 13 mm, (C) 17 mm, (D) 22 mm, (E) 28 mm and (F) 37 mm. The DEP is determined by calculating the ratio of the curves, which is graphically represented as the horizontal shift of the curves (black arrow). The gray lines denote the interval where the average ratio between the curves was determined. PET images were reconstructed using the PSF TOF method and SPECT images using the SC 6i8s method.

5

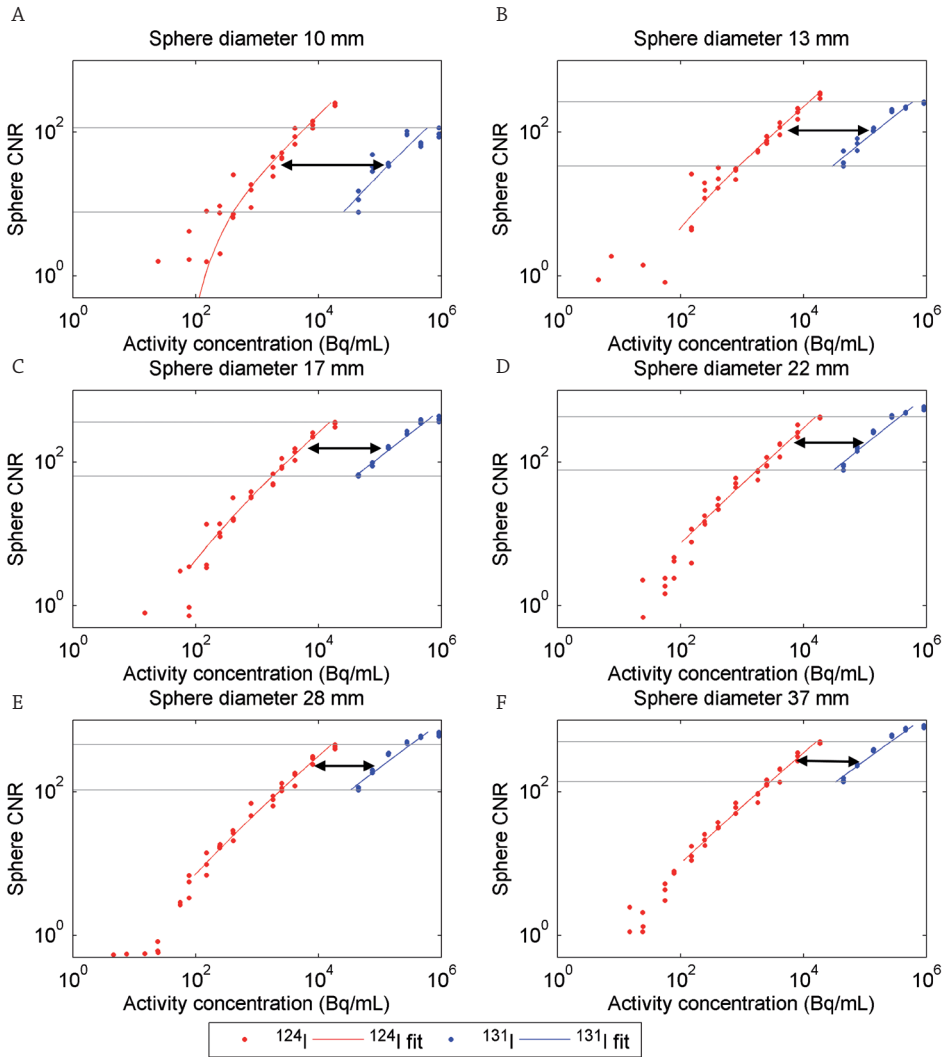


Figure 5.5 The sphere CNR as a function of activity concentration for the ^{124}I (red) and ^{131}I (blue) phantom without background for spheres with a diameter of (A) 10 mm, (B) 13 mm, (C) 17 mm, (D) 22 mm, (E) 28 mm and (F) 37 mm. The DEP is determined by calculating the ratio of the curves, which is graphically represented as the horizontal shift of the curves (black arrow). The gray lines denote the interval where the average ratio between the curves was determined. PET images were reconstructed using the PSF TOF method and SPECT images using the SC 6i8s method.

Table 5.2 DEPs for the phantom with background.

PET reconstruction method	SPECT reconstruction method	10 mm	13 mm	17 mm	22 mm	28 mm	37 mm
PSF TOF	SC 6i8s	1.5	1.9	1.9	4.4	9.0	16.2
no-PSF no-TOF	SC 6i8s	3.6	2.1	3.5	7.8	15.1	23.3
PSF TOF	no-SC 6i8s	1.4	2.1	1.9	4.1	6.8	11.6
no-PSF no-TOF	no-SC 6i8s	3.4	2.1	3.6	7.4	11.9	18.1
PSF TOF	SC 30i8s	0.8	1.3	1.0	1.7	2.1	2.7
no-PSF no-TOF	SC 30i8s	1.8	1.5	2.0	2.8	3.4	3.9

Table 5.3 DEPs for the phantom without background.

PET reconstruction method	SPECT reconstruction method	10 mm	13 mm	17 mm	22 mm	28 mm	37 mm
PSF TOF	SC 6i8s	1.1	2.3	3.3	4.8	5.9	7.0
no-PSF no-TOF	SC 6i8s	1.7	3.2	3.2	4.2	4.8	5.5
PSF TOF	no-SC 6i8s	0.8	1.4	2.0	2.9	4.1	4.3
no-PSF no-TOF	no-SC 6i8s	1.3	2.6	2.6	3.3	4.2	4.0
PSF TOF	SC 30i8s	0.9	1.1	1.4	1.6	1.7	1.8
no-PSF no-TOF	SC 30i8s	1.4	1.7	1.6	1.6	1.7	1.7

Table 5.4 MDAs in Bq/ml for the phantom with background.

Isotope	Reconstruction method	10 mm	13 mm	17 mm	22 mm	28 mm	37 mm
¹²⁴ I	PSF TOF	1.0×10^3	4.1×10^2	1.6×10^2	8.3×10^1	4.4×10^1	2.1×10^1
¹²⁴ I	no-PSF no-TOF	3.0×10^3	5.1×10^2	3.0×10^2	1.9×10^2	8.6×10^1	4.6×10^1
¹³¹ I	SC 6i8s	1.1×10^5	2.2×10^4	8.2×10^3	1.7×10^3	6.5×10^2	
¹³¹ I	no-SC 6i8s	9.6×10^4	2.5×10^4	8.9×10^3	1.4×10^3	4.2×10^2	
¹³¹ I	SC 30i8s	1.9×10^5	3.3×10^4	1.5×10^4	4.2×10^3	2.0×10^3	

smaller for the phantom without activity in the background compartment. In general, the DEPs are slightly smaller for the phantom without activity in the background compartment.

Table 5.4 shows the MDA for the phantom with activity in the background compartment. The MDA of ^{124}I is lower for the PSF TOF reconstruction method than for the no-PSF no-TOF reconstruction method. Similarly, for the 13 and 17 mm spheres, the MDA of ^{131}I is lower for the SC 6i8s reconstruction method than for the no-SC 6i8s reconstruction method. However, for the 10, 22 and 28 mm spheres, the MDA of ^{131}I is higher for the SC 6i8s reconstruction method than for the no-SC 6i8s reconstruction method. The MDAs of the SC 30i8s reconstruction method are larger than for the other SPECT reconstruction methods.

Discussion

A relatively low activity of 74 MBq ^{124}I (~1% of ^{131}I activity) is sufficient to achieve a similar detectability of lesions on ^{124}I PSF TOF PET/CT and ^{131}I SPECT/CT for small spheres ($\leq 10\text{mm}$), since the reported detectability equivalence percentages (DEPs) are close to 1%. False negative ^{124}I PET/CTs as compared with the post-therapy ^{131}I SPECT/CTs may be ascribed to differences in detectability for large lesions ($> 10\text{mm}$) and for no-PSF no-TOF PET, since DEPs are larger than 1%.

The results showed that the DEP was lower for smaller spheres, which indicates that smaller spheres are relatively more easily detected on PET than SPECT images. This can be explained by the fact that the resolution of ^{124}I PET images (approximately 5 mm) generally is higher than the resolution of ^{131}I SPECT images (approximately 15 mm). Therefore, differences in the CNR are large in the range of sphere sizes between 5 and 15 mm.

Activities frequently used in clinical practice and studies are 74 MBq of ^{124}I and 7400 MBq of ^{131}I , thus the ratio of ^{124}I administered activity is approximately 1% of the ^{131}I administered activity. However, as different scan delay times are used after administration, it is necessary to correct for physical decay during the scan delay time. The ^{124}I PET and the ^{131}I SPECT acquisitions are usually performed 24 hours and 7 days after administration respectively, so that at scan time the ^{124}I activity concentration is approximately 1.5% of the ^{131}I activity concentration, if we correct for physical decay. Table 5.2 and Table 5.3 show that for some sphere sizes and reconstruction algorithms, the DEP is smaller than 1.5%. Therefore, for small spheres ($\leq 10\text{mm}$) on PSF TOF PET an activity of 74 MBq ^{124}I is sufficient to achieve similar detectability on the low activity ^{124}I PET/CT as on the high activity ^{131}I SPECT/CT. This shows that false negative low activity ^{124}I PSF TOF PET/CTs as compared with the post-therapy high activity ^{131}I SPECT/CTs are not likely occurring owing to differences in detectability for small lesions. A significant part of the lesions in clinical practice is expected to be smaller than 10 mm²⁴. For larger lesions ($> 10\text{ mm}$) and no-PSF no-TOF PET, the DEP generally is larger than 1.5% and 74 MBq of ^{124}I is not sufficient to achieve similar detectability on the low activity ^{124}I PET/CT as on the high activity ^{131}I SPECT/CT. Reported discrepancies, such as shown the example in Figure 5.1, may therefore be caused by differences in the detectability.

The administered activity of ^{124}I is a factor that should be taken into account when comparing our results with other studies. Several clinical studies have been performed with lower activities than 74 MBq of ^{124}I ^{8,9,11}. The probability of a false negative ^{124}I PET/CT as compared with the post-therapy ^{131}I SPECT/CTs considerably increases with lower ^{124}I dosages. When 25 MBq of ^{124}I and

7400 MBq of ^{131}I is administered, the ratio of ^{124}I and ^{131}I activity concentration is approximately 0.5%, when corrected for physical decay. Since this is lower than the reported DEPs, discrepancies are more likely to occur as a result of differences in detectability.

Activities of 90 MBq are sufficient to achieve similar detectability for lesion diameters up to 17 mm on PSF TOF PET, with DEPs up to 1.8%. Based on DEPs of 3.5% for lesion diameters up to 17mm on no-PSF no-TOF PET, activities as high as 170 MBq of ^{124}I may be warranted to obtain equal detectability. However, a limiting factor for high pre-therapy activities may be thyroid stunning, although stunning due to ^{124}I is controversial, and the origin and existence of stunning still are a hotly debated issue²⁵.

Discrepancies between the ^{124}I and ^{131}I distributions in the tissue as a consequence of differences in uptake/washout may be influenced by additional factors, not assessed in this study. Firstly, unlike phantoms, thyroid tumors or thyroid cancer metastases are inhomogeneous structures consisting of cancer cells, blood vessels and connective tissue with different iodine concentrations, inducing partial volume effects which may affect the measured contrast. Secondly, the uptake of iodine may be influenced by the preparation of the patient, since patients can be prepared either by thyroid hormone withdrawal or recombinant human thyroid-stimulating hormone (rhTSH) stimulation to stimulate iodine uptake. Thirdly, cell damage as a consequence of delivered dose may influence the retention time and may therefore cause differences in the ^{124}I and ^{131}I physiological washout properties. A faster washout of ^{131}I is expected for damaged cells²⁴. Fourthly, the contrast of ^{131}I lesions may increase when delayed scanning is performed, because clearance of the background activity can occur at a faster rate than clearance of the activity in the tumor, so that contra-intuitively, the contrast in the images increases over time¹⁰. One of the few practically adjustable parameters in clinical practice that influences the activity concentration is the delay time between the administration and acquisition. However, the timing of the ^{131}I SPECT/CT acquisition still is a matter of debate in literature. In fact, Salvatori et al. state that 'perfect timing' probably does not exist due to differences in ^{131}I kinetics in different patients and in different metastases²⁶. A scan delay time of 7 days for this study was chosen to allow washout of background activity²⁷. Similar to ^{131}I , the uptake of ^{124}I in metastases shows significant differences among metastases, although most of the metastases showed to have their peak uptake at approximately 24 hours after administration^{28, 29}. Therefore, a scan delay time of 24 hours was used for the ^{124}I PET/CT acquisition.

The purpose of this study was not to investigate the impact of physiological factors, but to quantitatively compare the detectability of lesions on ^{124}I PET/CT and ^{131}I SPECT/CT images. Assuming that physical decay is the only factor affecting the ratio of ^{124}I and ^{131}I activity concentration may not be accurate and the interpretation of the results depends on these assumptions. However, the measured DEPs do not depend on physiological factors. To our knowledge, phantom measurements that compare the detectability of ^{124}I and ^{131}I quantitatively have not been published before.

CNR values lower than 1 were not used for the regression analysis and calculation of the DEP. These values are inherently noisy due to the low number of counts. Furthermore, rounding errors occurred by conversion to the DICOM format when the mean voxel value in the background compartment was lower than 1. Consequently, for low activity concentrations in the phantom without background activity, the standard deviation in the background compartment σ_b was

underestimated and the CNR overestimated. Therefore, these data points (mean background $\text{VOI} < 1$) were not used to determine the DEPs and MDAs.

Diagnostic ^{131}I SPECT/CT with 37-150 MBq of ^{131}I can also be performed for pre-therapy imaging³. However, this study shows that false negative diagnostic scans as compared with the post-therapy scans may be ascribed to the difference in activity that is used, and that false negative results are likely, especially for the smaller lesions that have high MDAs.

False negative ^{124}I PET/CTs as compared with the ^{131}I SPECT/CTs occur when the ^{124}I activity concentration is below minimum detectable activity (MDA) and ^{131}I concentration is above MDA. The MDAs of ^{131}I and ^{124}I were therefore determined for the different reconstruction methods. The MDA of ^{131}I was higher for the SC 6i8s reconstruction method than for the no-SC 6i8s reconstruction method for some sphere sizes (10, 22 and 28 mm). MDAs were not necessarily lower for images obtained with scatter correction, possibly due to the addition of noise introduced in the reconstruction by the noisy scatter projections. Unfortunately, no ^{131}I MDAs could be obtained for the 37 mm spheres because not enough data was available for low CNRs.

The DEPs were lower for the 30i8s than for the 6i8s SPECT reconstruction method, because generally lower CNRs were obtained for the 30i8s than for the 6i8s SPECT reconstruction method. This was caused by the fact that the background noise level in the images increased with the number of iterations, which lowered the CNR. Therefore, the ^{124}I activity concentration expressed as a percentage of the ^{131}I activity concentration required to achieve the same CNR (i.e. the DEP), was lower for the 30i8s than for the 6i8s SPECT reconstruction method.

The sizes of the lesions in Figure 5.1 are 5 mm, 7 mm (Figure 5.1B) and 12 mm (Figure 5.1D), based on the co-registered CT data. The DEP for the 10 mm sphere is between 1.3 and 3.4, depending of the lesion-to-background ratio (Table 5.2 and Table 5.3), so that a relatively low activity of 74 MBq ^{124}I (~1% of ^{131}I activity) may not be sufficient to achieve a similar detectability. The false negative ^{124}I PET/CTs as compared with the ^{131}I SPECT/CTs may therefore be ascribed to differences in detectability. Unfortunately, no DEPs were calculated for sphere diameters smaller than 10 mm. In general, discrepancies between ^{124}I PET/CTs and ^{131}I SPECT/CTs depend on many factors, and this study shows that the dosage of ^{124}I should be chosen carefully.

Conclusion

A relatively low activity of 74 MBq ^{124}I (~1% of ^{131}I activity) is sufficient to achieve a similar detectability of lesions on ^{124}I PSF TOF PET/CT and ^{131}I SPECT/CT for small spheres ($\leq 10\text{mm}$), since the reported DEPs are close to 1%. Activities of 90 MBq of ^{124}I are sufficient to achieve similar detectability for lesion diameters up to 17 mm on PSF TOF PET, with DEPs up to 1.8%. False negative ^{124}I PET/CTs as compared with the post-therapy high activity ^{131}I SPECT/CTs may be ascribed to differences in detectability for large lesions ($> 10\text{mm}$) and for no-PSF no-TOF PET, since DEPs are larger than 1%. Based on DEPs of 3.5% for lesion diameters up to 17mm on no-PSF no-TOF PET, activities as high as 170 MBq of ^{124}I may be warranted to obtain equal detectability.

References

- 1 M. Luster et al., "Guidelines for radioiodine therapy of differentiated thyroid cancer," *Eur. J. Nucl. Med. Mol. Imaging* 35, 1941–1959 (2008).
- 2 C. Ma, J. Xie, and A. Kuang, "Is empiric ^{131}I therapy justified for patients with positive thyroglobulin and negative ^{131}I whole-body scanning results?," *J. Nucl. Med.* 46, 1164–70 (2005).
- 3 F. Pacini et al., "Therapeutic doses of iodine-131 reveal undiagnosed metastases in thyroid cancer patients with detectable serum thyroglobulin levels," *J. Nucl. Med.* 28, 1888–1891 (1987).
- 4 F. Pacini et al., "Outcome of differentiated thyroid cancer with detectable serum Tg and negative diagnostic (^{131}I) whole body scan: comparison of patients treated with high (^{131}I) activities versus untreated patients," *J. Clin. Endocrinol. Metab.* 86, 4092–4097 (2001).
- 5 M. Urhan et al., "Iodine-123 as a diagnostic imaging agent in differentiated thyroid carcinoma: A comparison with iodine-131 post-treatment scanning and serum thyroglobulin measurement," *Eur. J. Nucl. Med. Mol. Imaging* 34, 1012–1017 (2007).
- 6 Y.E. Erdi et al., "Radiation dose assessment for I-131 therapy of thyroid cancer using I-124 PET imaging," *Clin. Positron Imaging* 2, 41–46 (1999).
- 7 L.S. Freudenberg et al., "Value of ^{124}I -PET/CT in staging of patients with differentiated thyroid cancer," *Eur. Radiol.* 14, 2092–2098 (2004).
- 8 C. De Pont, S. Halders, J. Bucerius, F. Mottaghy, and B. Brans, " ^{124}I PET/CT in the pretherapeutic staging of differentiated thyroid carcinoma: Comparison with posttherapy ^{131}I SPECT/CT," *Eur. J. Nucl. Med. Mol. Imaging* 40, 693–700 (2013).
- 9 L.S. Freudenberg, W. Jentzen, S.P. Müller, and A. Bockisch, "Disseminated iodine-avid lung metastases in differentiated thyroid cancer: A challenge to ^{124}I PET," *Eur. J. Nucl. Med. Mol. Imaging* 35, 502–508 (2008).
- 10 G.R. Khorjekar et al., "Do negative ^{124}I pretherapy positron emission tomography scans in patients with elevated serum thyroglobulin levels predict negative ^{131}I posttherapy scans?," *Thyroid* 24, 1394–1399 (2014).
- 11 G.K. Lammers, J.P. Esser, P.C.M. Pasker, M.E. Sanson-van Praag, and J.M.H. de Klerk, "Can I-124 PET/CT predict pathological uptake of therapeutic dosages of radioiodine (I-131) in differentiated thyroid carcinoma?," *Adv. Mol. Imaging* 04, 27–34 (2014).
- 12 H.T.T. Phan et al., "The diagnostic value of ^{124}I -PET in patients with differentiated thyroid cancer," *Eur. J. Nucl. Med. Mol. Imaging* 35, 958–965 (2008).
- 13 D. Van Nostrand et al., " ^{124}I positron emission tomography versus ^{131}I planar imaging in the identification of residual thyroid tissue and/or metastasis in patients who have well-differentiated thyroid cancer," *Thyroid* 20, 879–883 (2010).
- 14 J.W. Kist, B. de Keizer, M.P.M. Stokkel, O.S. Hoekstra, and W.V. Vogel, "Recurrent differentiated thyroid cancer: towards personalized treatment based on evaluation of tumor characteristics with PET (THYROPET Study): study protocol of a multicenter observational cohort study," *BMC Cancer* 14, 405 (2014).
- 15 D. Rubello et al., "Iodine-131 radio-guided surgery in differentiated thyroid cancer: Outcome on 31 patients and review of the literature," *Biomed. Pharmacother.* 61, 477–481 (2007).

- 16 V. Preylowski et al., "Is the image quality of I-124-PET impaired by an automatic correction of prompt gammas?," *PLoS One* 8, 1–8 (2013).
- 17 K.P. Willowson, M. Tapner, Q.U.E.S.T.I. Team, and D.L. Bailey, "A multicentre comparison of quantitative (90)Y PET/CT for dosimetric purposes after radioembolization with resin microspheres: The QUEST Phantom Study," *Eur. J. Nucl. Med. Mol. Imaging* 42, 1202–1222 (2015).
- 18 Y.K. Dewaraja et al., "MIRD pamphlet no. 23: Quantitative SPECT for patient-specific 3-dimensional dosimetry in internal radionuclide therapy," *J. Nucl. Med.* 53, 1310–1325 (2012).
- 19 Y.K. Dewaraja et al., "MIRD pamphlet no. 24: Guidelines for quantitative ^{131}I SPECT in dosimetry applications," *J. Nucl. Med.* 54, 2182–8 (2013).
- 20 R.O. Duda and P.E. Hart, "Use of the Hough transformation to detect lines and curves in pictures.," 15, (1972).
- 21 A. Rose, "The sensitivity performance of the human eye on an absolute scale," *J. Opt. Soc. Am.* 38, 196–208 (1948).
- 22 D.S. Bright, D.E. Newbury, and E.B. Steel, "Visibility of objects in computer simulations of noisy micrographs," *J. Microsc.* 189, 25–42 (1998).
- 23 T. Carlier et al., "Assessment of acquisition protocols for routine imaging of Y-90 using PET/CT.," *EJNMMI Res.* 3, 11 (2013).
- 24 W. Jentzen et al., "Assessment of lesion response in the initial radioiodine treatment of differentiated thyroid cancer using ^{124}I PET imaging," *J. Nucl. Med.* 55, 1759–65 (2014).
- 25 I.R. McDougall and A. Iagaru, "Thyroid stunning: Fact or fiction?," *Semin. Nucl. Med.* 41, 105–112 (2011).
- 26 M. Salvatori et al., "Determining the appropriate time of execution of an I-131 post-therapy whole-body scan: comparison between early and late imaging.," *Nucl. Med. Commun.* 34, 900–908 (2013).
- 27 A. Chong et al., "Improved detection of lung or bone metastases with an I-131 whole body scan on the 7th day after high-dose I-131 therapy in patients with thyroid cancer," *Nucl. Med. Mol. Imaging* (2010). 44, 273–281 (2010).
- 28 W. Jentzen, L. Freudenberg, E.G. Eising, W. Sonnenschein, J. Knust, and A. Bockisch, "Optimized ^{124}I PET dosimetry protocol for radioiodine therapy of differentiated thyroid cancer.," *J. Nucl. Med.* 49, 1017–1023 (2008).
- 29 C. Pettinato et al., "Pretherapeutic dosimetry in patients affected by metastatic thyroid cancer using ^{124}I PET/CT sequential scans for ^{131}I treatment planning," *Clin. Nucl. Med.* 39, e367–e374 (2014).



Impact of reconstruction parameters on quantitative ^{131}I SPECT

Based on:

C.A.J. van Gils, C. Beijst, R. van Rooij, H.W.A.M. de Jong, "Impact of reconstruction parameters on quantitative ^{131}I SPECT", *Submitted for publication*

Abstract

Background

Radioiodine therapy using ^{131}I is widely used for treatment of thyroid disease or neuroendocrine tumors. Monitoring treatment by accurate dosimetry requires quantitative imaging. The high energy photons however render quantitative SPECT reconstruction challenging, potentially requiring accurate correction for scatter and collimator effects. The goal of this work is to assess the effectiveness of various correction methods on these effects using phantom studies.

Methods

A SPECT/CT acquisition of the NEMA IEC body phantom was performed. Images were reconstructed using the following parameters: 1) without scatter correction, 2) with triple energy window (TEW) scatter correction and 3) with Monte Carlo-based scatter correction. For modelling the collimator-detector response (CDR), both a) geometric Gaussian CDRs as well as b) Monte Carlo simulated CDRs were compared. Quantitative accuracy, contrast to noise ratios and recovery coefficients were calculated, as well as the background variability and the residual count error in the lung insert.

Results

The Monte Carlo scatter corrected reconstruction method was shown to be intrinsically quantitative, requiring no experimentally acquired calibration factor. It resulted in a more accurate quantification of the background compartment activity density compared with TEW or no scatter correction. The quantification error relative to a dose calibrator derived measurement was found to be <1%, -26% and 33% respectively. The adverse effects of partial volume were significantly smaller with the Monte Carlo simulated CDR correction compared with geometric Gaussian or no CDR modelling. Scatter correction showed a small effect on quantification of small volumes. When using a weighting factor, TEW correction was comparable to Monte Carlo reconstruction in all measured parameters, although this approach is clinically impractical since this factor is likely to be patient dependent.

Conclusion

Monte Carlo based scatter correction including accurately simulated CDR modelling is the most robust and reliable method to reconstruct accurate quantitative ^{131}I SPECT images.

Introduction

Iodine-131 is a beta emitting isotope often used for radionuclide therapy. It is utilized as a sodium iodide salt to treat, for example, hyperthyroidism due to Graves' disease¹. It can also be used for imaging or treating neuroblastoma and pheochromocytoma when attached as a labelling agent to metaiodobenzylguanidine (MIBG)^{2,3}.

While the emitted high energy beta particles are responsible for the therapeutic effect, the isotope also emits high energy gamma rays which can be used in (whole body) scintigraphy or SPECT(/CT) imaging of the activity distribution. These measurements can be used to stage and monitor patients and perform patient specific dosimetry. The latter requires quantitative images, meaning the reconstructed voxel values relate directly and consistently to the local activity concentrations (Bq/ml), or in combination with for example a dose point kernel, to absorbed dose (Gy). As quantitative SPECT remains a challenge, guidelines have been published with recommendations regarding (^{131}I) quantitative SPECT^{4,5}.

^{131}I emits a wide range of gamma energies, the most abundant of which has an energy of 364 keV with a yield of 81.5 % and is the preferred emission used in imaging. The emitted higher energy photons (637 and 723 keV) can scatter into the 364 keV photopeak window, resulting in misplaced activities, lower image contrast and increased image noise. This effect has to be corrected for to optimize image quality and allow for quantification. The Triple Energy Window (TEW) method is commonly used to correct for scatter^{6,7}. In this technique, two additional windows (acquired over energies both above and below the primary 364 keV photopeak window) are used to estimate and correct for the fraction of scattered photons in the photopeak window by incorporating the scatter projection data in the forward-projection step. This correction is, however, based on the assumption that the energy spectrum of scattered photons in the photopeak window can be expressed as a linear combination of the two scatter windows and the additional windows detect nothing but scattered photons. In addition, the application of noisy measured scatter projections for scatter correction increases image noise⁸.

Alternatively, model-based reconstruction methods (i.e. methods which use a model, or forward projector, in an iterative reconstruction scheme) have been suggested by several groups⁹⁻¹¹. These methods do not require acquisition of additional (scatter) energy windows, make no assumptions about the shape of the acquired energy spectrum and have less impact on reconstructed image noise. Since, in general, the performance of these methods relies on the correctness of the model, Monte Carlo-based reconstruction methods that incorporate all relevant photon physics are regarded to result in the most accurate images¹². However, this is at the cost of increased complexity and reconstruction time.

An additional challenge in ^{131}I imaging is the presence of a substantial partial volume effect due to the use of high energy collimators with low resolution. The partial volume effect results in underestimation of activity in small hot objects like tumors. This effect can be partially compensated for by including the so called collimator detector response (CDR) in the model used for reconstruction. The CDR represents how a point source of a given energy and at given distance from the collimator is measured by the detector. CDR can be approximated by analytically derived geometric (Gaussian) CDRs, but these models lack realistic description of septal penetration, collimator scatter and partial energy deposition that may be relevant in ^{131}I imaging. Therefore



accurate tabulated CDRs generated using highly detailed Monte Carlo particle simulation software have been suggested¹³⁻¹⁵.

Since the above mentioned sophisticated methods may introduce complexity, the purpose of this study was to investigate the essential scatter- and CDR-correction requirements for performing quantitative ¹³¹I SPECT. These were derived by comparing reconstructions of phantom acquisitions with- and without scatter correction (both TEW and Monte Carlo based), and with- and without CDR correction (both geometric Gaussian and Monte Carlo based).

Materials and Methods

Phantom description

A NEMA IEC body phantom was used which contains six fillable spheres with inner diameters of 10, 13, 17, 22, 28 and 37 mm. The phantom also contained a 51 mm diameter lung insert filled with polystyrene beads and water. The lung insert and the two largest spheres did not contain activity, whereas the other spheres contained an ¹³¹I solution with an activity concentration of 1.7 MBq/ml. The background compartment with a volume of 9700 ml was filled with an activity concentration of 0.17 MBq/ml, leading to a sphere-to-background ratio of 10:1. The total activity in the phantom at the time of acquisition was 1.6 GBq.

The sphere-to-background ratio was chosen because uptake percentages per gram of tissue range from 0.01 to 0.13 % for pheochromocytoma using MIBG¹⁶. For thyroid carcinoma using NaI this range is 0.09 to 0.47 % per gram of tissue¹⁷. Uptake of the thyroid in hyperthyroidism is typically much higher, reaching more than 1 % per gram of tissue¹⁸. A ratio of 10:1 corresponds to an uptake of approximately 0.1 % per gram, thereby falling within the large range of clinically encountered uptake percentages.

SPECT/CT acquisition

Acquisitions were performed using a Siemens Symbia T16 utilizing the high energy collimator over 128 angles with an acquisition time of 25 seconds per angle. The high energy collimator has 4 mm diameter hexagonal holes, a septal thickness of 2 mm and a hole length of 59.7 mm. A 15 % energy window width was used for the 364 keV photopeak, and adjacent upper- and lower-scatter windows a quarter of the photopeak window width were recorded simultaneously. The acquired matrix size was 128x128 pixels and a noncircular orbit was used. The average counts per projection angle was approximately 700,000 counts for the primary photopeak window, and approximately 110,000 and 70,000 counts for the lower- and upper-scatter window respectively. A CT was acquired for attenuation correction purposes, as well as for accurate determination of the location of the spheres and the lung insert in the phantom during processing.

UMCS

All reconstructions in this study were performed using the Utrecht Monte Carlo System (UMCS), which allows for ordered subset expectation maximization (OSEM) reconstruction using a variety of modeling options. These options include window based scatter correction, several CDR models and a Monte Carlo simulator that acts as a projector for model based reconstruction. In this work, all reconstructions were performed using convolution-based forced detection¹⁹. An extensive

Table 6.1 Gamma- and beta emissions with a yield of >1% of ¹³¹I decay (National Nuclear Data Center).

Gamma emissions		Beta emissions	
Energy (keV)	Yield (%)	Energy (keV)	Yield (%)
80.185	2.62	69.36	2.08
284.31	6.12	96.62	7.23
364.49	81.5	191.58	89.6
636.99	7.16		
722.91	1.77		

Half-life: 8.0252 days

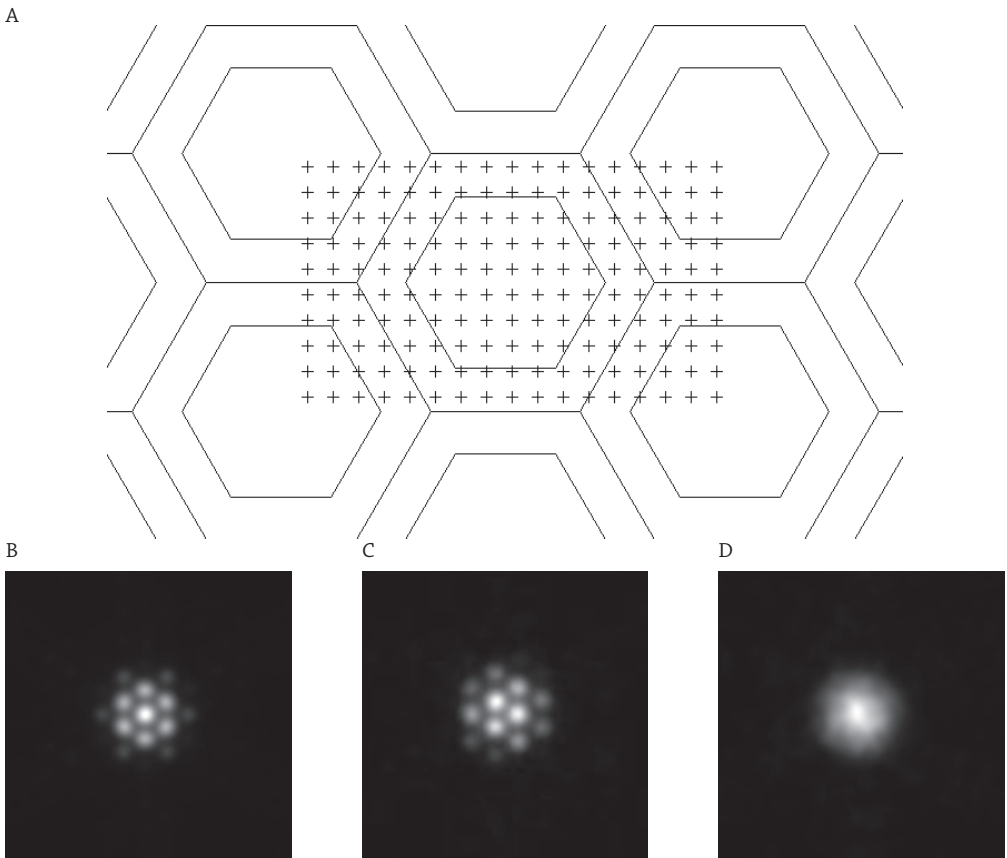


Figure 6.1 CDR sampling grid (A), examples of a non-averaged CDR directly above a hole (B), of a non-averaged CDR above a septum (C) and of an averaged CDR (D). The CDR examples shown in (B), (C), and (D) were obtained by simulating a point source at a distance of 12 cm from the collimator surface.

description of UMCS is provided elsewhere²⁰ and the framework has been previously validated for technetium-99m²¹, thallium-201²², holmium-166¹³ and yttrium-90¹⁴. For this study, the ¹³¹I emission spectrum and CDR were added to the framework. For validation, both the performance of the ¹³¹I Monte Carlo forward projector and the iterative reconstruction scheme as a whole were evaluated.

Implementation of ¹³¹I in the forward projector

The photon spectrum of ¹³¹I was incorporated in UMCS, including all gamma emissions (see Table 6.1 for a selection) and Bremsstrahlung photon contributions. The Bremsstrahlung spectrum was obtained by simulating a point source with ¹³¹I beta emissions in a water sphere in MCNPX 2.5.0²³, as described in previous work for ¹⁶⁶Ho and ⁹⁰Y^{13, 14}. The resulting total photon energy spectrum was treated as a probability density function meaning the energies were sampled proportionally to their relative abundance by UMCS when simulating projections.

To incorporate the physics of the forward projection onto the collimator detector system, such as collimator septal penetration, geometric broadening and lead x-rays, the collimator detector response was modelled using MCNPX. By simulating point sources of various energies at various distances to the collimator, an emission energy, energy window and collimator specific lookup table of CDRs for UMCS was created.

For all MCNPX calculations, 10⁸ source photons were simulated. Both photon- and electron physics were simulated and particle tracking was terminated when the energy of the tracked particle dropped below 45 keV.

Because of the relatively large hole diameter of the high energy collimator, the CDR is visually dependent on sampling location relative to the collimator grid. This is especially evident when the point source is located close to the collimator. A point source centered directly above a hole showed a significantly different response compared to a point source directly above a septum (compare Figure 6.1B to Figure 6.1C). To compensate for this effect, a grid of source positions (Figure 6.1A) was sampled and the resulting detector responses were spatially averaged. Figure 6.1D shows an example of an averaged CDR. All CDRs in Figure 6.1 were simulated at 12 cm distance from the collimator surface. As UMCS uses 1-dimensional CDRs as an input, the resulting CDRs were subsequently rotationally averaged. In addition to MCNPX simulated CDRs, geometric Gaussian CDRs were also implemented as a reconstruction option²⁴.

For the implementation of TEW correction, the lower- and upper- scatter window were combined to form a scatter estimate projection S_{pp} in the photo peak window by applying on

$$S_{pp} = k_{TEW} \frac{w_{pp}}{2} \left(\frac{P_{s1}}{w_{s1}} + \frac{P_{s2}}{w_{s2}} \right)$$

a pixel-by-pixel basis, where w_{pp} is the width of the photopeak window, w_{s1} and w_{s2} are the widths of the scatter windows and P_{s1} and P_{s2} are the scatter projections^{6, 7, 25, 26}, k_{TEW} is ideally equal to one. During reconstruction, may be added to a simple forward projector that does not include scatter events²⁵. Since overestimation of scatter was previously reported in literature^{27, 28}, the impact of an added weighting factor k_{TEW} was investigated in this study. Similar to the dual energy window k-factor, k_{TEW} needs to be determined from simulations or measurements.

Table 6.2 Reconstruction methods used in this study.

Method name	Scatter correction	CDR correction
NoScatNoCDR	None	None
NoScatGaussCDR	None	Gaussian
NoScatSimCDR	None	MCNPX simulated CDR
TEWSimCDR	TEW (optimized k_{TEW})	MCNPX simulated CDR
MCSimCDR	Monte Carlo	MCNPX simulated CDR

Validation of the forward projector

The accuracy of forward projections generated by UMCS was determined by comparison to measured line spread functions (LSFs). The LSFs were measured with various thicknesses (10, 50 and 100 mm) of Poly(methyl methacrylate) (PMMA) between the line source and detector. Potential backscatter was accounted for by placing 55 mm of PMMA behind the line source as viewed from the detector. There was no additional spacing between the PMMA and the collimator surface. The line source was placed in a plane parallel to the detector surface and the average LSF over a length of 10 cm was calculated.

Reconstruction

To compare the effect of CDR- and scatter correction techniques, 5 different reconstruction methods were employed. For each method, a maximum of 50 iterations with 8 subsets was calculated. The methods and their names are listed in Table 6.2. Using the voxel volume, isotope-specific abundancies and acquisition time, UMCS generates pixel values expressed in units of Bq/ml when using simulated CDRs. This is possible as the detector sensitivity is automatically determined when simulating CDRs. For the Monte Carlo scatter correction, 10^6 photon tracks were simulated as a higher number of simulated tracks does not lead to a significant increase in image quality²⁹. Depending on the processor speed, one iteration took approximately 2 to 5 minutes on a regular office desktop pc. No post-reconstruction filtering was used.

Activity estimation accuracy

To study whether an over- or underestimation of scatter was present in the phantom measurements as a consequence of the TEW scatter correction method, a line profile through a reconstruction of the (homogeneously filled) background compartment of the NEMA phantom was analyzed. An ideal reconstruction of a homogeneous activity distribution yields a flat line profile. Therefore, if a line profile through the background compartment shows a sloped profile, this indicates that scatter is either undercompensated (sloped up towards center of the phantom) or overcompensated (sloped down towards center of the phantom), provided the CT attenuation correction works correctly. To reduce image noise in the profiles, 15 background slices were averaged and filtered using a 1 cm width Gaussian. Profiles were compared to average background concentration values in the phantom as measured using a dose calibrator.

Monte Carlo simulations were used to determine the optimal k_{TEW} that yielded an accurate scatter estimation. Using an accurate digital equivalent of the NEMA phantom, projections P_{s1} and P_{s2} were simulated, as well as a scatter-only projection contribution in the photopeak window. Using pixel-by-pixel simple ordinary least squares (excluding pixels clearly outside of the phantom), a single optimized k_{TEW} was found for all projections. The mean quantification error was determined for the different reconstruction methods by averaging over the entire background VOI of the phantom and comparing with dose calibrator derived measurements.

Sphere and lung insert quantification

The contrast to noise ratio (CNR) for each sphere in the phantom was determined by

$$CNR = \left| \frac{C - C_B}{\sigma_{BG}} \right|,$$

where C is the average number of counts in the sphere of interest, C_B is the average number of counts in the background VOI and σ_{BG} is the standard deviation in the background VOI. The recovery coefficients for the hot spheres (also called hot sphere contrast) are calculated by

$$Q_H = \frac{\frac{C_H}{C_B} - 1}{\frac{a_H}{a_B} - 1},$$

where C_H is the average number of counts in the hot sphere volume of interest (VOI), a_H is the activity concentration in the sphere and a_B is the concentration in the background. In this work $a_H/a_B \approx 10$. The cold sphere contrast for the two largest spheres was calculated by

$$Q_C = \left(1 - \frac{C_C}{C_B} \right),$$

where C_C is the average number of counts in the cold sphere VOI. The residual error in the lung insert was defined as

$$\Delta C_{lung} = \frac{C_{lung}}{C_B},$$

where C_{lung} is the average number of counts in the lung insert VOI. For the background compartment, the coefficient of variation was defined as

$$COV_{BG} = \frac{\sigma_{BG}}{C_B}.$$

Additionally, the recovered activity for the hot spheres and the recovered activity density in the background compartment were also compared to dose calibrator measurement derived values.

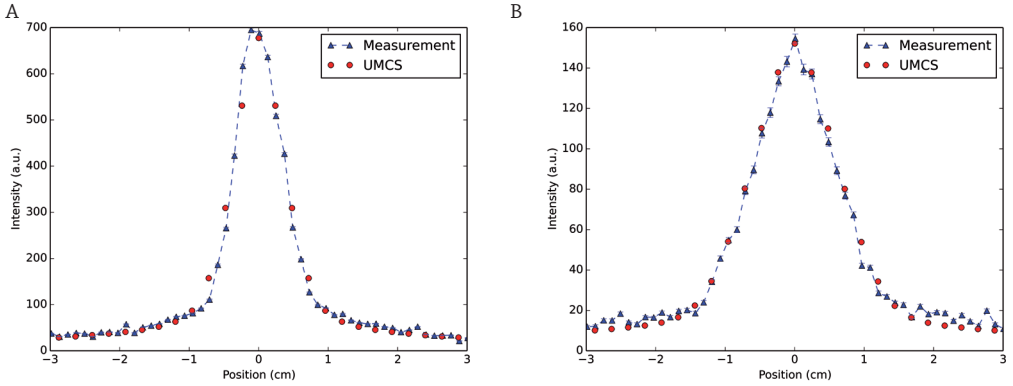


Figure 6.2 Measured and UMCS simulated line spread functions for 1 cm (A) and 10 cm (B) of PMMA between line source and the collimator surface. The error bars show the standard deviation in the measured points over the 10 cm averaging distance.

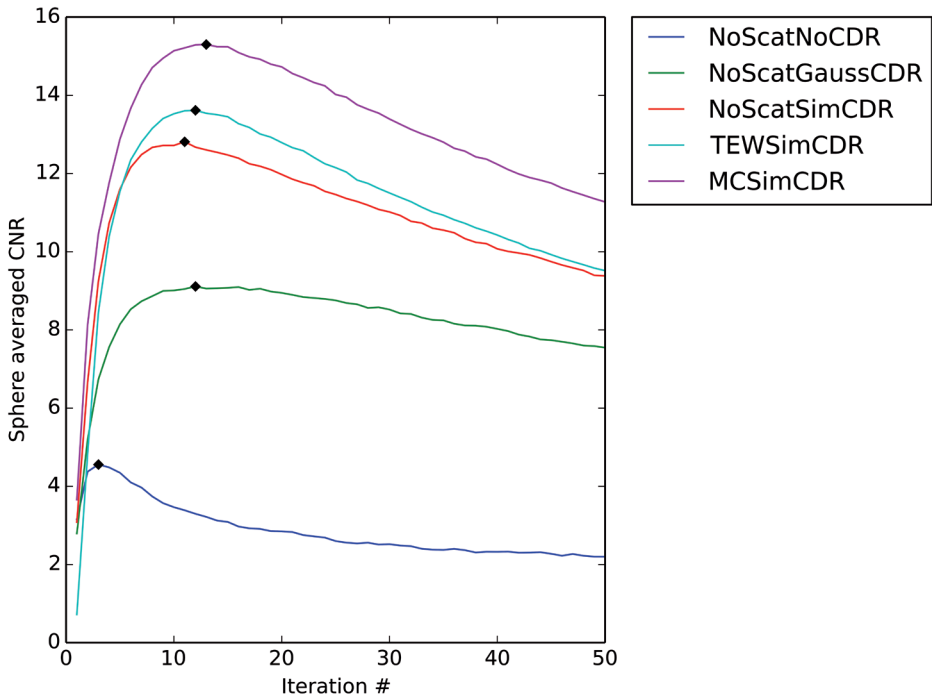


Figure 6.3 CNR averaged over all spheres as a function of iteration number for all methods. The used number of iterations per method for the remainder of this work is indicated by black diamonds.



NEMA NU-2 2007 analysis guidelines for the phantom were adopted wherever possible (National Electrical Manufacturers Association, 1994). A 3D analysis instead of 2D analysis was performed to reduce the influence of image noise and placement errors of the VOIs on the calculated parameters. The locations of the centers of the spheres and the lung insert were derived from the CT acquisition. For the spheres, spherical VOIs were drawn around these centers with a diameter corresponding to the actual diameter of the spheres. For the lung insert, a 30 mm diameter cylindrical VOI was drawn around the center of the insert. For the background VOI the entire background compartment was used, omitting the lung insert- and sphere VOIs dilated by 20 mm. To avoid effects of the edge of the phantom, the outer 20 mm of the phantom was not used in both the background- and lung insert VOIs.

The number of iterations in the reconstruction on which the analyses were performed was determined by maximizing the CNR over all spheres for each reconstruction method.

Results

Implementation and validation of ^{131}I reconstructions

Figure 6.2 shows a comparison of measured and simulated line profiles for two thicknesses of PMMA between the line source and the detector. The UMCS LSFs show agreement with measured line profiles at both thicknesses. Measurements using 5 cm of PMMA result in similar agreement (data not shown). Note that in these simulations only the forward projector of UMCS is used.

In Figure 6.3, the averaged CNR was plotted as a function of the number of iterations. This shows that the highest average CNR is obtained after 3, 12, 11, 12 and 13 for NoScatNoCDR, NoScatGaussCDR, NoScatSimCDR, TEWSimCDR and MCSimCDR respectively. These numbers of iterations were later used when comparing the different reconstruction methods.

Scatter estimation accuracy

Figure 6.4B and C show measured profiles of the reconstructed background of the phantom at two different locations, indicated in the Figure 6.4A. The upper line profile is shown in Figure 6.4B, the lower line profile is shown in Figure 6.4C. The grey rectangles in the graphs indicate the true activity concentration in the background as deduced from dose calibrator measurements. The effects of broadening due to CDR are seen at the edges of the phantom and at the edges of the lung insert. Because only reconstructions incorporating Monte Carlo simulated CDRs yield quantitative results without calibration measurements, making scatter estimation accuracy feasible, the methods using a Gaussian- or no CDR are not shown in this figure.

Monte Carlo based scatter correction combined with simulated CDR provides the most accurate quantitative result. When using the conventional TEW scatter estimation with $k_{\text{TEW}}=1$, a clear overestimation of scatter is seen as a significant underestimation of activity density and a slightly sloped profile in the background compartment. No scatter correction leads to underestimation of scatter, thus overestimation of activity concentration, also leading to a slightly sloped profile. Monte Carlo scatter correction on the other hand results in accurate quantification and a relatively flat profile. Due to effects of the CDR correction however, a totally flat profile is not achieved, regardless of the used scatter correction method.

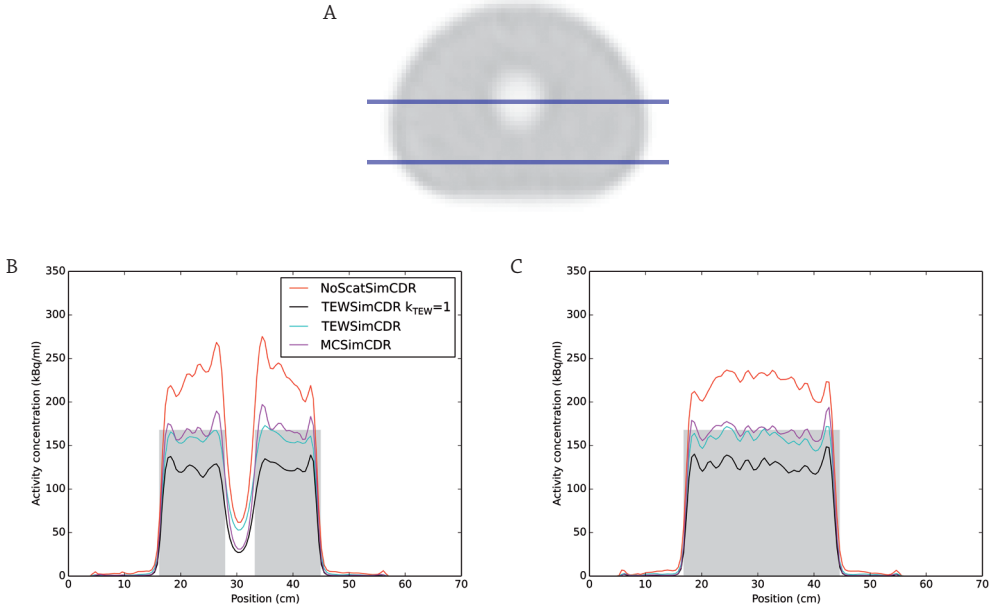


Figure 6.4 Location of line profiles through the background compartment of the phantom (A), upper indicated line profile (B) and lower indicated line profile (C).

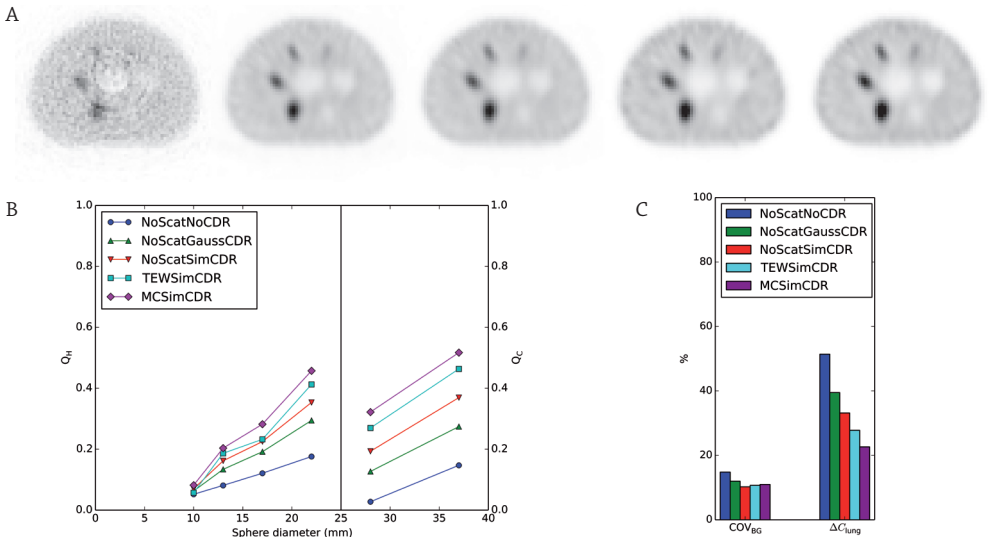


Figure 6.5 Examples of reconstructed slices (left to right) NoScatNoCDR, NoScatGaussCDR, NoScatSimCDR, TEWSimCDR and MCSimCDR (A). The maximum of the gray scale used for images (A), (B) and (C) is six times the mean background value for each method. Hot- and cold sphere contrast as a function of sphere diameter (B) and corresponding residual error in the lung insert and coefficient of variation in the background (C).

An optimal weighting factor k_{TEW} of 0.67 is found for the digital equivalent phantom. It has to be noted however, that per acquisition frame k_{TEW} varied from 0.64 to 0.69, depending on the angle. When using the optimal weighting factor in the TEW method, the resulting profile from the physical image data is similar to the Monte Carlo scatter correction. Consequently, this optimized weighting factor is used in all further comparisons. Averaged over the entire background VOI of the phantom, a mean quantification error of activity density of less than 1% is found for both Monte Carlo and weighted TEW scatter correction when compared to the activity derived from the dose calibrator measurement. Applying no scatter correction or using a k_{TEW} weighting factor of 1 results in a mean quantification error of 33% or -26% respectively.

Sphere and lung insert quantification

Figure 6.5 shows example slices through the phantom (A), the measured recovery coefficients for all spheres (C), their corresponding residual error in the lung insert and coefficient of variation in the background for the various reconstruction categories (C). NoScatNoCDR shows the lowest recovery coefficients, whereas MCSimCDR shows the highest recovery coefficients. For the largest hot sphere, a maximum recovery coefficient of approximately 0.47 is found, whereas for the largest cold sphere a cold sphere contrast of approximately 0.53 is seen. Scatter correction is seen to be less important than CDR correction. The 10 mm diameter sphere is small compared to the CDR broadening and therefore poorly resolved regardless of the applied scatter- and CDR correction. The coefficient of variation in the background is comparable between reconstruction methods. The accuracy of the reconstruction of the lung insert is also shown to be more dependent on the CDR correction than the scatter correction.

Table 6.3 shows the recovered activity and the recovered activity density in the hot spheres and background compartment respectively. The deviation from the dose calibrator derived measurements is shown between brackets. All spheres show significant deviations from the derived activities regardless of reconstruction method. NoScatSimCDR performs slightly better in sphere activity quantification but shows a much larger deviation in background compartment activity density. TEWSimCDR and MCSimCDR show equivalent quantitative performance.

Discussion

Using phantom experiments, the impact of various scatter- and CDR correction methods on ^{131}I SPECT reconstruction was evaluated in this study.

The agreement between measured- and simulated line spread functions indicates that the forward projector used in UMCS reconstructions yields accurate projection simulations for ^{131}I , both in terms of CDR- and scatter simulation. Accurate attenuation correction is also demonstrated.

Recognizing over- or undercompensation by scatter correction techniques is not trivial without quantitative reconstruction capabilities. That is, overcompensation of scatter or background may result in a higher apparent contrast as compared with scatter correction methods that are quantitatively accurate. Moreover, accurate scatter correction does not necessarily lead to a homogeneous distribution of activity due to CDR correction effects. Finally, applying no scatter correction can yield a slightly higher recovered activity due to misplacement of activity

Table 6.3 Recovered activity in the hot spheres and activity concentration in the background. Deviation from dose calibrator measurement is shown between brackets.

Method	10 mm (MBq)	13 mm (MBq)	17 mm (MBq)	22mm (MBq)	Background (MBq/ml)
NoScatSimCDR	0.17 (-81%)	0.59 (-70%)	1.65 (-62%)	5.12 (-46%)	0.19 (14%)
TEWSimCDR	0.15 (-83%)	0.56 (-72%)	1.51 (-65%)	4.80 (-49%)	0.17 (0%)
MCSimCDR	0.15 (-83%)	0.55 (-72%)	1.55 (-64%)	4.84 (-49%)	0.17 (-1%)
Dose calibrator	0.89	1.95	4.37	9.47	0.17

by erroneous detection of scattered photons in the primary photopeak energy window. Note that the latter does not necessary lead to a higher contrast as the background compartment activity density is also overestimated.

Correcting for scatter, both using Monte Carlo and TEW (using an appropriate k_{TEW}), yields only slightly better hot sphere recovery coefficients, cold sphere contrast and residual lung error results compared to no scatter correction. For resolving the hot- and cold spheres and the lung insert, scatter correction is less important than CDR correction.

Accurate quantification of background activity density (and quantification of details significantly larger than the widths of the CDRs) is however very much dependent on the validity of the applied scatter correction. When not correcting for scatter, an overestimation of activity density is found, whereas an overcorrection of scatter leads to an underestimation of activity density^{27,28}.

For the NEMA IEC body phantom used in this work, using an optimized weighting factor k_{TEW} of ≈ 0.67 determined by Monte Carlo modelling of a digital equivalent phantom, the quantitative abilities of TEW scatter correction are comparable to Monte Carlo scatter correction. It has to be emphasized however that in this work the activity density is high, leading to a high number of acquired counts and therefore low image noise. A lower number of counts may lead to increased noise in the scatter window projections and therefore decreased TEW performance⁸. To evaluate this, noise studies should be performed in future work. This study shows that absolute quantitative reconstruction of activity is feasible, with an accuracy at a level which is typically associated with PET³⁰.

The effect of dose calibrator measurement errors on quantification measures should be taken into account when interpreting these results. The relative error in the measurement of the activity concentration can be reduced to around 5%, if sufficient precautions are taken³¹. Consequently, the calculated quantification measures are affected proportionally.

From dual energy windows methods it is known that scatter weighting factors can be object size and background intensity dependent^{32,33}. The implementation of TEW scatter correction for clinical quantitative SPECT remains a challenge, as the quantitative accuracy may depend on the correct estimation of many parameters³⁴. Using the digital anthropomorphic XCAT phantom³⁵ with varying ¹³¹I distributions, k_{TEW} was found (data not shown) to vary considerably, between approximately 0.31 for thyroid uptake to 0.63 for liver uptake. These factors are not the same as found for the phantom measurements presented in this work and are also acquisition angle dependent, indicating that care has to be taken when trying to derive the appropriate weighting

factor experimentally from phantom measurements. This suggests that since there is no single generic k_{TEW} weighting factor, accurate ^{131}I quantification using TEW scatter correction is challenging in clinical practice.

The major obstacle of quantitative ^{131}I SPECT remains the limited resolution inducing a significant partial volume effect. Implementation of a realistic CDR, including all photon physics, has a positive impact on the partial volume effect. Overall, the lowest performance in all measured sphere- and lung insert parameters is observed when CDR is not implemented, followed by a Gaussian CDR estimation and finally modelled CDR. This shows that the accuracy of the used CDRs in the model has a significant impact in quantification of hot- and cold lesions, as well as the accuracy of the lung insert reconstruction. Also, realistic CDR modelling is necessary for intrinsic quantification (i.e., without needing calibration measurements), because the simulations include detector sensitivity. Alternative ways to reduce the partial volume effects include the use of innovative high energy collimators³⁶, and by using partial volume correction methods^{37, 38}.

Conclusion

Monte Carlo-based scatter correction is shown to be intrinsically very accurate in measuring activity concentration over the background VOI of the phantom. The TEW scatter correction method showed significant overestimation of the scatter contribution that could only be compensated by introducing an object dependent scatter weighting factor. Accurate inclusion of the collimator and detector response in reconstruction is the most dominant factor in quantitative reconstructions of small volumes, both hot and cold spheres and the lung insert. Monte Carlo based scatter- and CDR modelling during reconstruction is therefore vital for quantitative ^{131}I SPECT.



References

- 1 R.S. Bahn Chair et al., "Hyperthyroidism and other causes of thyrotoxicosis: management guidelines of the American Thyroid Association and American Association of Clinical Endocrinologists.," *Thyroid* **21**, 593–646 (2011).
- 2 G.K. Gedik, C.A. Hoefnagel, E. Bais, and R.A.V. Olmos, "131I-MIBG therapy in metastatic pheochromocytoma and paraganglioma.," *Eur. J. Nucl. Med. Mol. Imaging* **35**, 725–33 (2008).
- 3 H.J. Brisse et al., "Guidelines for imaging and staging of neuroblastic tumors: consensus report from the International Neuroblastoma Risk Group Project.," *Radiology* **261**, 243–57 (2011).
- 4 Y.K. Dewaraja et al., "MIRD pamphlet no. 23: Quantitative SPECT for patient-specific 3-dimensional dosimetry in internal radionuclide therapy," *J. Nucl. Med.* **53**, 1310–1325 (2012).
- 5 Y.K. Dewaraja et al., "MIRD pamphlet no. 24: Guidelines for quantitative 131I SPECT in dosimetry applications," *J. Nucl. Med.* **54**, 2182–8 (2013).
- 6 Y. Dewaraja and K. Koral, "Quantitative 131I SPECT with triple energy window Compton scatter correction," *IEEE Trans. Nucl. Sci.* **45**, 3109–3114 (1998).
- 7 D.J. Macey et al., "Improved conjugate view quantitation of I-131 by subtraction of scatter and septal penetration events with a triple energy window method.," *Med. Phys.* **22**, 1637–43 (1995).
- 8 Y. Narita et al., "Monte Carlo and experimental evaluation of accuracy and noise properties of two scatter correction methods for SPECT.," *Phys. Med. Biol.* **41**, 2481–96 (1996).
- 9 Y. Du et al., "Evaluation of simultaneous 201Tl/99mTc dual-isotope cardiac SPECT imaging with model-based crosstalk compensation using canine studies.," *J. Nucl. Cardiol.* **21**, 329–40 (2014).
- 10 F. Kalantari, H. Rajabi, and M. Saghari, "Quantification and reduction of the collimator-detector response effect in SPECT by applying a system model during iterative image reconstruction: a simulation study.," *Nucl. Med. Commun.* **33**, 228–38 (2012).
- 11 P.A. Wolf, J.S. Jørgensen, T.G. Schmidt, and E.Y. Sidky, "Few-view single photon emission computed tomography (SPECT) reconstruction based on a blurred piecewise constant object model.," *Phys. Med. Biol.* **58**, 5629–52 (2013).
- 12 H. Zaidi, "Relevance of accurate Monte Carlo modeling in nuclear medical imaging.," *Med. Phys.* **26**, 574–608 (1999).
- 13 M. Elschoot et al., "Quantitative Monte Carlo-based holmium-166 SPECT reconstruction.," *Med. Phys.* **40**, 112502–112512 (2013).
- 14 M. Elschoot, M.G.E.H. Lam, M.A.A.J. van den Bosch, M.A. Viergever, and H.W.A.M. de Jong, "Quantitative Monte Carlo-based 90Y SPECT reconstruction.," *J. Nucl. Med.* **54**, 1557–63 (2013).
- 15 J.B. Moody, Y.K. Dewaraja, and E.P. Ficaro, "Resolution and noise properties of 123I MIBG SPECT with collimator-detector response modeling," in 2011 IEEE Nucl. Sci. Symp. Conf. Rec. (IEEE, 2011), pp. 2779–2786.
- 16 J. Bomanji et al., "Uptake of iodine-123 MIBG by pheochromocytomas, paragangliomas, and neuroblastomas: a histopathological comparison.," *J. Nucl. Med.* **28**, 973–8 (1987).
- 17 J.C. Reynolds, "Percent 131I uptake and post-therapy 131I scans: their role in the management of thyroid cancer.," *Thyroid* **7**, 281–4 (1997).
- 18 J.W. Van Isselt, J.M. de Klerk, H.P. Koppeschaar, and P.P. Van Rijk, "Iodine-131 uptake and turnover rate vary over short intervals in Graves' disease.," *Nucl. Med. Commun.* **21**, 609–16 (2000).

- 19 H.W.A.M. De Jong, T.P. Slijpen, and F.J. Beekman, "Acceleration of Monte Carlo SPECT simulation using convolution-based forced detection," *Nucl. Sci. IEEE Trans.* **48**, 58–64 (2001).
- 20 F.J. Beekman, H.W.A.M. De Jong, and S. Van Geloven, "Efficient fully 3-D iterative SPECT reconstruction with Monte Carlo-based scatter compensation," *IEEE Trans. Med. Imaging* **21**, 867–877 (2002).
- 21 J. Xiao, T.C. de Wit, S.G. Staelens, and F.J. Beekman, "Evaluation of 3D Monte Carlo-based scatter correction for 99mTc cardiac perfusion SPECT," *J. Nucl. Med.* **47**, 1662–9 (2006).
- 22 J. Xiao, T.C. de Wit, W. Zbijewski, S.G. Staelens, and F.J. Beekman, "Evaluation of 3D Monte Carlo-based scatter correction for 201Tl cardiac perfusion SPECT," *J. Nucl. Med.* **48**, 637–44 (2007).
- 23 J.S. Hendricks et al., "MCNPX Extensions version 2.5.0," (2005).
- 24 S.R. Cherry, J.A. Sorenson, and M.E. Phelps, "The Gamma Camera: Performance Characteristics," in *Phys. Nucl. Med.*, third(W.B. Saunders, Philadelphia, 2003), pp. 227–251.
- 25 K. Ogawa, "Simulation study of triple-energy-window scatter correction in combined Tl-201, Tc-99m SPECT," *Ann. Nucl. Med.* **8**, 277–81 (1994).
- 26 K. Ogawa, Y. Harata, T. Ichihara, A. Kubo, and S. Hashimoto, "A practical method for position-dependent Compton-scatter correction in single photon emission CT," *IEEE Trans. Med. Imaging* **10**, 408–12 (1991).
- 27 Y.K. Dewaraja, M. Ljungberg, and J.A. Fessler, "3-D Monte Carlo-Based Scatter Compensation in Quantitative I-131 SPECT Reconstruction," *IEEE Trans. Nucl. Sci.* **53**, 181 (2006).
- 28 N. Song, Y. Du, B. He, and E.C. Frey, "Development and evaluation of a model-based downscatter compensation method for quantitative I-131 SPECT," *Med. Phys.* **38**, 3193–204 (2011).
- 29 T.C. de Wit and F.J. Beekman, "Monte Carlo-based statistical SPECT reconstruction: influence of number of photon tracks," *IEEE Trans. Nucl. Sci.* **52**, 1365–1369 (2005).
- 30 D.L. Bailey and K.P. Willowson, "Quantitative SPECT/CT: SPECT joins PET as a quantitative imaging modality," *Eur. J. Nucl. Med. Mol. Imaging* **41 Suppl 1**, S17–25 (2014).
- 31 J.E. Carey, P. Byrne, L. DeWerd, R. Lieto, and N. Petry, "The selection, use, calibration, and quality assurance of radionuclide calibrators used in nuclear medicine (2012).
- 32 K.F. Koral, F.M. Swailen, S. Buchbinder, N.H. Clinthorne, W.L. Rogers, and B.M. Tsui, "SPECT dual-energy-window Compton correction: scatter multiplier required for quantification," *J. Nucl. Med.* **31**, 90–8 (1990).
- 33 J.Q. Luo, K.F. Koral, M. Ljungberg, C.E. Floyd, and R.J. Jaszczak, "A Monte Carlo investigation of dual-energy-window scatter correction for volume-of-interest quantification in 99Tcm SPECT," *Phys. Med. Biol.* **40**, 181–99 (1995).
- 34 B.J. Min et al., "A simulation study for SPECT multi-pin-hole detector optimization," *IEEE Nucl. Sci. Symp. Conf. Rec.* **4**, 2228–2231 (2005).
- 35 W.P. Segars, G. Sturgeon, S. Mendonca, J. Grimes, and B.M.W. Tsui, "4D XCAT phantom for multimodality imaging research," *Med. Phys.* **37**, 4902–15 (2010).
- 36 C. Beijst, M. Elschot, M.A. Viergever, and H.W.A.M. de Jong, "A parallel-cone collimator for high-energy SPECT," *J. Nucl. Med.* **56**, 476–482 (2015).



- 37 Y.K. Dewaraja, M. Ljungberg, and K.F. Koral, "Monte Carlo evaluation of object shape effects in iodine-131 SPET tumor activity quantification.," *Eur. J. Nucl. Med.* **28**, 900–6 (2001).
- 38 K.F. Koral, A. Yendiki, and Y.K. Dewaraja, "Recovery of total I-131 activity within focal volumes using SPECT and 3D OSEM.," *Phys. Med. Biol.* **52**, 777–90 (2007).



7

**Summary and general
discussion**

Summary

In this thesis several imaging techniques for guidance of radionuclide therapy are investigated. The first part describes the development of instrumentation for guidance of radionuclide therapy. To date, no real-time hybrid imaging modalities for interventional purposes have been developed that combine simultaneously acquired nuclear and anatomic images. Real-time functional imaging in conjunction with anatomical imaging would provide the physician with valuable information during the procedure, thereby improving therapeutic efficiency. **Chapter 2** describes the development of a prototype which relies on placing an x-ray tube, x-ray detector and a gamma camera in one line enabling imaging of the same field of view. Since straightforward combination of these elements would block the line of views, a gamma camera geometry that looks around the x-ray tube was developed. A prototype was built using a mobile c-arm and a gamma camera with a four-pinhole collimator. Using the prototype, test images were acquired and sensitivity, resolution and co-registration error were analyzed. Nuclear images (2 frames per second) were acquired simultaneously with x-ray images. Depending on the point source-to-detector distance, the system resolution was 1.5 – 1.9 cm full width at half maximum (FWHM), the sensitivity $0.6 - 1.5 \times 10^{-5}$ counts per decay and the co-registration error -0.13 – 0.15 cm. With good spatial and temporal alignment of both modalities throughout the field of view, x-ray images can be shown in grayscale and corresponding nuclear images in color overlay. Measurements with our hybrid imaging prototype device that combines simultaneous x-ray and nuclear imaging of the same field of view have demonstrated the feasibility of real time simultaneous hybrid imaging in the intervention room.

Accurate determination of the system parameters that describe the position of the x-ray tube, x-ray detector, gamma camera and collimators is crucial to optimize image quality. **Chapter 3** discusses a calibration method that estimates the system parameters used for reconstruction. A multimodality phantom consisting of five point sources was created. First, nuclear and fluoroscopic images of the phantom were acquired at several distances from the image intensifier. The system parameters were acquired using physical measurement and multimodality images of the phantom were reconstructed. The resolution and co-registration error of the point sources were determined as a measure of image quality. Next, the system parameters were estimated using a calibration method, which adjusted the parameters in the reconstruction algorithm, until the resolution and co-registration were optimized. For evaluation, multimodality images of a second set of phantom acquisitions were reconstructed using calibrated parameter sets. Subsequently, the resolution and co-registration error of the point sources were determined as a measure of image quality. In addition, simultaneously acquired fluoroscopic and nuclear images of two moving syringes were obtained with parameter sets from before and after calibration. The mean FWHM was lower after calibration (0.94 cm) than before calibration (1.01 cm). The mean co-registration error was lower after calibration (0.14 cm) than before calibration (1.17 cm). The simultaneously acquired fluoroscopic and nuclear images showed improved co-registration after calibration as compared with before calibration. A calibration method was presented that improves the resolution and co-registration of simultaneously acquired hybrid fluoroscopic and nuclear images by estimating the geometric parameter set as compared with a parameter set acquired by direct physical measurement.

The second part of this thesis concerns the quality of single photon emission computed tomography (SPECT) images of high-energy photon-emitting isotopes. Potential methods to improve the quality of high-energy SPECT images are introduced, and the implications of reduced image quality in clinical practice are discussed.

In SPECT using high-energy photon emitting isotopes, such as ^{131}I , parallel hole collimators with thick septa are required to limit septal penetration at the cost of sensitivity and resolution. **Chapter 4** investigates a collimator with cone-shaped holes, which is designed to limit collimator penetration while preserving resolution and sensitivity. The objective is to demonstrate that a single slice prototype of the parallel cone (PC) collimator is capable of improving the image quality of high-energy SPECT. The image quality of the PC collimator was quantitatively compared to that of clinically used low-energy high-resolution (LEHR; for $^{99\text{m}}\text{Tc}$) and high-energy general-purpose (HEGP; for ^{131}I and ^{18}F) parallel hole collimators. First, Monte Carlo simulations of single and double point sources were performed to assess sensitivity and resolution by comparing point spread functions (PSFs). Second, a prototype PC collimator was used in an experimental phantom study to assess and compare contrast recovery coefficients and image noise. Monte Carlo simulations showed reduced broadening of the PSF due to collimator penetration for the PC collimator as compared with the HEGP collimator (e.g. 0.9 cm vs. 1.4 cm FWHM for ^{131}I). Simulated double point sources placed 2 cm apart were separately detectable for the PC collimator, whereas this was not the case for ^{131}I and ^{18}F at distances from the collimator face ≥ 10 cm for the HEGP collimator. The sensitivity, measured over the simulated profiles as the total amount of counts per decay, was found to be higher for the LEHR and HEGP collimators than for the PC collimator (e.g. 3.1×10^{-5} vs. 2.9×10^{-5} counts per decay for ^{131}I). However, at equal noise level, phantom measurements showed that contrast recovery coefficients were similar for the PC and LEHR collimators for $^{99\text{m}}\text{Tc}$, but that the PC collimator significantly improved the contrast recovery coefficients as compared with the HEGP collimator for ^{131}I and ^{18}F . High-energy SPECT imaging with a single slice prototype of the proposed PC collimator has shown the potential for significantly improved image quality in comparison with standard parallel hole collimators.

Radioiodine therapy with ^{131}I is used for treatment of suspected recurrence of differentiated thyroid carcinoma. Pretherapeutic ^{124}I PET/CT with a low activity ($\sim 1\%$ of ^{131}I activity) can be performed to determine whether uptake of ^{131}I , and thereby the desired therapeutic effect, may be expected. However, false-negative ^{124}I PET/CT results as compared with posttherapeutic ^{131}I SPECT/CT have been reported by several groups¹⁻⁵. The purpose of **Chapter 5** was to investigate whether the reported discrepancies may be ascribed to a difference in lesion detectability between ^{124}I PET/CT and ^{131}I SPECT/CT and, hence, whether the administered ^{124}I activity is sufficient to achieve equal detectability. Phantom measurements were performed using the National Electrical Manufacturers Association 2007 image-quality phantom. As a measure of detectability, the contrast-to-noise ratio was calculated. The ^{124}I activity was expressed as the percentage of ^{131}I activity required to achieve the same contrast-to-noise ratio. This metric was defined as the detectability equivalence percentage (DEP). As lower DEPs were obtained for smaller spheres, a relatively low ^{124}I activity was sufficient to achieve similar lesion detectability between ^{124}I PET/CT and ^{131}I SPECT/CT. DEP was 1.5%, 1.9%, 1.9%, 4.4%, 9.0%, and 16.2% for spheres with diameters of 10, 13, 17, 18, 25, and 37 mm, respectively, for attenuation- and scatter-corrected SPECT versus

point-spread function (PSF) model-based and time-of-flight (TOF) PET. For no-PSF no-TOF PET, DEP was 3.6%, 2.1%, 3.5%, 7.8%, 15.1%, and 23.3%, respectively. In conclusion, a relatively low ^{124}I activity of 74 MBq (~1% of ^{131}I activity) is sufficient to achieve similar lesion detectability between ^{124}I PSF TOF PET/CT and ^{131}I SPECT/CT for small spheres (≤ 10 mm), since the reported DEPs are close to 1%. False-negative ^{124}I PET/CT results as compared with posttherapeutic ^{131}I SPECT/CT may be ascribed to differences in detectability for large lesions (> 10 mm) and for no-PSF no-TOF PET, since DEPs are greater than 1%. On the basis of DEPs of 3.5% for lesion diameters of up to 17 mm on no-PSF no-TOF PET, ^{124}I activities as high as 170 MBq may be warranted to obtain equal detectability.

Dosimetry for treatment monitoring requires quantitative SPECT images. However, quantitative SPECT imaging of high-energy isotopes such as ^{131}I remains a challenge, because of scatter and collimator penetration. The quality of SPECT images can be improved upon by incorporating scatter and collimator-detector-response models in the reconstruction. **Chapter 6** compares triple-energy-window (TEW) and Monte Carlo based scatter correction methods, as well as different methods for collimator-detector response (CDR) by performing phantom measurements. A SPECT/CT acquisition of the NEMA IEC body phantom was performed. Subsequently, images were reconstructed using the following parameters: 1) without scatter correction, 2) with TEW scatter correction and 3) with Monte Carlo-based scatter correction. For modelling the CDR, both a) geometric Gaussian CDRs as well as b) Monte Carlo simulated CDRs were compared. In the resulting reconstructions, quantitative accuracy, contrast-to-noise ratios and recovery coefficients were calculated, as well as the percentage of background variability and the residual count error in the lung insert. The quantification error as compared with a dose calibrator derived measurement was found to be $< 1\%$, -26% and 33% for the Monte Carlo scatter corrected, TEW scatter corrected and no scatter corrected reconstruction method, respectively. Higher recovery coefficients were obtained with the Monte Carlo simulated CDR correction than with the geometric CDR and no CDR modelling. The contrast recovery of the TEW method was similar to the Monte Carlo method. However, the TEW method required an experimentally determined weighting factor. The reconstruction method incorporating Monte Carlo based scatter correction and simulated CDR modelling produced intrinsically quantitative ^{131}I SPECT images with contrast recovery coefficient similar to the TEW scatter correction method, without the use of experimentally determined weighting factors.

General Discussion

Part I

Measurements described in the first part of this thesis with the prototype setup of the hybrid c-arm demonstrate that real-time simultaneous fluoroscopic and nuclear imaging of the same field of view is feasible. This was achieved without adding constraints to the traditional geometry of the C-arm and to the interventional set-up. The fluoroscopic and nuclear hybrid images demonstrated good spatial and temporal overlap.

The purpose of the hybrid c-arm is not to compete with diagnostic hybrid imaging devices in terms of image parameters such as resolution and contrast. The proposed system is rather aimed at guiding interventional oncological procedures. The intrinsic spatial co-registration of the x-ray and nuclear images is a great advantage in supporting the dynamic procedures in the intervention room.

Limitations simultaneous fluoroscopic and nuclear imaging

Constructing a real prototype can prove the technical feasibility of a system, but it may also reveal unforeseen obstacles. Prototype measurements showed substantial spill-over of x-rays into the nuclear images, even at kV settings well below the lower energy threshold of the nuclear imaging (126 keV). Pile-up effects in the gamma camera can cause multiple x-ray photons to be detected as a single gamma photon, potentially causing x-ray photons to be counted in the energy window. Possible solutions to the spill-over problem include anti-synchronization of the nuclear acquisition with pulsed fluoroscopy⁶. Assuming that x-ray images are acquired with a frequency of 5 frames per second and a pulse width of 5 ms, only 2.5% of the counts would theoretically be lost to prevent detection of possibly scattered x-rays in the gamma camera energy window. Furthermore, the effects of x-ray photon pileup can be overcome by using detectors with a higher temporal resolution than detectors equipped with a NaI(Tl) scintillation crystal, such as a LSO or LaBr₃ scintillation crystal with a much shorter decay time^{7,8}.

In the prototype set-up using a standard desktop computer and software not optimized for speed, the average post-processing time for a single visualization frame was approximately 3 s, allowing only retrospective image evaluation. Several groups have shown that significant acceleration can be achieved by parallel processing on graphic processing units (GPUs)⁹. Therefore, we believe real time processing is feasible when optimized hardware and software is used.

Future perspectives simultaneous fluoroscopic and nuclear imaging

Future research will be aimed at improving the image quality while maintaining the system's capability of simultaneous hybrid imaging. Larger digital flat panel x-ray detectors capable of imaging the entire patient may be more practical for clinical procedures than the relatively small image intensifier used for the prototype. Additionally, problems caused by distortion of image intensifiers will be overcome, since these problems are almost non-existent for digital flat panel detectors.

The application of smaller detectors for nuclear imaging and/or of other collimators such as parallel hole collimators may improve sensitivity, resolution and allow a flexible light-weight

design. The resolution and the sensitivity are also affected by the reconstruction method that is used and the reconstruction parameters, such as the number of iterations. Nevertheless, the optimization of image quality remains a visual trade-off between resolution and noise, as with all nuclear medicine examinations in clinical practice. For some tasks high resolution is required, whereas images with low noise levels may be favored for other applications. More research needs to be done to determine optimal geometry and reconstruction parameters for the fluoroscopic and nuclear imaging c-arm. The same holds for the frame rate of nuclear imaging. Guidance of interventional procedures may require high frame rates, whereas diagnostic imaging may require high image quality. The noise level of the acquired images will also depend on the amount of activity that is used, which in turn depends on the isotope and the procedure. Clinical experience will be required to optimize these parameters and is subject of future research.

The presented experimental setup was only able to perform acquisitions in a single orientation. Future research aims to develop a prototype that can rotate around the patient, the same way conventional c-arms are used. By acquiring multiple projections during the rotation of the hybrid c-arm around the patient, it is also possible to perform tomography, the same way c-arms can be used to perform cone beam CT¹⁰⁻¹². Effectively, this would enable the acquisition of interventional simultaneous SPECT/CT studies. Tomography instead of planar imaging may provide additional useful information for image guided (oncological) interventions.

Simultaneous fluoroscopic and nuclear imaging for radioembolization

Simultaneous fluoroscopic and nuclear imaging can potentially be used for assessment of the activity distribution of the scout dose and therapeutic dose during radioembolization procedures. More specifically, the hybrid c-arm may be used for assessment of lung shunt, extra-hepatic depositions, and possibly even the intra-hepatic distribution, depending on the quality of the images that can be obtained with the future prototype. The advantage of using the hybrid c-arm for imaging during radioembolization procedures is that the images can be acquired in the intervention room during the procedure instead of after the procedure using a SPECT/CT or PET/CT. The radioembolization procedure is currently performed in two steps, because the patient needs to leave the intervention room for imaging of the scout dose. However, when the assessment of the scout dose distribution can be evaluated in the intervention room, the radioembolization procedure may be performed in one step. In general, the therapeutic efficiency of procedures may be greatly improved by use of a modality for simultaneous fluoroscopic and nuclear imaging.

Alternatives interventional imaging

Hand held gamma cameras and gamma probes can be used to acquire intra-operative information about the distribution of activity¹³⁻¹⁵. In addition, hand held cameras can also be used for interventional freehand SPECT, by reconstructing three-dimensional datasets from the acquired projection data¹⁶⁻¹⁸. These freehand SPECT images can be fused with ultrasound images for hybrid image guidance¹⁹. Another approach to interventional nuclear imaging is to mount a gamma camera on a robotic arm for interventional robotic SPECT²⁰. However, the interpretation of this information may be difficult owing to the lack of co-registered anatomical information. This can be solved by registration of pre-operative anatomical data to the interventionally acquired

images²¹. Nevertheless, non-rigid registration remains a challenge and the preoperative images may not represent the actual activity distribution. Other ways of hybrid image guidance include the use of hybrid gamma-emitting and fluorescent tracers for sentinel lymph node procedures that enable two-step navigation by preoperative imaging with SPECT/CT and intraoperative guidance by near-infrared fluorescence imaging²².

Part II

For assessment of treatment response, dosimetry and treatment planning in radionuclide therapies, diagnostic hybrid systems (i.e. SPECT/CTs and PET/CTs) are widely used. As a consequence, an improvement of image quality will benefit radionuclide therapies.

General-purpose collimator?

There are many ways of improving the quality of images used for guidance of radionuclide therapy. Chapter 4 highlights the potential of significantly improved image quality with a single slice prototype of the proposed parallel cone (PC) collimator in comparison with standard parallel hole collimators, by reducing collimator penetration. Many of the isotopes used for radionuclide therapies (e.g. ¹³¹I and ⁹⁰Y) emit high energy photons that easily penetrate the collimator. Therefore, the image quality of the proposed PC collimator decreases as the photon energy increases. However, the loss of image quality is not as severe for the PC collimator as observed for the parallel hole collimator. This suggests that the PC collimator could be used for a variety of radioisotopes and photon energies. Using a single collimator for multiple purposes has many benefits in clinical practice, because changing collimators between exams is time consuming and requires large and heavy collimator carts. A study comparing acquisitions from full-FOV collimators with full three-dimensional acquisitions and algorithms may give conclusive answers as to whether the PC collimator can improve image quality in clinical practice.

Dedicated systems

Most commercial diagnostic hybrid systems are designed to perform a large variety of exams. However, systems can also be designed for a specific purpose.

In addition to optimizing the collimator for high-energy purposes as described in Chapter 4, the detector can also be optimized for high-energy photons. This can be done by employing scintillation crystals with high stopping power, which increases the detection efficiency. Walrand et al. have designed a camera dedicated for Bremsstrahlung imaging of ⁹⁰Y^{23, 24}. They describe a dedicated system with a 30 mm thick BGO crystal and a 8 mm high-energy pinhole with extra shielding to prevent penetration of high-energy photons. Additionally, it is suggested that the camera is mounted on a simplified mobile gantry for use in the intervention room.

Dedicated instrumentation designed for a single application can improve image as compared with general-purpose instrumentation. Myocardial perfusion imaging is an interesting application for dedicated systems, since a large part of the SPECT studies in clinical practice are cardiac studies. The Siemens IQSPECT method with the smartzoom collimator is especially designed for myocardial perfusion imaging^{25, 26}. The rationale behind the collimator is that it is partially converging so that a magnification of the heart is obtained. Entirely dedicated cardiac SPECT systems have also been developed, that are often smaller than standard SPECT/CT systems and employ ingenious

collimator designs²⁷⁻³². Dedicated systems have shown the feasibility of significantly reduced acquisition times or radiation dose while remaining high image quality, which benefits patient comfort and scanning efficiency.

Advances in image reconstruction

In addition to optimizing the instrumentation for high-energy applications, the reconstruction algorithm can also be optimized. This can be achieved by modelling the image degrading effects accurately. Chapter 6 discusses various models that correct for the adverse effects of scatter and collimator detector response on image quality. Other advances in emission tomography reconstruction include modelling of cardiac and/or respiratory motion and dynamic imaging by incorporating the information of motion into the reconstruction algorithm³³⁻³⁷. Especially for four-dimensional reconstruction algorithms, it is preferred to preserve temporal information of the counts so that list-mode data is often used instead of binned sinograms. Other advances include the integration of anatomical information in the reconstruction algorithm by using anatomical priors^{38,39}. Owing to the advances in the field of PET/MR, algorithms that reconstruct the activity and the attenuation simultaneously have been developed, because obtaining mu-maps from MR images remains a challenge⁴⁰⁻⁴². Note that many groups focus their research on implementation of these techniques in PET, although translation to SPECT may be feasible for many techniques.

PET versus SPECT

Generally, PET outperforms SPECT in the sense of sensitivity, resolution and quantitative capabilities. An approach to improve the quality of nuclear images, is to replace SPECT tracers with positron emitting PET tracers. For example in myocardial perfusion imaging, several positron emitting tracers have been suggested as alternative to ^{99m}Tc sestamibi⁴³⁻⁴⁵. However, the short half-lives of ⁸²Rb, ¹⁵O and ¹³N render these isotopes impractical for clinical use and require the presence of an on-site cyclotron or generator. Fluorinated (¹⁸F) PET tracers are therefore practical, owing to the half-life of 109 minutes and the presence of an existing infrastructure for production and distribution. Successful results have recently been obtained with Flurpiridaz ¹⁸F PET for assessment of myocardial blood flow⁴⁵⁻⁴⁷. These advances spur the question of whether there is a future for SPECT systems in the nuclear medicine department⁴⁸⁻⁵⁰. Some have argued that PET may completely replace scintigraphy and SPECT in the future⁴⁹. However, the success of a modality depends for a large part on cost-effectiveness. In many cases, SPECT remains the preferred modality because ^{99m}Tc is produced easily using a generator, and many SPECT tracers can be in-house prepared by kit formulation.

Conclusions

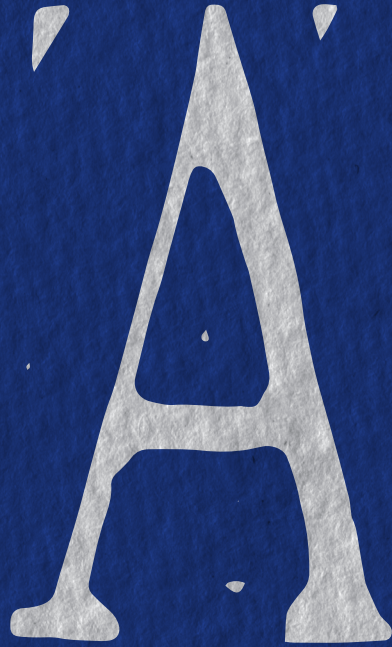
- Measurements with our hybrid imaging prototype device have shown that simultaneous fluoroscopic and nuclear imaging of the same field of view is feasible.
- A calibration method can be used to improve the resolution and co-registration of simultaneously acquired hybrid fluoroscopic and nuclear images by estimating the geometric parameter set as compared with a parameter set acquired by direct physical measurement.
- High-energy SPECT imaging with a single slice prototype of the proposed PC collimator has shown the potential for significantly improved image quality in comparison with standard parallel hole collimators.
- A relatively low ^{124}I activity of 74 MBq (~1% of ^{131}I activity) is sufficient to achieve similar lesion detectability between ^{124}I PSF TOF PET/CT and ^{131}I SPECT/CT for small spheres (≤ 10 mm). False-negative ^{124}I PET/CT results as compared with posttherapeutic ^{131}I SPECT/CT may be ascribed to differences in detectability for large lesions (> 10 mm) and for no-PSF no-TOF PET.
- The reconstruction method incorporating Monte Carlo based scatter correction and simulated CDR modelling produced intrinsically quantitative ^{131}I SPECT images with contrast recovery coefficient similar to the TEW scatter correction method, without the use of experimentally determined weighting factors.

References

- 1 C. De Pont, S. Halders, J. Bucierius, F. Mottaghy, and B. Brans, "124I PET/CT in the pretherapeutic staging of differentiated thyroid carcinoma: Comparison with posttherapy 131I SPECT/CT," *Eur. J. Nucl. Med. Mol. Imaging* 40, 693–700 (2013).
- 2 L.S. Freudenberg, W. Jentzen, S.P. Müller, and A. Bockisch, "Disseminated iodine-avid lung metastases in differentiated thyroid cancer: A challenge to 124I PET," *Eur. J. Nucl. Med. Mol. Imaging* 35, 502–508 (2008).
- 3 G.R. Khorjekar et al., "Do negative 124I pretherapy positron emission tomography scans in patients with elevated serum thyroglobulin levels predict negative 131I posttherapy scans?," *Thyroid* 24, 1394–1399 (2014).
- 4 G. K. Lammers, J.P. Esser, P.C.M. Pasker, M.E. Sanson-van Praag, and J.M.H. de Klerk, "Can I-124 PET/CT predict pathological uptake of therapeutic dosages of radioiodine (I-131) in differentiated thyroid carcinoma?," *Adv. Mol. Imaging* 04, 27–34 (2014).
- 5 H.T.T. Phan et al., "The diagnostic value of 124I-PET in patients with differentiated thyroid cancer," *Eur. J. Nucl. Med. Mol. Imaging* 35, 958–965 (2008).
- 6 D.B. Plewes and E. Vogelstein, "Grid controlled x-ray tube switching time: implications for rapid exposure control," *Med. Phys.* 11, 693–696 (1984).
- 7 T.K. Lewellen, "Recent developments in PET detector technology," *Phys. Med. Biol.* 53, R287–R317 (2008).
- 8 T.E. Peterson and L.R. Furenlid, "SPECT detectors: the Anger camera and beyond," *Phys. Med. Biol.* 56, R145–R182 (2011).
- 9 A. Eklund, P. Dufort, D. Forsberg, and S.M. LaConte, "Medical image processing on the GPU - Past, present and future," *Med. Image Anal.* 17, 1073–1094 (2013).
- 10 J.H. Siewerdsen et al., "Volume CT with a flat-panel detector on a mobile, isocentric C-arm: pre-clinical investigation in guidance of minimally invasive surgery," *Med. Phys.* 32, 241–254 (2005).
- 11 U. Linsenmaier et al., "Three-dimensional CT with a modified C-arm image intensifier: feasibility," *Radiology* 224, 286–92 (2002).
- 12 M.J. Wallace et al., "Impact of C-arm CT on Hepatic Arterial Interventions for Hepatic Malignancies," *J. Vasc. Interv. Radiol.* 18, 1500–1507 (2007).
- 13 S. Schneebaum et al., "Clinical applications of gamma-detection probes - Radioguided surgery," *Eur. J. Nucl. Med.* 26, 26–35 (1999).
- 14 E.J. Hoffman, M.P. Tornai, C.S. Levin, L.R. MacDonald, and S. Siegel, "Gamma and beta intra-operative imaging probes," *Nucl. Instruments Methods Phys. Res. Sect. A Accel. Spectrometers, Detect. Assoc. Equip.* 392, 324–329 (1997).
- 15 S. Heller and P. Zanzonico, "Nuclear probes and intraoperative gamma cameras," *Semin. Nucl. Med.* 41, 166–181 (2011).
- 16 C. Bluemel et al., "Freehand SPECT for image-guided sentinel lymph node biopsy in breast cancer," *Eur. J. Nucl. Med. Mol. Imaging* 40, 1656–61 (2013).
- 17 R. de Bree, B. Pouw, D.A. Heuveling, and J.A. Castelijns, "Fusion of Freehand SPECT and Ultrasound to Perform Ultrasound-Guided Fine-Needle Aspiration Cytology of Sentinel Nodes in Head and Neck Cancer," *AJNR. Am. J. Neuroradiol.* 36, 2153–8 (2015).
- 18 D.A. Heuveling, S. van Weert, K.H. Karagozoglu, and R. de Bree, "Evaluation of the use of freehand SPECT for sentinel node biopsy in early stage oral carcinoma," *Oral Oncol.* 51, 287–90 (2015).

- 19 M. Freesmeyer, T. Opfermann, and T. Winkens, "Hybrid integration of real-time US and freehand SPECT: proof of concept in patients with thyroid diseases.," *Radiology* 271, 856–61 (2014).
- 20 B. Fuerst et al., "First Robotic SPECT for Minimally Invasive Sentinel Lymph Node Mapping.," *IEEE Trans. Med. Imaging* PP, 1 (2015).
- 21 B.J. Wood et al., "Technologies for guidance of radiofrequency ablation in the multimodality interventional suite of the future.," *J. Vasc. Interv. Radiol.* 18, 9–24 (2007).
- 22 N.S. van den Berg, R.A. Valdés-Olmos, H.G. van der Poel, and F.W.B. van Leeuwen, "Sentinel lymph node biopsy for prostate cancer: a hybrid approach.," *J. Nucl. Med.* 54, 493–6 (2013).
- 23 S. Walrand, M. Hesse, R. Wojcik, R. Lhommel, and F. Jamar, "Optimal design of anger camera for bremsstrahlung imaging: Monte Carlo evaluation.," *Front. Oncol.* 4, 149 (2014).
- 24 S. Walrand, M. Hesse, G. Demonceau, S. Pauwels, and F. Jamar, "Yttrium-90-labeled microsphere tracking during liver selective internal radiotherapy by bremsstrahlung pinhole SPECT: feasibility study and evaluation in an abdominal phantom.," *EJNMMI Res.* 1, 32 (2011).
- 25 P.C. Hawman and E.J. Haines, "The Cardiofocal collimator: a variable-focus collimator for cardiac SPECT," *Phys. Med. Biol.* 39, 439–450 (1994).
- 26 R. Rajaram et al., "Tomographic performance characteristics of the IQ-SPECT system," in 2011 IEEE Nucl. Sci. Symp. Conf. Rec.(IEEE, 2011), pp. 2451–2456.
- 27 F.P. Esteves et al., "Novel solid-state-detector dedicated cardiac camera for fast myocardial perfusion imaging: multicenter comparison with standard dual detector cameras.," *J. Nucl. Cardiol.* 16, 927–34.
- 28 E. V Garcia, T.L. Faber, and F.P. Esteves, "Cardiac dedicated ultrafast SPECT cameras: new designs and clinical implications.," *J. Nucl. Med.* 52, 210–7 (2011).
- 29 T. Sharir et al., "Multicenter Trial of High-Speed Versus Conventional Single-Photon Emission Computed Tomography Imaging," *J. Am. Coll. Cardiol.* 55, 1965–1974 (2010).
- 30 T. Sharir, P.J. Slomka, and D.S. Berman, "Solid-state SPECT technology: fast and furious.," *J. Nucl. Cardiol.* 17, 890–6 (2010).
- 31 J. Maddahi et al., "Prospective multicenter evaluation of rapid, gated SPECT myocardial perfusion upright imaging.," *J. Nucl. Cardiol.* 16, 351–7.
- 32 W.L. Duvall et al., "Reduced isotope dose and imaging time with a high-efficiency CZT SPECT camera.," *J. Nucl. Cardiol.* 18, 847–857 (2011).
- 33 A. Rahmim, O. Rousset, and H. Zaidi, "Strategies for Motion Tracking and Correction in PET," *PET Clin.* 2, 251–266 (2007).
- 34 A.J. Reader and J. Verhaeghe, "4D image reconstruction for emission tomography.," *Phys. Med. Biol.* 59, R371–418 (2014).
- 35 G. Li et al., "Advances in 4D medical imaging and 4D radiation therapy.," *Technol. Cancer Res. Treat.* 7, 67–81 (2008).
- 36 U.M. Shrestha, Y. Seo, E.H. Botvinick, and G.T. Gullberg, "Image reconstruction in higher dimensions: myocardial perfusion imaging of tracer dynamics with cardiac motion due to deformation and respiration.," *Phys. Med. Biol.* 60, 8275–301 (2015).
- 37 A. Rahmim, J. Tang, and H. Zaidi, "Four-dimensional (4D) image reconstruction strategies in dynamic PET: Beyond conventional independent frame reconstruction," *Med. Phys.* 36, 3654 (2009).

- 38 J. Cheng-Liao and J. Qi, "PET image reconstruction with anatomical edge guided level set prior.," *Phys. Med. Biol.* 56, 6899–918 (2011).
- 39 S. Somayajula, C. Panagiotou, A. Rangarajan, Q. Li, S.R. Arridge, and R.M. Leahy, "PET image reconstruction using information theoretic anatomical priors.," *IEEE Trans. Med. Imaging* 30, 537–49 (2011).
- 40 A. Rezaei, M. Defrise, and J. Nuyts, "ML-reconstruction for TOF-PET with simultaneous estimation of the attenuation factors.," *IEEE Trans. Med. Imaging* 33, 1563–72 (2014).
- 41 M. Defrise, A. Rezaei, and J. Nuyts, "Time-of-flight PET data determine the attenuation sinogram up to a constant.," *Phys. Med. Biol.* 57, 885–99 (2012).
- 42 A. Rezaei et al., "Simultaneous reconstruction of activity and attenuation in time-of-flight PET.," *IEEE Trans. Med. Imaging* 31, 2224–33 (2012).
- 43 T.H. Schindler, "Positron-emitting myocardial blood flow tracers and clinical potential.," *Prog. Cardiovasc. Dis.* 57, 588–606 (2015).
- 44 J. Maddahi and R.R.S. Packard, "Cardiac PET perfusion tracers: current status and future directions.," *Semin. Nucl. Med.* 44, 333–43 (2014).
- 45 D.S. Berman et al., "Phase II safety and clinical comparison with single-photon emission computed tomography myocardial perfusion imaging for detection of coronary artery disease: flurpiridaz F 18 positron emission tomography.," *J. Am. Coll. Cardiol.* 61, 469–77 (2013).
- 46 R.R.S. Packard, S.-C. Huang, M. Dahlbom, J. Czernin, and J. Maddahi, "Absolute quantitation of myocardial blood flow in human subjects with or without myocardial ischemia using dynamic flurpiridaz F 18 PET.," *J. Nucl. Med.* 55, 1438–44 (2014).
- 47 P.J. Slomka et al., "Dual-gated motion-frozen cardiac PET with Flurpiridaz F18.," *J. Nucl. Med.* (2015).
- 48 A. Gholamrezanejad, S. Mirpour, and G. Mariani, "Future of nuclear medicine: SPECT versus PET.," *J. Nucl. Med.* 50, 16N–18N (2009).
- 49 A. Alavi and S. Basu, "Planar and SPECT imaging in the era of PET and PET-CT: can it survive the test of time?," *Eur. J. Nucl. Med. Mol. Imaging* 35, 1554–9 (2008).
- 50 G. Mariani, L. Bruselli, and A. Duatti, "Is PET always an advantage versus planar and SPECT imaging?," *Eur. J. Nucl. Med. Mol. Imaging* 35, 1560–5 (2008).



Addenda

Samenvatting in het Nederlands

In dit proefschrift worden verscheidene technieken besproken voor geleiding van radionuclidetherapie. Het eerste deel beschrijft de ontwikkeling van apparatuur voor geleiding van radionuclidetherapie.

Tot op heden zijn er geen hybride beeldvormende modaliteiten bekend die simultane nucleaire en anatomische beeldvorming kunnen combineren. Functionele beelden tegelijkertijd verkregen met anatomische beelden zouden de arts kunnen voorzien van waardevolle informatie tijdens (oncologische) interventies. Hierdoor zou de efficiëntie van de behandeling verbeterd kunnen worden. **Hoofdstuk 2** beschrijft de ontwikkeling van een prototype waarin een röntgenbuis, een röntgendetector en een gamma camera op één lijn geplaatst zijn, om hybride beeldvorming van hetzelfde volume mogelijk te maken. Triviale geometrische combinaties van deze elementen zouden ervoor zorgen dat het beeld geblokkeerd wordt. Daarom is er een innovatieve gamma camera geometrie bedacht. Het prototype is gebouwd met een mobiele c-boog, een gamma camera en een collimator bestaande uit vier pinholes. Met dit prototype werden testbeelden opgenomen om de sensitiviteit, de resolutie en de co-registratie te bepalen. Nucleaire beelden (2 beelden per seconde) werden tegelijkertijd met de fluoroscopische beelden opgenomen. Afhankelijk van de afstand tussen de puntbron en de detector, was de resolutie 1.5 – 1.9 cm full width at half maximum (FWHM), de sensitiviteit 0.6 – 1.5×10^{-5} tellen per verval, en de co-registratie fout -0.13 – 0.15 cm. Met een goede spatiële en temporele uitlijning van beide modaliteiten in het hele volume, kunnen fluoroscopische beelden in grijstinten en nucleaire beelden in kleurschaal over elkaar worden weergegeven. Metingen met het hybride prototype voor simultane fluoroscopische en nucleaire beeldvorming van hetzelfde volume, hebben laten zien dat simultane hybride beeldvorming in de interventiekamer mogelijk is.

Het is cruciaal voor de optimalisatie van de beeldkwaliteit dat de systeemparemeters nauwkeurig worden bepaald, die de positie van de röntgenbuis, röntgendetector en gamma camera beschrijven. **Hoofdstuk 3** beschrijft een kalibratiemethode die de systeemparemeters voor reconstructie bepaalt. Hiervoor hebben wij een multimodaal fantoom gebruikt bestaande uit vijf puntbronnen. Allereerst zijn nucleaire en fluoroscopische beelden opgenomen van het fantoom dat op verschillende afstanden van de röntgendetector werd geplaatst. De systeemparemeters zijn bepaald door deze fysiek te meten, en multimodale beelden werden gereconstrueerd. De resolutie en co-registratie fout van de puntbronnen konden hierdoor worden berekend als maat voor de beeldkwaliteit. Vervolgens werden de systeemparemeters afgeschat met behulp van een kalibratiemethode. Deze methode paste de systeemparemeters voor reconstructie aan totdat de optimale resolutie en co-registratie was bereikt. Ter evaluatie zijn multimodale beelden gereconstrueerd van een tweede set metingen met gekalibreerde parameters. Daarna werd de resolutie en co-registratiefout van de puntbronnen berekend als maat voor de beeldkwaliteit. Ten slotte werden simultane fluoroscopische en nucleaire beelden opgenomen van twee bewegende spuiten met systeemparemeters van voor en na kalibratie. De gemiddelde FWHM was lager na kalibratie (0.94 cm) dan voor kalibratie (1.01 cm). De gemiddelde co-registratie fout bleek lager te zijn na kalibratie (0.14 cm) dan voor kalibratie (1.17 cm). De simultaan verkregen fluoroscopische en nucleaire beelden vertoonden een verbeterde co-registratie na kalibratie, in vergelijking met voor de kalibratie. Uiteindelijk is een kalibratiemethode gepresenteerd die de resolutie en co-

registratie van simultaan verkregen fluoroscopische en nucleaire beelden verbeterde door de systeemparameters te kalibreren.

Het tweede deel van dit proefschrift gaat over de kwaliteit van 'single photon emission computed tomography' (SPECT) beelden van isotopen die hoogenergetische fotonen uitzenden. Mogelijke methoden ter verbetering van de beeldkwaliteit van hoogenergetische SPECT beelden komen aan de orde, en de gevolgen van een verslechterde beeldkwaliteit in de klinische praktijk worden besproken.

'Parallel hole' collimatoren met dikke septa zijn vereist voor het verkrijgen van SPECT beelden van isotopen, zoals ^{131}I , die hoogenergetische fotonen uitzenden. Deze dikke septa zorgen ervoor dat de penetratie van de septa beperkt blijft hoewel dat ten koste gaat van de sensitiviteit en de resolutie. **Hoofdstuk 4** beschrijft een collimator met kegelvormige gaten. Deze zijn zo ontworpen dat de collimator-penetratie beperkt blijft terwijl de resolutie en sensitiviteit behouden blijven. Het doel van deze studie was om te laten zien dat een prototype bestaande uit een enkelvoudige rij van parallelle kegelvormige gaten (de parallel cone (PC) collimator) in staat is om de beeldkwaliteit van hoogenergetische SPECT beelden te verbeteren. De beeldkwaliteit van de PC collimator werd kwantitatief vergeleken met de klinisch gebruikte 'low-energy high-resolution' (LEHR; voor $^{99\text{m}}\text{Tc}$) en 'high-energy general-purpose' (HEGP; voor ^{131}I en ^{18}F) parallel hole collimatoren. Ten eerste werden Monte Carlo simulaties uitgevoerd van enkele en dubbele puntbronnen om de sensitiviteit en de resolutie te bestuderen. Hiertoe werden punt-spreid-functies (point spread functions (PSFs)) vergeleken. Ten tweede werd de PC collimator gebruikt voor een fantoom studie. De fantoommetingen hadden als doel de contrast herstel coëfficiënten (contrast recovery coefficients (CRCs)) en de beeldruis te vergelijken. De Monte Carlo simulaties lieten een verminderde verbreding van de PSFs zien als gevolg van collimator penetratie voor de PC collimator in vergelijking met de HEGP collimator (e.g. 0.9 cm vs. 1.4 cm FWHM voor ^{131}I). De gesimuleerde dubbele puntbronnen, met 2 cm onderlinge afstand, waren onderscheidbaar voor de PC collimator. Dit was niet het geval was voor ^{131}I en ^{18}F op afstanden van het collimator oppervlak ≥ 10 cm voor de HEGP collimator. De sensitiviteit, gemeten over de gesimuleerde profielen door het totaal aantal tellen per verval te bepalen, was hoger voor de LEHR en HEGP collimatoren dan voor de PC collimator (e.g. 3.1×10^{-5} vs. 2.9×10^{-5} tellen per verval voor ^{131}I). Echter, bij gelijke ruisniveaus lieten de fantoommetingen zien dat de CRCs vergelijkbaar waren voor de PC and LEHR collimatoren voor $^{99\text{m}}\text{Tc}$. Bovendien verbeterde de PC collimator de CRCs significant in vergelijking met de HEGP collimator voor ^{131}I en ^{18}F . In vergelijking met de standaard parallel hole collimatoren heeft het prototype, bestaande uit een enkelvoudige rij van parallelle kegelvormige gaten (de PC collimator), de potentie om de beeldkwaliteit van hoogenergetische SPECT beelden significant te verbeteren.

Jodium-131-therapie wordt gebruikt voor de behandeling van recidive gedifferentieerde schildklier carcinoomen. Pre-therapeutische ^{124}I PET/CT met een lage activiteit (~1% van ^{131}I activiteit) kan worden uitgevoerd om te bepalen of de opname van ^{131}I en daarmee het therapeutische effect te verwachten is. Echter, verschillende groepen hebben fout-negatieve ^{124}I PET/CT beelden in vergelijking met de post-therapeutische ^{131}I SPECT/CT beelden waargenomen. Het doel van **Hoofdstuk 5** was om te onderzoeken of de gerapporteerde verschillen toegeschreven kunnen worden aan het verschil in detecteerbaarheid van laesies tussen ^{124}I PET/CT en ^{131}I SPECT/CT. Hiermee kan worden bepaald of de toegediende ^{124}I activiteit voldoende is om gelijkwaardige detecteerbaarheid te behalen. Fantoommetingen werden uitgevoerd met het NEMA 2007

beeldkwaliteitsfantoom. Als maat voor de detecteerbaarheid werd de contrast-ruis verhouding berekend. De ^{124}I activiteit werd vervolgens uitgedrukt als een percentage van de ^{131}I activiteit die benodigd is om dezelfde contrast-ruis verhouding te behalen. Deze grootte werd gedefinieerd als het equivalent detecteerbaarheidspercentage (detectability equivalence percentage (DEP)). De DEPs lager waren voor kleine bollen, waardoor een relatief lage activiteit ^{124}I voldoende bleek om vergelijkbare detecteerbaarheid van laesies te behalen op ^{124}I PET/CT en ^{131}I SPECT/CT beelden. De DEP was respectievelijk 1.5, 1.9, 1.9, 4.4, 9.0, en 16.2% voor bollen met een diameter van 10, 13, 17, 18, 25 en 37 mm, voor de attenuatie- en verstrooiing gecorrigeerde SPECT versus de PSF gemodelleerde en time-of-flight (TOF) gecorrigeerde PET beelden. Voor no-PSF no-TOF PET was de DEP 3.6, 2.1, 3.5, 7.8, 15.1, en 23.3%, respectievelijk. Hieruit concludeerden wij dat een relatief lage ^{124}I activiteit van 74 MBq (~1% van de ^{131}I activiteit) voldoende was om vergelijkbare detecteerbaarheid te behalen op ^{124}I PSF TOF PET/CT en ^{131}I SPECT/CT voor kleine bollen (≤ 10 mm). Dit werd aangenomen omdat de gerapporteerde DEPs ongeveer 1% waren. Fout-negatieve ^{124}I PET/CT resultaten kunnen in vergelijking met de post-therapeutische ^{131}I SPECT/CT worden toegeschreven aan het verschil in detecteerbaarheid voor grote laesies (> 10 mm) en voor no-PSF no-TOF PET. Dit werd aangenomen omdat de DEPs groter dan 1% waren. Om vergelijkbare detecteerbaarheid van laesies te behalen zijn ^{124}I activiteiten van 170 MBq gerechtvaardigd, omdat DEPs werden gemeten van 3.5% voor laesies met een diameter tot 17mm op no-PSF no-TOF PET.

Kwantitatieve SPECT beelden zijn vereist voor dosimetrie ter geleiding van de behandeling. Echter, kwantitatieve SPECT beeldvorming van isotopen, zoals ^{131}I , die hoogenergetische fotonen uitzenden blijft een uitdaging. Verstrooiing en collimator-penetratie hebben namelijk een negatieve invloed op de beeldkwaliteit. De kwaliteit van SPECT beelden kan worden verbeterd door de verstrooiing en collimator-detector-respons (CDR) in de reconstructie te verwerken.

Hoofdstuk 6 vergelijkt zowel verstrooiingscorrectiemodellen gebaseerd op triple-energy-window (TEW) en Monte Carlo methodes, als verschillende methodes voor CDR correctie door middel van fantoommetingen. Hiervoor werd een SPECT/CT meting van het NEMA IEC fantoom uitgevoerd. Vervolgens zijn er beelden gereconstrueerd met de volgende reconstructieparameters: 1) zonder verstrooiingscorrectie, 2) met TEW verstrooiingscorrectie en 3) met verstrooiingscorrectie gebaseerd op Monte Carlo simulaties. Voor het modelleren van de CDR werden a) geometrische Gaussische CDRs en b) Monte Carlo gesimuleerde CDRs gebruikt. Voor de gereconstrueerde beelden werden de nauwkeurigheid van de kwantificatie, de contrast-ruis verhouding, contrast-herstel-coëfficiënten, de achtergrondvariabiliteit en de gemiddelde fout in het long compartiment bepaald. De procentuele fout in de kwantificatie was respectievelijk $< 1\%$, -26% and 33% in vergelijking met de metingen van de dosis kalibrator, voor de Monte Carlo methode, de TEW methode en zonder verstrooiingscorrectie. Hogere contrast-herstel-coëfficiënten werden behaald voor de Monte Carlo gesimuleerde CDRs in vergelijking met de geometrische CDRs en zonder CDRs. De contrast-herstel-coëfficiënten van de TEW methode waren vergelijkbaar met de Monte Carlo methode. Echter, voor de TEW methode was een experimenteel bepaalde weegfactor vereist. De reconstructie methode met verstrooiingscorrectie gebaseerd op Monte Carlo simulaties en Monte Carlo gesimuleerde CDRs leverde intrinsiek kwantitatieve ^{131}I SPECT beelden op met contrast-herstel-coëfficiënten vergelijkbaar met de TEW methode, maar zonder de noodzaak voor experimenteel bepaalde weegfactoren.

Conclusies

- Metingen met het hybride prototype voor simultane fluoroscopische en nucleaire beeldvorming van hetzelfde volume, hebben laten zien dat simultane hybride beeldvorming in de interventiekamer mogelijk is.
- Een kalibratiemethode kan worden gebruikt om de resolutie en co-registratie van simultaan verkregen fluoroscopische en nucleaire beelden te verbeteren door de systeemparameters te kalibreren.
- In vergelijking met de standaard parallel hole collimatoren heeft het prototype, bestaande uit een enkelvoudige rij van parallelle kegelvormige gaten (de PC collimator), de potentie om de beeldkwaliteit van hoogenergetische SPECT beelden significant te verbeteren.
- Een relatief lage ^{124}I activiteit van 74 MBq (~1% van de ^{131}I activiteit) was voldoende om vergelijkbare detecteerbaarheid te behalen op ^{124}I PSF TOF PET/CT en ^{131}I SPECT/CT voor kleine bollen (≤ 10 mm). Fout-negatieve ^{124}I PET/CT resultaten kunnen in vergelijking met de post-therapeutische ^{131}I SPECT/CT worden toegeschreven aan het verschil in detecteerbaarheid voor grote laesies (> 10 mm) en voor no-PSF no-TOF PET.
- De reconstructie methode met verstrooiingscorrectie gebaseerd op Monte Carlo simulaties en Monte Carlo gesimuleerde CDRs leverde intrinsiek kwantitatieve ^{131}I SPECT beelden op met contrast-herstel-coëfficiënten vergelijkbaar met de TEW methode, maar zonder de noodzaak voor experimenteel bepaalde weegfactoren.



List of publications

C. Beijst, M. Elschot, M.A. Viergever, H.W.A.M. de Jong, "Toward simultaneous real-time fluoroscopic and nuclear imaging in the intervention room", *Radiology*, 2016, nr. 1, vol. 278, pp. 232-238

C. Beijst, J.W. Kist, M. Elschot, M.A. Viergever, O.S. Hoekstra, B. de Keizer, H.W.A.M. de Jong, "Quantitative comparison of ^{124}I PET/CT and ^{131}I SPECT/CT detectability", *The Journal of Nuclear Medicine*, 2016, nr. 1, vol. 57, pp. 103-108

C. Beijst, M. Elschot, M.A. Viergever, H.W.A.M. de Jong, "A parallel-cone collimator for high-energy SPECT", *The Journal of Nuclear Medicine*, 2015, nr. 3, vol. 56, pp. 476-482

B. Arsenali, H.W.A.M. de Jong, M.A. Viergever, D.B. Dickerscheid, **C. Beijst**, K.G.A. Gilhuijs, "Dual-head gamma camera system for intraoperative localization of radioactive seeds", *Physics in Medicine and Biology*, 2015, vol. 60, pp. 7655-7670

C. Beijst, G. Schep, E. van Breda, P.F.F. Wijn, C. van Pul, "Accuracy and precision of CPET equipment: A comparison of breath-by-breath and mixing chamber systems", *Journal of Medical Engineering and Technology*, 2012; vol. 37, nr. 1, pp. 35-42

C. Beijst, M. Elschot, S. van der Velden, H.W.A.M. de Jong, "Multimodality calibration for simultaneous fluoroscopic and nuclear imaging", *Submitted for publication*

C.A.J. van Gils, **C. Beijst**, R. van Rooij, H.W.A.M. de Jong, "Impact of reconstruction parameters on quantitative ^{131}I SPECT", *Submitted for publication*



Dankwoord

Na vier jaren hard werken is nu het moment aangebroken om iedereen die mij in deze periode direct of indirect heeft geholpen te bedanken.

Allereerst wil ik graag mijn copromotor dr. ir. Hugo de Jong en promotor prof. dr. ir. Max Viergever bedanken. Hugo, bedankt voor de prettige samenwerking. Ik vond je pragmatische aanpak erg prettig en ik kijk er naar uit om met de opleiding tot klinisch fysicus te beginnen. Bedankt voor de gezellige BBQs in je achtertuin! Beste Max, al op de eerste dag vroeg je mij om je aan te spreken met 'je' en 'jij' in plaats van 'u'. Dit was tekenend voor het contact tijdens mijn promotie. Het was gemakkelijk om met je in contact te komen, ondanks je drukke agenda.

Graag wil ik de beoordelingscommissie bedanken voor de tijd die allen hebben besteed aan het lezen van mijn proefschrift. Hartelijk dank prof. dr. R. De Bree, prof. dr. ir. J.J.W. Lagendijk, prof. dr. M. van Vulpen, prof. dr. ir. R. Boellaard, en prof. dr. M.G.E. Lam.

In het begin van mijn promotie heb ik een kamer gedeeld met Mattijs, Alan en Edwin. Ik kon met mijn vragen altijd bij jullie terecht. Beste Mattijs, je hebt me in het begin erg geholpen en je was snel met je nuttige input bij mijn papers. De biertjes (met o.a. Maarten) zorgden voor de nodige ontspanning. Dear Alan, I remember you carrying a log under your arm during an entire party (Mattijs' defense party) like a real caveman. That was awesome. Edwin, de ontelbare bakkies koffie zorgden ervoor dat we scherp bleven, en het klimmen en boulderen gaven de nodige afleiding. In de loop van mijn promotie voegden zich Jaap, Robert, Sandra, Remco en Wilco bij de groep. Jaap, het was gezellig om met jou een kamer te delen, de conversaties konden altijd een onverwachte wending nemen. Bedankt Robert, je bent een echte recht-voor-zijn-raap Hagenees met wijsheden die niet zouden misstaan op een Delfts blauw tegeltje. Sandra, er was er maar een die vrolijk fluitend door het ziekenhuis liep. Jouw humeur in onverwoestbaar. Adriaantje (Remco)! wanneer beginnen we aan het Shaun T. fitness programma? Wilco, voor iemand die niet van verkleeden houdt, ben je onwijs goed in het samenstellen van een outfit. Drommels, drommels, drommels, jouw Baron-outfit was geweldig.

Beste klinisch fysici (in opleiding), Arnold, Bart, Rob en Bastiaan, bedankt voor het gezelschap tijdens de talloze lunches, bakjes koffie, stukken taart en natuurlijk de prettige samenwerking. Arnold, je bent niet alleen een 'family man' thuis maar ook een sugar daddy voor de groep. Bart, sinds dat je weg bent heb ik nooit meer zo kunnen genieten van een broodje bal met pindasaus. Rob, jij bent de échte klimmer in de groep (jij klimt niet alleen maar op plastic). Bovendien heb je in de loop der jaren een uitstekende youtube-index opgebouwd in je hoofd. Met Bastiaan, een van de wijzen uit het oosten met een voorliefde voor Brabantse gezelligheid, ben je altijd in goed gezelschap. Ook wil ik graag de klinisch fysici in opleiding die voor kortere (of langere) tijd in de groep werkzaam waren bedanken voor de samenwerking: Dennis, Rens, Wendy, Koen en Paul. Koen, bedankt voor de samenwerking aan het 131I reconstructie paper.

Graag wil ik de laboranten van afdeling nucleaire geneeskunde en de mensen van radionuclidenapotheek bedanken voor hun ondersteuning. Bedankt Denise, Ellen, Erik, Hans, John, John, Linda, Mike, Nikki, Petra, Rianne, Roel, Susan, Suzanne, Tim, Yasmin en alle studenten dat jullie elke keer klaar stonden om mijn problemen op te lossen. Ook wil ik Remmert en Gerard bedanken voor hun ondersteuning in het lab en het technisch cluster voor de technische ondersteuning. Gert, zonder jouw reparaties aan de Argus had ik mijn experimenten niet kunnen doen.



Jakob en Bart, hartelijk dank voor de samenwerking tijdens de 124I-studie. Naast het feit dat we een mooi paper hebben geschreven, heb ik de samenwerking als erg prettig ervaren. Laten we nog een keer een paper schrijven.

Dear housemates and regular guests of the Lange Nieuwstraat. I had so much fun during all the nights out, parties and unforgettable holidays. You are like a family! Thank you Aisha, Alex, Amin, Ana, Anne, Anne, Anshu, Chantal, Elena, Erik, Hester, Joana, João, Lisa, Magda, Matteo, Matthew, Maxence, Natasha, Roberto, Sara, Saskia, Soraya, Stefano, Susana, Tristan, Vittoria and Wouter.

Thanks Alex, Cyril, Edwin and Pieter for going climbing and bouldering with me. It was a great way of clearing my mind.

Beste (aspirant) leden en reünisten van de Tuna, van de oudste tot de jongste generatie, bedankt voor de onvergetelijke festivals in binnen- en buitenland, het 50-jarig bestaan, de lustrumreis, cantussen, kerstdiners en de CD opnames. Ik hoop dat er nog vele komen. Beste Frans Tielemans, bedankt voor de (kerst)diners en gezellige avonden.

Jan Martijn, bedankt voor de gezellige lunches bij Pizzeria Tricolore en in de botanische tuinen, de lekkere bakjes espresso achteraf, de goede raad en de hulp bij mijn proefschrift. Bestuursgenoten van de E.S.R. Thêta, beste Eline, Karel en Karlijn. Ik heb enkele keren geprobeerd uit te leggen waarover mijn promotie ging, maar ik weet niet of dat ooit helemaal gelukt is. Ik weet nog dat ik vol trots een filmpje uit mijn eerste paper liet zien en dat de eerste vraag was: "Zit er geen muziek onder?" De volgende keer zal ik er een hitje onder zetten. Hoe dan ook, bedankt voor jullie morele ondersteuning!

Niek, al van jongs af aan kennen wij elkaar, dus ik ben blij dat je mijn paranimf wil zijn. Bedankt voor de zeilweekenden, het Carnaval vieren en de goede stapavonden.

Lieve familie, bedankt dat jullie altijd voor mij klaarstaan. Joep, allereerst bedankt voor linsnedes die je gemaakt hebt voor mijn proefschrift. Dit maakt het ontwerp van mijn proefschrift erg persoonlijk. Dankjewel papa en mama, dat jullie er altijd voor mij waren en zijn. Ik ben er van overtuigd dat de extra curriculaire activiteiten waar jullie ons vroeger naartoe hebben gebracht mij gevormd hebben, en dat deze vorming alleen mogelijk was dankzij jullie ondersteuning. Jullie hebben mij altijd door dik en dun gesteund.



CV

Casper Beijst was born on the 13th of August 1986 in Tilburg. He went to secondary school at the Theresia Lyceum in Tilburg, where he finished in 2004 (in Dutch ‘gymnasium’). The same year, he started his bachelor studies in Applied Physics at the Eindhoven University of Technology. He passed his bachelor exam in 2010, and continued with his master’s degree at the same university. In the year 2010, he went to Berkeley for an internship at the Lawrence Berkeley National Laboratory. The specialization of his master’s degree was in Physical Instrumentation and Medical Physics and the research for his master’s thesis was conducted at the Maxima Medical Center in Veldhoven. In 2011, he obtained his Master’s degree from the Eindhoven University of Technology. He then started working as a PhD student at the University Medical Center Utrecht. The results of his work as a PhD student are described in this thesis.

In March 2016, he started working as a medical physics resident at the University Medical Center Utrecht in the department of radiology and nuclear medicine.



